PEROVSKITE MICROTUBULAR MEMBRANES FOR PURE HYDROGEN PRODUCTION FROM WATER SPLITTING

Rafael Vilar Franca

A thesis submitted for the degree of Doctor of Philosophy (PhD) in Chemical Engineering at Newcastle University

SCHOOL OF CHEMICAL ENGINEERING AND ADVANCED MATERIALS

May 2013

Abstract

The purpose of this thesis is to investigate the feasibility of producing hydrogen with microtubular membranes made of mixed ionic electronic conducting perovskite by membrane-based steam reforming. This process involves water splitting in one side of the membrane followed by oxygen ions transport across the membrane to react with methane in the membrane reaction side. The overall process produces two separate streams of pure hydrogen and syngas.

Initial experiments were performed using temperature programmed redox (water oxidation and methane reduction) cycles to investigate the feasibility of three perovskites ($Ba_{0.5}Sr_{0.5}Co_{0.8}Fe_{0.2}O_{3-\delta}$, $La_{0.6}Sr_{0.4}Co_{0.2}Fe_{0.8}O_{3-\delta}$ and $La_{0.7}Sr_{0.3}FeO_{3-\delta}$) to produce hydrogen from water splitting. Membrane fragments and powder materials were used during these tests, resulting in $La_{0.6}Sr_{0.4}Co_{0.2}Fe_{0.8}O_{3-\delta}$ and $La_{0.7}Sr_{0.3}FeO_{3-\delta}$ powder materials showing better activity for hydrogen production than $Ba_{0.5}Sr_{0.5}Co_{0.8}Fe_{0.2}O_{3-\delta}$. However $La_{0.6}Sr_{0.4}Co_{0.2}Fe_{0.8}O_{3-\delta}$ presented better performance among all membrane fragments tested under the experiments conditions.

Preliminary oxygen permeation and hydrogen production experiments using membranes systems were also carried out with all perovskites; $Ba_{0.5}Sr_{0.5}Co_{0.8}Fe_{0.2}O_{3-\delta}$ microtubes presented high oxygen permeation, however low activity for hydrogen production from water splitting. $La_{0.7}Sr_{0.3}FeO_{3-\delta}$ microtubes presented low oxygen permeation rates and no activity for hydrogen production, post-operation analysis showed the presence of a strontium/sulfur layer on the microtubes surfaces which may have affected permeation. $La_{0.6}Sr_{0.4}Co_{0.2}Fe_{0.8}O_{3-\delta}$ microtubes presented better potential for oxygen permeation and hydrogen production among the other membranes; hence these microtubes were selected for further long term experiments.

$La_{0.6}Sr_{0.4}Co_{0.2}Fe_{0.8}O_{3-\delta}$ microtubular membrane reactors were tested for long term oxygen permeation followed by membrane-based steam reforming. The membranes were subjected to two known axial temperature profiles in the temperature of 900°C and 960°C. The microtubes showed good stability under reaction conditions, operating over a total operation period of *ca* 400 hours of oxygen permeation followed by *ca* 400 hours of steam reforming. The outlet gas composition from both sides (methane and water side) of the membranes were analysed which allowed material a balance. This indicated that the hydrogen production occurred due to oxygen flux across the membrane and not

just surface reaction. Post-operation analysis of the microtubes revealed the presence of a strontium-enriched dense layer on the water-exposed membrane surface and of crystallites enriched with cobalt and sulfur on the methane feed side surface.

Acknowledgements

I would first of all express my sincere gratitude to my supervisor, Prof. Ian Metcalfe, for his continuous support, motivation and guidance during my PhD study. He was always helpful and available to discuss any kind of subject whenever I needed. I would like to thank him for being not only a great supervisor but also a good friend during all these years, thanks for the support and great advices when I needed more.

I would like to thank Dr. Alan Thursfield for his supervision and support in the laboratory; his knowledge and technical advices were very important to this project. I'm also grateful to the group of professor Kang Li at Imperial College, for supplying most of the membranes used in this project. The collaboration and assistance of his group was crucial to the improvement and realisation of my experimental work.

I also had much help from the staff of Newcastle University during my PhD. I wish to thank Justine McGruther, Craig Clark, Angela Coutts and Kay Garrick for their immense patient and assistance. Thanks for always being helpful and friendly. I cannot forget to thank Pauline Carrick and Maggie White for their assistance with characterisation analysis. I would also like to thank the guys from the workshop; in special to Simon Daley, Iain Ditchburn, Jamie Halliday and Iain Strong for their help building and repairing the reactor used in my project.

I would like to express my gratitude to the members of my group and my office; Callum Campbell, Danai Poulidi, Maria Elena Rivas, Naimah Ibrahim, Mas Jalil, Sureena Abdullah, Hang Qi, James Merotra, Ahmed Abdo, Thea Coward, Joseph Ikwebe and Elizabeth Eterigho for the support and friendship. Special thanks to Claire Thompson and Luke Watkins for being amazing friends and also for keeping my energy levels high in the last months of PhD. I would always be grateful for their immense help.

I cannot imagine this PhD without my really good friends Francesco Dal Grande and Arul Murugan. Thanks guys for all the help during my first year in UK. I would like to thank Francesco for all his support and companionship; thanks for our endless conversations that always cheered me up. Arul thanks for being my loyal friend during the entire PhD; we have been through good and bad moments together always helping each other. I am grateful he was always there when I needed. I would also like to thank my friends outside university; Melina, Beatrice, Victor, Panos, Alex, Gina, Asier and

Ian Hewitt for being truly good friends when I needed most. Thanks to Dimitris Presvytis for being an amazing friend during the most difficult times and also for being a brilliant “flatmate”. I also express my sincere gratitude to José Renato for bringing me some Brazilian happiness in the last year. Thanks for being a really good friend and for all your support. I would like to thank for the lifetime friendship of Thomas Curtis and his family; thanks for the immense generosity and hospitality during my first weeks in Newcastle. I wish to give a massive thanks to Epaminondas Chalkids and Daniel Apostolidis for being more than basketball teammates and friends. Thanks for being my real brothers in UK and to always keep me smiling. I could not imagine what it would have been like without them. *“The greatest gift of life is friendship, and I have received it”.*

I would like to give a sincere thanks to Antonia Currie and her family; thanks for all patient, and unconditional love during the last two years. I will always remain grateful for their support and for being my family in Newcastle. I would also like to thank my parent’s partners, Marcia Cirne and Marcos Espinola, for always being kind and treating me as a son. Finally I would like to express my heartfelt thanks to Milena Franca, Rosangela Vilar and Kepler Franca for all support towards my education and also for their selfless efforts in cultivating my personality. No words can express my love for them.

Table of Contents

CHAPTER 1

1 Introduction 1

1.1 Overview 1

1.2 Purpose of the research 2

1.3 Structure of the thesis 3

1.4 Aims and Objectives 3

2 Membranes for hydrogen production 5

2.1 Introduction 5

2.2 Conventional hydrogen production and separation methods 6

2.2.1 Hydrogen production from natural gas 6

2.2.2 Hydrogen production from water 7

2.2.3 Hydrogen from biomass 8

2.3 Membrane systems 10

2.3.1 Hydrogen perm-selective membranes 12

2.3.2 Oxygen permeable membranes 13

2.4 Oxygen transport membranes for hydrogen production 20

2.5 Application of OTMs to syngas production from hydrocarbon sources 21

2.6 Applications of OTMs to hydrogen production from water splitting 24

2.6.1 OTM-based water splitting using hydrogen as reducing agent 28

2.6.2 OTM-based water splitting using ethane as reducing agent 29

2.6.3 OTM-based water splitting using carbon monoxide as reducing agent ... 30

2.6.4 OTM-based water splitting using methane as reducing agent 32

2.6.5 Summary 33

3 Experimental 35

3.1 Introduction 35

3.2 Membrane fabrication 35
3.3 Temperature programmed experiments 37
3.3.1 Material preparation and characterisation 37
3.3.2 Apparatus 37
3.3.3 Temperature programmed experiments procedure 38
3.4 Membranes experimental setup 38
3.4.1 Feed system 38
3.4.2 Furnace 40
3.4.3 Membrane module 41
3.4.4 Analysis system 43
3.5 Oxygen permeation 44
3.6 Membrane-based steam reforming 45
4 Preliminary studies 47
4.1 Introduction 47
4.2 Thermal expansion of the microtubes 47
4.2.1 Effective membrane area calculation 49
4.3 Residence time distribution 49
4.4 Blank membrane-based steam reforming test 52
4.5 Attempted studies 53
4.5.1 Tubular membrane reactors 53
4.5.2 Disk membrane reactors 55
4.5.3 Sealant materials 56
4.5.4 Catalyst materials 59
4.5.5 Membrane-based water-gas shift 61
4.5.6 Autothermal membrane-based steam reforming studies 63
5 Materials Selection 66
5.1 Introduction 66
5.2 Temperature programmed experiments 67

5.2.1 Characterisation of fresh materials 68
5.2.2 TPR/TPO cycles 69
5.2.3 Post operation characterisation 72
5.3 Membrane Experiments 74
5.3.1 Characterisation of fresh microtubes 74
5.3.2 Oxygen Permeation 76
5.3.3 Membrane-based steam reforming 77
5.3.4 Post operation characterisation 79
5.4 Summary 82
6 $La_{0.6}Sr_{0.4}Co_{0.2}Fe_{0.8}O_{3-\delta}$ microtubular membranes for hydrogen production from water splitting 83
6.1 Introduction 83
6.2 Characterisation of fresh LSCF6428 84
6.3 Oxygen permeation studies 85
6.4 Membrane-based steam reforming studies 87
6.4.1 Induction Period 88
6.4.2 SW furnace (900°C) 88
6.4.3 LN furnace (900°C) 91
6.5 Material Balance 93
6.5.1 Conversion and selectivity 95
6.6 Post operation characterisation 95
6.6.1 SW furnace 96
6.6.2 LN furnace 97
6.7 Summary 99
7 Conclusions and suggested future work 100
7.1 Research outcome 100
7.2 Suggested future work 103
8 References 105

9 Appendix 3-A 116

10 Appendix 3-B 117

11 Appendix 3-C 118

12 Appendix 5-A 119

13 Appendix 6-A 121

14 Appendix 6-B 122

List of Figures

Figure 2.1 Hydrogen production pathways presenting different methods and variety of feedstocks [22]..... 6
Figure 2.2 Schematic of membrane separation process showing transport from the feed stream to the permeated stream [18]..... 10
Figure 2.3 Hydrogen permeation through a dense palladium membrane showing the solution/diffusion mechanism [62]..... 13
Figure 2.4 Ideal structure of ABO_3 perovskite in which oxygen vacancies are generated by replacement of A and/or B ions [75]. 14
Figure 2.5 Schematic principle for oxygen transport throuhg mixed ionic electronic membranes at elevated temperature from high oxygen activity to low oxygen activity. 15
Figure 2.6 SEM image of a microtube (hollow fibre) membrane produced by phase inversion technique [84]. 17
Figure 2.7 Partial oxidation of methane using MIEC membranes. Oxygen ions are transported through the membranes to react with methane to produce syngas. 18
Figure 2.8 Membrane-based steam reforming using MIEC membranes. Oxygen ions are transported through the membranes to react with methane to produce separate streams of hydrogen and syngas. 19
Figure 3.1 Schematic apparatus for microtubes fabrication by phase inversion [151]. . 36
Figure 3.2 SEM images of the membrane cross sections of (a) LSCF6428, (b) LSF731 and (c) BSCF5582. 36
Figure 3.3 Schematic of the experimental setup for oxygen permeation and membrane-based steam reforming experiments. 38
Figure 3.4 Schematic diagram of the water saturator system. 39
Figure 3.5 Water saturator calibration curve. 40
Figure 3.6 SW and LN furnaces; internal temperature profile of reactor at 900°C. Horizontal lines indicate (a) total heated length of membranes using SW furnace, (b) total heated length of membranes using LN furnace and (c) total length of membranes used during the experiments. 41
Figure 3.7 Schematic of the microtubes membrane module. 42
Figure 3.8 New microtube membrane module design; using silicone sealant (in black). 43
Figure 3.9 Schematic diagram of oxygen permeation experiments. 45

Figure 3.10 schematic diagram of membrane-based steam reforming. 46
Figure 4.1 Microtubes bending when exposed to high temperatures due to high thermal expansion coefficient. 48
Figure 4.2 Lumen-side stimulus-response residence time distribution profile at 900°C, using nitrogen (20 ml (STP) min^{-1}) as a carrier gas and argon (20 ml (STP) min^{-1}) as a tracer. 50
Figure 4.3 Shell-side stimulus-response residence time distribution profile at 900°C, using nitrogen (20 ml (STP) min^{-1}) as a carrier gas and argon (20 ml (STP) min^{-1}) as a tracer. 51
Figure 4.4 Blank membrane-based reforming at 900°C using alumina tubes to simulate the microtubes. Lumen side was supplied with methane (5%) at 20 ml min^{-1} and the shell side with water vapour (7.2%) at 20 ml min^{-1} 52
Figure 4.5 Microtubes sintering furnace; internal temperature profile of at 1200°C. 54
Figure 4.6 Mechanical failure of two membranes in the reactor; the other two membranes remained in good conditions. 55
Figure 4.7 Disk membranes (1mm thick) produced by hydraulic press. 56
Figure 4.8 Glass sealant material blocking permeation area of a disk membrane. 57
Figure 4.9 Oxygen permeation with BSCF short microtube on the lumen-side outlet, varying air supplied on the shell side with argon as sweep gas on the lumen side at 20 ml min-1. 58
Figure 4.10 “White powder” observed at the quartz shell. 59
Figure 4.11 SEM images and EDS maps of the surface of LSCF6428 disk membranes after (a) 5 seconds and (b) 50 seconds of palladium deposition. 61
Figure 4.12 Schematic diagram of water-gas shift experiments. 62
Figure 4.13 Membrane-based water-gas shift with water vapour supplied on the lumen side at 20 ml min^{-1} and carbon monoxide (0.5%) on the shell side at 20 ml min^{-1}using LN furnace (900°C). 62
Figure 4.14 Schematic representation of autothermal membrane-based process for hydrogen production. 64
Figure 4.15 Outlet composition from autothermal membrane-based steam reforming studies using the LN furnace (a) on the shell side and (b) on the lumen side. 65
Figure 5.1 Schematic representing (a) periodically temperature programmed process and (b) oxygen permeating mebrane system for hydrogen production via steam reforming [109]. 66

Figure 5.2 SEM Images of fresh microtubes fragments (a) BSCF5582, (b) LSCF6428 and (c) LSF731. 68
Figure 5.3 Hydrogen production during 1st and 15th TPOs at 900°C of *ca* 50mg of BSCF5582, LSCF6428, LSF731 (a) powder materials and (b) membrane fragments. . 71
Figure 5.4Post operation SEM images of (a) BSCF5582 and (b) LSCF6428 membrane fragments after 15th TPR/TPO cycles. 72
Figure 5.5 Post operation SEM images of the LSF731 membrane fragment after 15^{th} TPR/TPO cycles. 73
Figure 5.6 SEM images of the fresh BSCF5582 (a) shell-side surface of the microtubes, (b) the lumen-side surface and (c) cross-section. 74
Figure 5.7 SEM images of the fresh LSF731 (a) shell-side surface of the microtubes, (b) the lumen-side surface and (c) cross-section. 75
Figure 5.8 SEM image of the fresh LSF731 cross-section showing enriched sulfur/strontium layer. 75
Figure 5.9 Oxygen permeation on the lumen-side outlet, varying air supplied on the shell side with argon as sweep gas on the lumen side at 20 ml min^{-1}. 77
Figure 5.10 Hydrogen production molar fraction on the shell-side outlet at different water vapour concentrations (shell-side inlet) when methane was maintained constant on the lumen-side inlet at 5%. 78
Figure 5.11 Hydrogen production molar fraction on the shell-side outlet at different methane concentrations (lumen-side inlet), when water vapour was maintained constant on the shell-side inlet at 7.2%. 79
Figure 5.12 Post operation SEM images of BSCF5582 microtube (a) shell-side surface and (b) lumen-side surface. 80
Figure 5.13 Post operation SEM images of LSF731 microtube shell-side surface showing dense strontium layer. 81
Figure 5.14 Post operation SEM images of LSF731 microtube cross-section showing dense strontium layer. 81
Figure 6.1 Schematic diagram of membrane-based steam reforming at 900°C 83
Figure 6.2 SEM images of the fresh (a) lumen-side surface of the microtubes, (b) the shell-side surface and (c) cross-section. 84
Figure 6.3 Oxygen permeation with air supplied on the shell side at 20 ml min^{-1} and argon as sweep gas on the lumen side at 20 ml min^{-1}using SW furnace (916°C and 900°C) 86

Figure 6.4 Oxygen permeation with air supplied on the shell side at 20 ml min^{-1} and argon as sweep gas on the lumen side at 20 ml min^{-1}using LN furnace (900°C)..... 87
Figure 6.5 Outlet composition from membrane-based steam reforming at 900°C using the SW furnace on the (a) shell side (water-splitting side) when methane is supplied as a reducing gas at the lumen side, (b) expanded view of showing the affect of interruption of the methane supply with argon and (c) lumen side (methane oxidation side) when methane is supplied as a reducing gas. 90
Figure 6.6 Outlet composition from membrane-based steam reforming at 900°C using LN furnace on the (a) shell side (water-splitting side) and (b) lumen side (methane oxidation side) when methane is supplied as a reducing gas. 91
Figure 6.7 Shell-side outlet composition from membrane-based steam reforming at 960°C using LN furnace when methane is supplied as a reducing gas. 93
Figure 6.8 Post operation SEM images of the microtubes using the SW furnace: (a) the lumen-side surface of cold zone showing small crystals, and (b) the shell-side surface of the hot zone showing the development of cracks on the membrane surface and the presence of needle and sphere-like crystals. 96
Figure 6.9 Post operation XRD pattern of microtubes using the LN furnace of (a) shell-side cold zone and (b) shell-side hot zone. Low intensity peak assignments; (▲) SiO_2 (■)) La_2O_3 (●) SrO. 97
Figure 6.10 Post operation SEM images of the microtubes using the LN furnace: (a) the lumen-side surface of hot zone showing small crystals, (b) the shell-side surface of the hot zone showing needle like crystals and (c) the cross-section showing the shell-side surface of the hot zone covered with a micro-layer. 98
Figure 7.1 Schematic representation of autothermal membrane-based process for hydrogen production. Water splitting is performed in one set of membranes and the other set provides oxygen for methane combustion. 104
Figure 9.1 Experimental setup used in this project. 116
Figure 11.1 Membrane module before sealed. 118
Figure 12.1 Products of TPR/TPO at 900°C during 15 cycles for powder materials. (a) and (b) BSCF5582; (c) and (d) LSCF6428 and (e) and (f) LSF731. 119
Figure 12.2 Products of TPR/TPO at 900°C during 15 cycles for membranes fragments. (a) and (b) BSCF5582; (c) and (d) LSCF6428 and (e) and (f) LSF731. 120
Figure 13.1 XRD patterns of unused LSCF6428 fresh membranes (a) shell side and (b) lumen side. 121

List of tables

Table 2.1 Hydrogen production from water-splitting using oxygen transport membranes. 26
Table 3.1 Dimensions of the sintered microtube membranes. 37
Table 4.1 Approximated active area (S_A) of each membrane module. 49
Table 4.2 Semi-quantitative EDS analysis of disk membrane blocked by glass sealant material. 57
Table 4.3 Semi-quantitative EDS analysis of LSCF membranes with no oxygen permeation due to silicon contamination and "white powder" encountered on the top of the membranes. 59
Table 4.4 EDS analyses of LSCF6428 membranes coated with palladium catalyst. 60
Table 4.5 Post operation EDS data of LSCF6428 microtubes after membrane-based water-gas shift. 63
Table 5.1 BET analysis of fresh OCM samples. 68
Table 5.2 Spot EDS analyses of fresh microtubes fragments. 69
Table 5.3 Spot EDS analyses of fresh microtubes fragments after 15th TPR/TPO cycles. 73
Table 5.4 Spot EDS data of fresh BSCF5582 and LSF731 microtubes; LS (Lumen side) and SS (Shell side). 76
Table 5.5 Post operation EDS data of BSCF5582 and LSF731 microtubes. 82
Table 6.1EDS data of fresh LSCF6428 microtubes. 84
Table 6.2 Membrane treatment history 85
Table 6.3 Average mole fractions of products from membrane-based steam reforming at 900°C using SW furnace (between 100 and 200 hours) and LN furnace (between 150 and 350 hours). 93
Table 6.4 Post operation EDS data of microtubes using SW furnace. 97
Table 6.5 Post operation EDS data of microtubes using LN furnace. 97
Table 10.1 Results for water saturator calibration. 117

Nomenclature

BET	*Brunauer-Emmett-Teller*
BSCF5582	$Ba_{0.5}Sr_{0.5}Co_{0.8}Fe_{0.2}O_{3-\delta}$
COG	*Coke oven gas*
CVD	*Chemical vapour deposition*
EDS	*Energy dispersive X-ray*
EEA	*European Environment Agency*
GC	*Gas Chromatograph*
GCO	*Gadolinium doped ceria*
LN	*Long length and narrow bore furnace*
LSCF6428	$La_{0.6}Sr_{0.4}Co_{0.2}Fe_{0.8}O_{3-\delta}$
LSF731	$La_{0.7}Sr_{0.3}FeO_{3-\delta}$
MFC	*Mass flow controllers*
MIEC	*Mixed ionic-electronic conducting*
OCM	*Oxygen Carrier Material*
OTM	*Oxygen Transport membranes*
PSA	*Pressure swing adsorption*
POM	*Partial oxidation of methane*
QMS	*Quadrapole mass spectrometer*
SEM	*Scanning electron microscopy*
SMR	*Steam methane reforming*
STP	*Standard temperature and pressure (273.15 K, 1 atm)*
SW	*Short length and wide bore furnace*

TCD	*Thermal conductivity detector*
TPO	*Temperature programmed oxidation*
TPR	*Temperature programmed reduction*
TSA	*Temperature swing adsorption*
WGS	*Water-gas shift*
XRD	*X-ray diffraction*
$V_O^{\cdot\cdot}$	*Oxygen vacancies*
$h^{\cdot}$	*Electrons holes*
O_O^x	*Lattice oxygen*
e^-	*Electron*

Chapter 1

1 Introduction

1.1 Overview

The growing economy in emerging countries such as Brazil, Russia, China, India and, more recently, South Africa, will involve increase in population expansion, and additional demands for energy. Countries with solid economies will also require more energy due to new life standards. Forecast scenarios estimate that world energy consumption will increase by 47%, from 2010 to 2035 [1].

This growing demand for energy has to be associated with increasing the supply (new energy sources) and/or modifying techniques for better efficiency in the usage and consumption of existing resources [2]. With expectations that fossil fuels prices will remain high and concerns about environmental damage of greenhouse gas emissions suggests that the world's current energy supply is economically and environmentally unsustainable [3].

According EIA (U.S. Energy Information Administration) renewable energy is the fastest-growing source in many countries, mainly due to strong government incentives (more aggressive policies in relation of carbon dioxide emissions) [1]. Thus the tendency is to shift to lower carbon emission energy sources, which will be beneficial for whole society [4]. Hydrogen as an energy carrier meets this requirement as it does not produce greenhouse gas emissions in particular when applied in fuel cell system.

Hydrogen has the potential to compete with fossil fuels however its storage and capital costs production are still main drawbacks. For all hydrogen production processes improvements are still necessary; conventional steam reforming of methane produces hydrogen with many by-products consequently a purification method is required. Also to have a sustainable hydrogen production method, the hydrogen must be produced from a renewable source (*e.g.* water) rather than fossil fuels.

Membrane technology for hydrogen production/separation has potential to compete with conventional methods as they offer the opportunity of separating hydrogen in a

simple unit which requires less energy and consequently less investment. Recently membranes have also been investigated for hydrogen production from direct water splitting; oxygen transport membranes (OTM) are applied to remove oxygen from water dissociation therefore enhancing hydrogen conversion [5].

The main drawbacks of these membranes are durability and stability. microtubular membranes have been developed in order to improve mechanical stability and performance. This membrane geometry presents high surface area per unit of volume and reduced wall thickness which facilitate the oxygen transport. Other advantage is the possibility of avoiding high temperature sealing problems as long membranes can facilitate cold sealing.

Hydrogen has the potential to play an important role in the transition from hydrocarbons to renewable energy sources. Therefore this gives particular importance to the investigation, development and commercialisation of oxygen transport membranes systems for pure hydrogen production from water splitting.

1.2 Purpose of the research

Hydrogen is conventionally produced by steam reforming of hydrocarbons to produce a mixture of hydrogen, steam, carbon monoxide and carbon dioxide. Further hydrogen separation is required in order to produce pure hydrogen. Recently there has been considerable interest in the use of high temperature membranes to produce pure hydrogen without using a downstream separation step. These techniques use high temperature gas-solid redox (reduction and oxidation) processes for hydrogen production with oxygen transport through the membrane.

This project aims to verify the feasibility of microtubular perovskite membranes for hydrogen production from water splitting. Perovskite-type membranes, such as $Ba_{0.5}Sr_{0.5}Co_{0.8}Fe_{0.2}O_{3-\delta}$, $La_{0.7}Sr_{0.3}FeO_{3-\delta}$ and $La_{0.6}Sr_{0.4}Co_{0.2}Fe_{0.8}O_{3-\delta}$ have previously shown desirable properties for oxygen permeation [6-9]. In this thesis they are therefore proposed as potential materials for hydrogen production from water splitting.

Most of the studies involving oxygen permeable membranes for hydrogen production from water splitting lacked the detail necessary to prove that hydrogen production is due to oxygen transport through the membrane rather than surface reactions. In this work, therefore, gas analysis of both sides was performed and a material balance was also

reported. Previous studies also rarely report longevity of the membranes under operation conditions which is of extreme importance for future industrial applications. In this project long term experiments are reported and other important aspects are discussed, such as membrane failure, trans-membrane leaks and membranes sealing.

1.3 Structure of the thesis

Following this introduction, *Chapter 2* provides a background of conventional hydrogen production methods and membrane technology for hydrogen production/separation. *Chapter 2* also presents the application of oxygen permeable membranes for syngas production and a literature survey regarding water splitting using oxygen permeable membranes. Membrane fabrication procedures and experimental setups used in this project are presented in *Chapter 3*. *Chapter 4* presents preliminary studies on experimental conditions and membrane behaviour, when exposed to experimental environment and also some attempted studies. In *Chapter 5* studies to investigate the feasibility of producing hydrogen from water splitting with three perovskite materials ($Ba_{0.5}Sr_{0.5}Co_{0.8}Fe_{0.2}O_{3-\delta}$, $La_{0.7}Sr_{0.3}FeO_{3-\delta}$ and $La_{0.6}Sr_{0.4}Co_{0.2}Fe_{0.8}O_{3-\delta}$) are presented; temperature programmed and membrane system experiments were carried out during these studies. *Chapter 6* presents the long term membrane-based steam reforming studies for hydrogen production with $La_{0.6}Sr_{0.4}Co_{0.2}Fe_{0.8}O_{3-\delta}$ microtubes. Finally in *Chapter 7* the most remarkable results of this work are highlighted and also future work suggestions are given.

1.4 Aims and Objectives

The first aim of this thesis is to review the experimental work that has been performed in previous literature regarding hydrogen production from water splitting using oxygen carrier membranes in order to develop an understanding of the current limitations of the process.

A general summary of the tasks of this project is presented below:

- Fabrication and characterisation of perovskite membranes ($Ba_{0.5}Sr_{0.5}Co_{0.8}Fe_{0.2}O_{3-\delta}$, $La_{0.7}Sr_{0.3}FeO_{3-\delta}$ and $La_{0.6}Sr_{0.4}Co_{0.2}Fe_{0.8}O_{3-\delta}$) prepared by phase inversion (collaboration with Imperial College London).

- Development of membrane module suitable for hydrogen production from water splitting process, including investigation of sealant materials for high temperature membrane reactors.
- Investigation of catalytic activity towards water splitting of powder perovskites ($Ba_{0.5}Sr_{0.5}Co_{0.8}Fe_{0.2}O_{3-\delta}$, $La_{0.7}Sr_{0.3}FeO_{3-\delta}$ and $La_{0.6}Sr_{0.4}Co_{0.2}Fe_{0.8}O_{3-\delta}$) by temperature programmed experiments.
- Fabrication of disk membranes for fast kinetic investigation of the perovskite materials ($Ba_{0.5}Sr_{0.5}Co_{0.8}Fe_{0.2}O_{3-\delta}$, $La_{0.7}Sr_{0.3}FeO_{3-\delta}$ and $La_{0.6}Sr_{0.4}Co_{0.2}Fe_{0.8}O_{3-\delta}$) towards oxygen permeation and water splitting processes.
- Evaluation of the capability of the perovskite microtubes ($Ba_{0.5}Sr_{0.5}Co_{0.8}Fe_{0.2}O_{3-\delta}$, $La_{0.7}Sr_{0.3}FeO_{3-\delta}$ and $La_{0.6}Sr_{0.4}Co_{0.2}Fe_{0.8}O_{3-\delta}$) to transport oxygen ions across the membranes walls.
- Investigation of the feasibility of perovskite microtubes ($Ba_{0.5}Sr_{0.5}Co_{0.8}Fe_{0.2}O_{3-\delta}$, $La_{0.7}Sr_{0.3}FeO_{3-\delta}$ and $La_{0.6}Sr_{0.4}Co_{0.2}Fe_{0.8}O_{3-\delta}$) to produce hydrogen from water splitting and reducing gas (methane or carbon monoxide) activation.
- Investigation of catalytic activity of Palladium deposited by sputtering on the external surface of the microtubes for comparison with uncoated microtubes.
- Investigation of long duration operation and stability of membrane systems.
- Investigation of the effects of oxygen permeation and membrane-based steam reforming on the microtubes composition, microstructure and performance.
- Development of an autothermal membrane system for hydrogen production using methane as fuel.

Chapter 2

2 Membranes for hydrogen production

2.1 Introduction

The necessity of finding pathways to sustainability is driving researchers to find new energy sources for the future. Liquid fuels are still expected to remain the main source of energy, with already a major investment in 1st generation bio fuels (derived from biomass conversion) research [10, 11]. Bio fuels themselves will not address energy demand issues nor, according to European Environment Agency (EEA), global warming concerns [12]. Clearly new environmentally friendly energy technologies have to be developed.

Hydrogen as an energy carrier has the potential to provide energy with high efficiency and nearly zero emissions of pollutants when used in a fuel cell system [13, 14]. Demand for pure hydrogen has continuously increased in recent years, however currently hydrogen production technologies are energy intensive with many by-products associated; consequently purification is required making the overall process more expensive [15, 16].

This scenario has motivated researchers to improve methods of hydrogen production, separation and purification. Membrane technology shows great potential to substitute/integrate conventional methods for the production of pure hydrogen. Membrane processes also consume less energy and have the feasibility of operating continuously [17].

Hydrogen separation using polymeric membranes is already a well known technology; however these membranes present drawbacks, such as limited temperature application and sensitivity to certain chemicals [15, 17-19]. Hydrogen production and purification using inorganic membranes have attracted large interest due to the possibility of application under harsh conditions. However improvements in this technology such as stability and durability are still required for industrial applications [20, 21].

2.2 Conventional hydrogen production and separation methods

Hydrogen can be produced from different methods and from a variety of feedstocks as illustrated in Figure 2.1 [22]. Most of the hydrogen produced nowadays is derived from fossil resources, such as natural gas and coal; however alternative renewable energy resources (*e.g.* biomass and water) also can be used. Several methods can be applied such as chemical, biological, electrolytic, photolytic and thermochemical. The main issue is how to separate the hydrogen from other reaction products in an economically and efficient manner [23, 24].

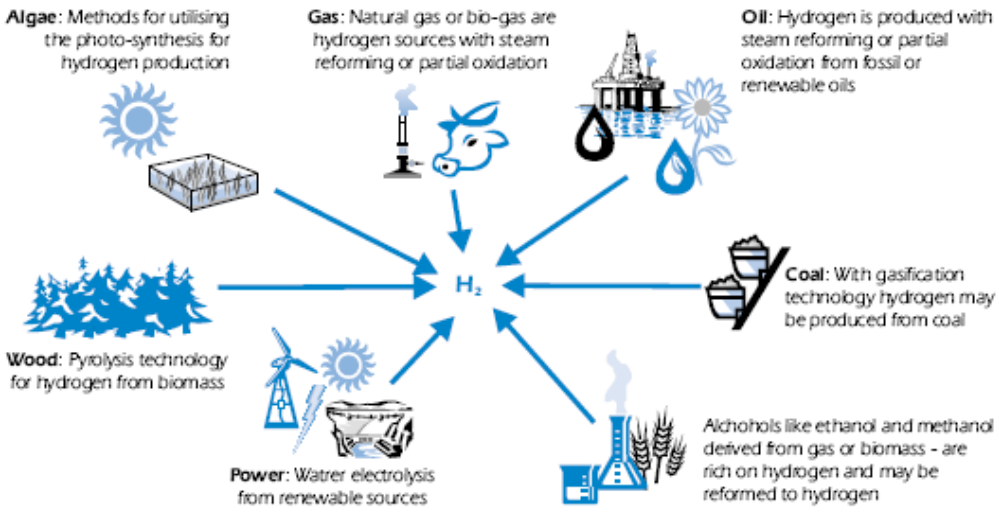

Figure 2.1 Hydrogen production pathways presenting different methods and variety of feedstocks [22].

The main hydrogen production methods and separation processes are presented and discussed further in this chapter. Other potential alternative, membrane-based steam reforming, which is the main objective of this work is presented in *Section 2.6.*

2.2.1 Hydrogen production from natural gas

Steam methane reforming (SMR) is the most conventional and well developed technology for hydrogen production [25, 26]. In this reaction methane is reacted with water vapour at elevated temperatures (700-850°C) in the presence of a supported nickel catalyst (Equation (2.1)). The reaction product is syngas (mixture of hydrogen and carbon monoxide), which contains approximately 12% of carbon monoxide, which can be converted to more hydrogen by the water-gas shift (WGS) step (Equation (2.2)). In this step carbon monoxide reacts with water vapour over a shift catalyst to produce

hydrogen and carbon dioxide. Other hydrogen method is the dry reforming of methane which produces syngas from carbon dioxide and methane, according to Equation (2.4).

$$CH_4 + H_2O \rightarrow CO + 3H_2 \qquad \Delta H^0_{298K} = +205\ kJ/mol \tag{2.1}$$

$$CO + H_2O \rightarrow CO_2 + H_2 \qquad \Delta H^0_{298K} = -41\ kJ/mol \tag{2.2}$$

$$CO_2 + CH_4 \rightarrow 2H_2 + 2CO \qquad \Delta H^0_{298K} = +247\ kJ/mol \tag{2.3}$$

Hydrogen can also be produced by the partial oxidation of methane (POM) as described in Equation (2.4) producing carbon monoxide and hydrogen. The carbon monoxide produced is further converted in hydrogen by WGS.

$$CH_4 + {}^1/_2\, O_2 \rightarrow CO + 2H_2 \qquad \Delta H^0_{298K} = -35\ kJ/mol \tag{2.4}$$

Other hydrogen production method is the autothermal reforming of methane which combines SMR (endothermic) with POM (exothermic) processes. The total reaction is exothermic and once more WGS is used to improve the hydrogen yields.

In order to achieve pure hydrogen in all methods mentioned a separation step is needed; the most common method used is pressure swing adsorption (PSA). This process involves capture of the impurities at higher pressure using a molecular sieve and then release of the impurities at low pressure. Hydrogen purities *ca* 99.9% may be obtained after the PSA process; however this separation technique is expensive and reduces the total efficiency of the overall process [27, 28].

Other separation techniques such as temperature swing adsorption (TSA) and cryogenic distillation could also be used to remove the impurities. TSA has a relatively long time operation and cryogenic distillation requires extremely low temperatures and therefore considerable amount of energy. Membrane systems have potential for hydrogen purification and have been successfully competing with conventional methods [18, 29, 30]. Hydrogen separation methods using membranes are discussed in *Section 2.3*.

2.2.2 Hydrogen production from water

Electrolysis is the process which water is split into hydrogen and oxygen using an electric current and an electrolyser (Equation (2.5)). Hydrogen obtained by electrolyses has a purity *ca* 99.99% being suitable for directly fuel cell applications. However

conventional electrolysis methods have not yet been competitive for large scale production due to high investment costs [31, 32].

$$H_2O \rightarrow H_2 + {}^1/_2\, O_2 \qquad (2.5)$$

Water electrolysis has gained great interest recently since the possibility of producing sustainable hydrogen in large scale. Electrolysis can result in zero greenhouses emissions if powered by renewable energy sources such as solar, hydroelectric, or wind [23, 33]. Therefore this method can compete with traditional methods such as steam methane reforming, especially with given expectations that fossil resources prices will continue to increase [34].

Direct thermal decomposition of water produces hydrogen splitting water in one step using heat. Since this process requires really high temperature (above 2000°C), multiple-step chemical reactions (thermochemical water splitting) are applied to lower the temperature and decompose water into hydrogen and oxygen. These processes are not industrially feasible yet due to many technical issues relate to high temperatures separation processes, corrosion, heat exchangers and heat sources [35, 36].

Photolysis is a developing method for hydrogen production which employs sunlight coupled with semiconductors materials (photovoltaic cells) to split water directly into hydrogen and oxygen. The technique is not yet economically competitive with other hydrogen production methods due to drawbacks related to semiconductors photocorrosion and low efficiencies [37-39].

Biophotolysis is a process in which certain microbes, such as green algae and cyanobacteria, capture sunlight energy after photosynthesis to split water and produce hydrogen as a by-product [40]. Genetic manipulation of the microbes has improved the process however slow hydrogen production rates is the main drawback to this technology [41, 42].

2.2.3 Hydrogen from biomass

Biomass is widely available from a variety of sources and can be converted for hydrogen generation by different technologies [42, 43]. Thermochemical processes are the most common methods as they operate at high temperatures and therefore obtain

high reaction rates. These processes involve either gasification or pyrolysis to produce a hydrogen-rich stream [44, 45].

Pyrolysis is used to produce bio fuels however its process can be adapted for hydrogen production. The process converts biomass into liquid and gaseous components by applying heat (370-550°C) under pressure (0.1-0.5MPa) in the absence of air (Equation (2.6)).

$$Biomass + heat \rightarrow H_2 + CO + CH_4 + \ other\ products \qquad (2.6)$$

The gaseous components are normally hydrogen, methane, carbon monoxide, carbon dioxide and other products depending of the nature of the biomass. In order to increase the hydrogen production SMR (Equation (2.1)) is applied followed by WGS reaction (Equation (2.2)).

During gasification biomass is converted into gaseous components by applying heat under pressure and in the presence of steam. The gaseous components are similar than in pyrolysis and subsequent series of chemical reactions produces syngas, which is also treated by SMR and WGS to improve hydrogen yields.

Thermochemical biomass processes use dry biomass, requiring a water content below 10 wt. %. However hydrothermal gasification processes requires an excess of water at increased temperature and pressure. The main advantage is that biomass, with a natural water content of 80 wt. % or more, can be converted without drying before. This process also has the advantage of having high reaction rates with a very low formation of undesired products like tars and coke [46].

Biomass conversion has the potential to be an economically renewable hydrogen production method and has already proved to be industrially feasible [47]. However over half of the hydrogen produced from biomass comes from SMR, consequently separation methods are required to purify the hydrogen produced. Conventional methods of separation are an expensive step of the process, thus membranes technology clearly can play an important role in this industrial sector [48, 49].

2.3 Membrane systems

Membranes are basically physical barriers which allow the transport across them of only selected species. The first known membrane experiment was performed by J.A. Nollet in 1748, he realised osmosis using a piece of pig's bladder [50]. However the first large scale gas separation membrane application was performed in the mid-1940s by the USA government for nuclear fuel enrichment [51]. Since then membrane technology for gas separation has received great attention.

The integration of membrane systems in hydrogen production processes represents a potential option for intensification of the process by decreasing energy utilization and equipment size. Membrane systems are energy saving as the process does not require any phase-transformation [19, 52], moreover their operation requires smaller units compared to other hydrogen separation plants. Most conventional hydrogen processes consists of a reactor unit coupled to a separation unit while membrane systems offers the opportunity to operate reaction/separation in a single unit. This innovative scheme intensifies hydrogen production.

Figure 2.2 shows a schematic of the membrane separation process, which most of the systems rely on pressure or concentration gradient as driving force for permeation from the feed stream to the permeated stream.

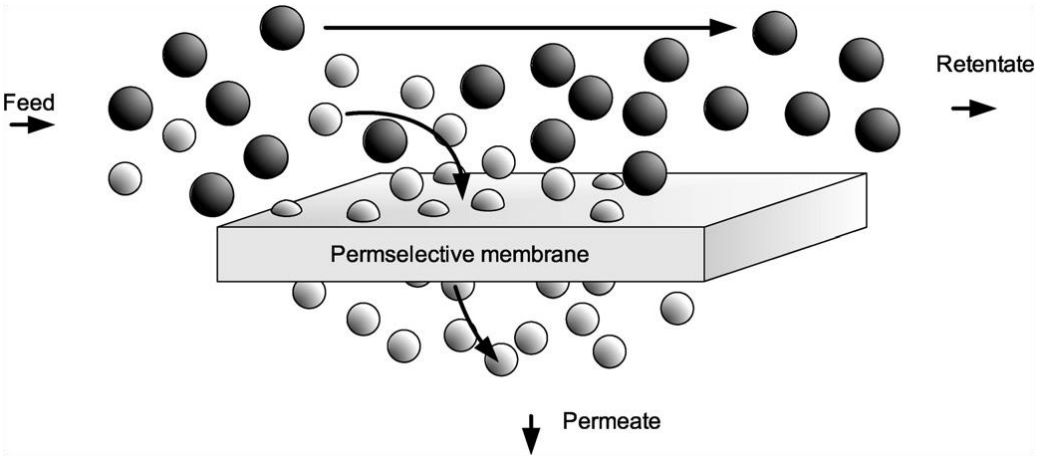

Figure 2.2 Schematic of membrane separation process showing transport from the feed stream to the permeated stream [18].

The performance of a membrane system depends of its selectivity and flux towards mixtures. Flux (J_x) is the total material transport through the membrane and can be expressed using Equation (2.7).

$$J_x = \frac{P}{t}(p^n_{x,feed} - p^n_{x,permeate}) \quad (2.7)$$

Where P is the species x permeability, t is the membrane thickness and $p^n_{x,feed}$ and $p^n_{x,permeate}$ are the species x partial pressures in the feed and permeate side, respectively. It is important to notice that the membrane thickness plays an important role in the overall process, since the permeation rate is increased when the thickness is minimised.

The separation factor can be expressed as the capability of a membrane to realise a given separation and is defined as the ratio of the permeability of the components in the membrane. The selectivity (α) of two components A and B can be defined as (Equation (2.8)):

$$\propto_{A/B} = \frac{P_A}{P_B} \quad (2.8)$$

Where P_A and P_B are component A permeability and component B permeability respectively. In the case of hydrogen separation, higher the selectivity more efficient is the process and therefore higher the purity of hydrogen produced.

Membranes can be classified into organic and inorganic and hybrids of organic/inorganic systems. Organic membranes are made of polymers and generally have some limitations related to high temperatures and resistance to harsh chemical environments. Inorganic membranes are made of glass, metal and ceramic materials and have attracted great interest as most of them can operate under high temperatures and withstand harsh environments [18, 53].

For hydrogen separation inorganic membranes can also be classified into dense and porous membranes. The gas separation through these membranes can be attributed to two mechanisms; through pores (porous membranes) and through the membrane material bulk (dense membranes). The most common hydrogen permeating membranes are the palladium alloys membranes, which separation mechanism can be described as solution/diffusion; a gas molecule is adsorbed in on side of the membrane wall, diffuses (in the form of ions and electrons or as atoms) through the bulk and associatively desorbs on the other side of the membrane [17, 54, 55]. Dense membranes generally have high selectivity, which is important factor for hydrogen purity, however they tend to present low fluxes. Other desirable properties are durability and stability (mechanical, chemical and thermal) under applied operation conditions [20, 56].

The scope of this work is limited to mixed ionic-electronic conducting membranes (MIEC) for oxygen separation; however a brief introduction of hydrogen perm-selective membranes and their properties are presented in the following section (*Section 2.3.1*).

2.3.1 Hydrogen perm-selective membranes

Hydrogen perm-selective membranes can be broadly separated in four categories; polymeric, metallic, carbon and ceramic [54]. Polymeric membranes for hydrogen separation are already commercially available, these are dense membranes therefore solution/diffusion is the mechanism to separate hydrogen from gaseous mixtures that generally consists of nitrogen, carbon monoxide, or hydrocarbons [17]. The advantages of polymeric membranes are their capability to resist high pressure drops and their low cost of raw material [56]. The main drawbacks of these membranes are the limited operation temperature (*ca* 100°C), mechanical strength and chemical resistance to certain chemicals such as hydrochloric acid, sulfur oxides and carbon dioxide [57].

Dense metallic membranes for hydrogen separation, in particular palladium and palladium alloys, are known to be high selective for hydrogen. High-purity hydrogen (up to 99.99%) can be obtained due to the higher diffusivity of only atomic hydrogen through palladium and its alloys (Figure 2.3) [58]. Membrane cost is an issue of this technology; to overcome this problem researchers have been focused on producing thin membranes, which also will increase hydrogen fluxes [59]. Techniques such as electroless-plating, chemical vapour deposition (CVD), sputtering and spray pyrolysis, have been used to apply thin palladium films on porous metallic or ceramic supports [60, 61]. Other disadvantage of these membranes is their high sensitivity to some gases such as hydrogen sulphide, hydrogen chloride and carbon monoxide [59, 62].

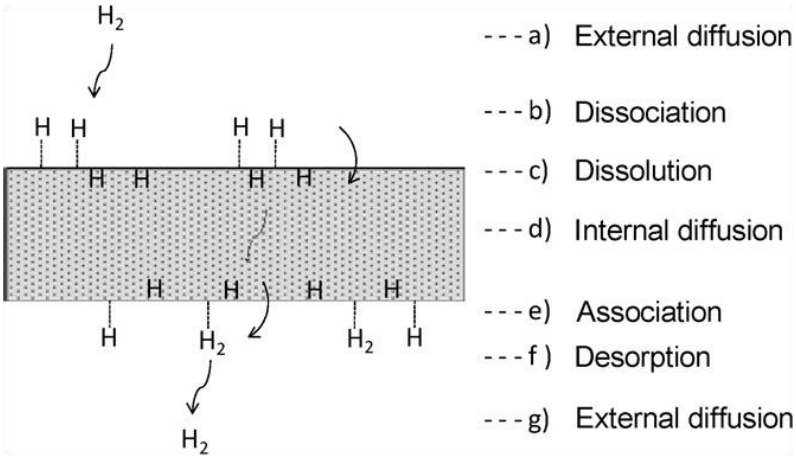

Figure 2.3 Hydrogen permeation through a dense palladium membrane showing the solution/diffusion mechanism [62].

Carbon membranes for hydrogen separation are divided into two groups based in the transport mechanism; surface diffusion and molecular sieving. Carbon molecular sieve membranes have received great interest due to great separation proprieties and stability, however large scale production still a challenge due to brittleness and fragility of carbon materials [63].

Ceramics membranes (porous and dense) for hydrogen separation have the advantage of being chemically inert and also resistant to high temperatures [64]. Porous ceramic membranes are usually made of alumina, zirconia, titania and silica and generally have a two-layer structure [54]. Dense ceramic membranes (proton exchange membranes) have high selectivity as only hydrogen ions can transport through the membrane. Material such as $SrCeO_{3-\delta}$ and $BaCeO_{3-\delta}$ are commonly used for having high proton conductivity, however their electronic conductivity is relatively low; hence hydrogen permeation fluxes are very low and considerable improvements in the process are still required for practical applications [65, 66].

2.3.2 Oxygen permeable membranes

The interest in dense oxygen permeable membranes increased after the development of ionic conducting materials for solid oxide fuel cells and sensors [67, 68]. These materials are mixed electronic ionic conductors thus the transport through the bulk is a combination of ions and electrons rather than molecular diffusion. Consequently a high selectivity for oxygen can be archived with MIEC membranes, which originally became of great interest due to the possibility of separating oxygen from air in an economically and feasible route. The most promising MIEC materials are the perovskite oxides which

present desirable properties, such as high oxygen flux when exposed to an oxygen gradient at temperatures above 700°C [69-71].

2.3.2.1 Perovskite

Of particular interest to this investigation are the MIEC perovskite-type membranes, which can exhibit high oxide ion conductivity due to their oxygen deficient nonstoichiometry [72]. These are ABO_3 structures in which large A ions are accommodate in a dodecahedral site while smaller B ions in an octahedral site as presented in Figure 2.4. The overall structure is very stable therefore the material has the capability of exchange a great range of metal cations at the A and/or B sites without changing its basic structure. This allows several modifications, such as doping strategies, to generate structure defects, which can create mobile oxygen vacancies and leading to higher oxygen ion mobility within the material lattice [73, 74].

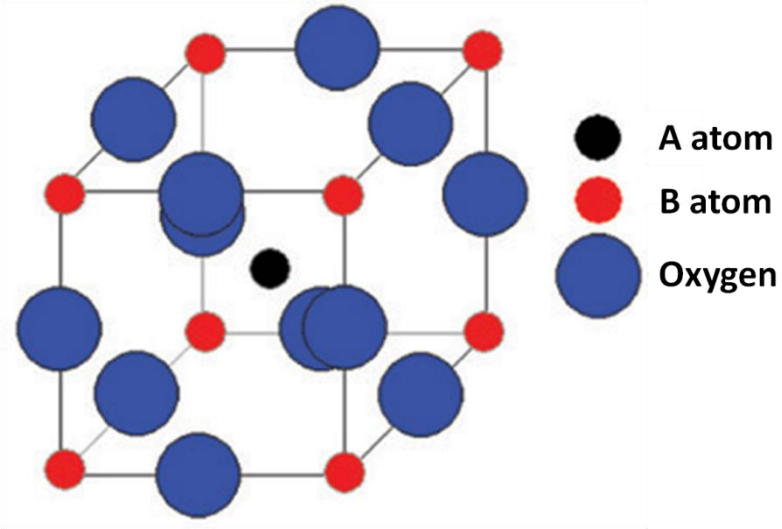

Figure 2.4 Ideal structure of ABO_3 perovskite in which oxygen vacancies are generated by replacement of A and/or B ions [75].

The ABO_3 perovskite structure allows a wide range of compounds to be produced with the introduction of either A´ and B´ atoms or both. The new structure can be described as $A_{1-x}A'_xB_{1-y}B'_yO_{3-\delta}$, where δ denotes the amount of oxygen vacancies. When these intrinsic defects are introduced the material becomes a useful conductor that can be employed for several applications.

The $La_{1-x}\,Sr_x\,Co_{1-y}Fe_yO_{3-\delta}$ perovskite family has been studied for a number of years, and due to its electronic and oxide anion conductivity has been applied for fuel cell cathodes and oxygen carrier membranes [70]. In particular $La_{0.6}Sr_{0.4}Co_{0.2}Fe_{0.8}O_{3-\delta}$ (LSCF6428)

membranes have been selected as potential oxygen carrier membranes and applied in this work to perform long term catalyst experiments. $Ba_{0.5}Sr_{0.5}Co_{0.8}Fe_{0.2}O_{3-\delta}$ (BSCF5582) and $La_{0.7}Sr_{0.3}FeO_{3-\delta}$ (LSF731) perovskite membranes were also investigated for their feasibility to split water and produce hydrogen.

2.3.2.2 Transport mechanism

Dense perovskite membranes when subjected to high temperatures and oxygen chemical potential difference (driving force for permeation) can transport oxygen from the presence of oxygen vacancies in the lattice of the membrane material. As the membrane is dense the transport of oxygen molecules is blocked, however oxygen dissociation and ionisation occurs at the high pressure side followed by migration of oxygen ions to the low pressure side. Simultaneously the flux of oxygen ions is charge compensated by a flux of electrons in the opposite direction. At the low pressure side the oxygen ions recombine to form oxygen molecules [76-78] (Figure 2.5).

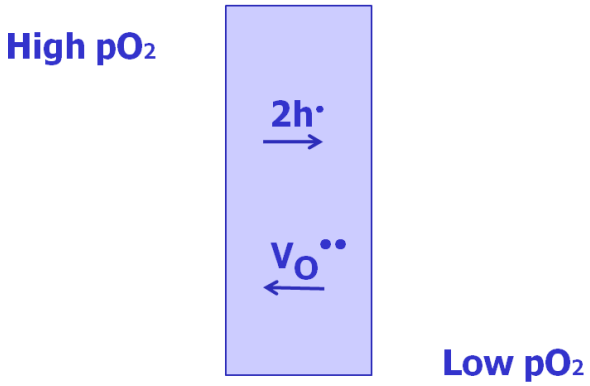

Figure 2.5 Schematic principle for oxygen transport throuhg mixed ionic electronic membranes at elevated temperature from high oxygen activity to low oxygen activity.

The reaction on the high pressure side can be written (using Kröger-Vink notation) as:

$$^1/_2\, O_2 + V_O^{\cdot\cdot} \rightarrow O_O^x + 2h^{\cdot} \qquad (2.9)$$

Where $V_O^{\cdot\cdot}$ denotes oxygen vacancies with a charge of +2, O_O^x lattice oxygen and $h^{\cdot}$ electrons holes. At the low pressure side oxygen ions are released creating an oxygen vacancy and donating two electrons back to the lattice of the membrane material (Equation (2.10)).

$$O_O^x + 2h^{\cdot} \rightarrow V_O + {}^1/_2\, O_2 \qquad (2.10)$$

This is feasible at high temperatures (700-1000°C) as the oxygen ions require enough thermal energy to overcome the energy barrier and hop from one crystallographic site to the other. An important factor is the fact these materials possess the ability to conduct both oxygen ions and electrons without the necessity of electrodes and external loadings, simplifying the membrane reactor and consequently the cost [75, 78].

Oxygen permeation through a dense membrane is controlled by (i) surface oxygen exchange (surface kinetics) and (ii) the rate of solid-state diffusion path the membrane length. When a MIEC membrane is under an oxygen partial pressure differential (Po_2), in a steady state, the oxygen permeation flux (jo_2) through the membrane can be expressed by Wagner equation (Equation (2.11)) [79]:

$$jo_2 = -\frac{RT}{(4F)^2 L}\int_{lnP'_{O_2}}^{lnP''_{O_2}} \frac{\sigma_{el}\sigma_{ion}}{\sigma_{el}+\sigma_{ion}} dlnPo_2 \qquad (2.11)$$

where R is the gas constant, T the temperature, F the Faraday constant and L the membrane thickness. P'_{O_2} and P''_{O_2} represent the oxygen partial pressure at the high and low Po_2 side of the membrane, respectively. The partial electronic and ionic conductivities of the material are represented by σ_{el} and σ_{ion} respectively.

For practical application it is interest to know whether the oxygen transport is controlled by bulk diffusion or surface exchange kinetics. From Equation (2.11) is evident that oxygen flux is inversely proportional to the membrane thickness; therefore higher oxygen flux can be obtained by reducing thickness. The oxygen permeation will be controlled by diffusion if the membrane has a thick wall, however reducing the membrane thickness, below a characteristic length L_c, surface exchange kinetics will predominantly control the oxygen permeation rate. L_c can be expressed in terms of self diffusion coefficient of oxygen ions (D_s) and surface exchange coefficients (k_s) by Equation (2.12) [78, 80].

$$L_c = \frac{D_s}{k_s} \qquad (2.12)$$

When membrane surface reaction is the rate determining step ($L \leq L_C$), oxygen permeation can be improved by surface modification; depositing a porous surface layer or by catalytic modification (or deposition), leading to an improvement of surface exchange kinetics [81].

2.3.2.3 Membrane geometry

Membrane geometry is an important aspect for achieve high oxygen permeation fluxes; membranes generally can be classified into: (i) planar and tubular membranes; (ii) symmetrical and asymmetrical.

Most of the oxygen permeation studies employ planar disk membranes due to easy fabrication method however tubular membranes have some advantages such as higher surface area and also simplicity to employ high temperature sealing. Microtubes (hollow fibres) membranes fabricated by phase inversion method have attracted great attention as they provide high surface area per unit volume when compared with disk membranes (Figure 2.6). Typically microtubular membranes have diameters range *ca* 1-2mm and membrane walls *ca* 0.2-0.3mm [82, 83].

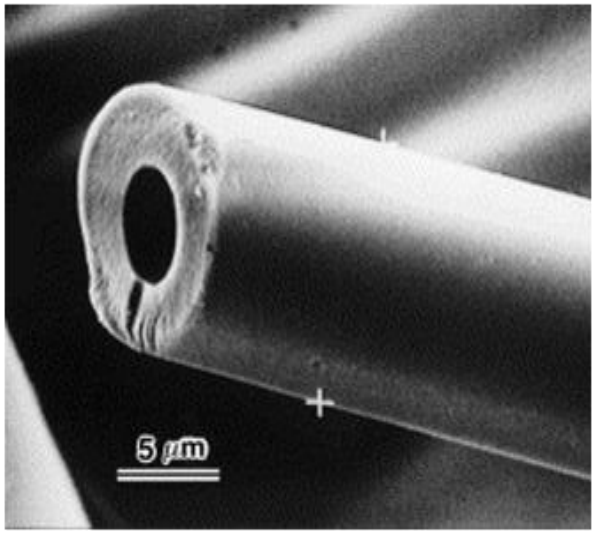

Figure 2.6 SEM image of a microtube (hollow fibre) membrane produced by phase inversion technique [84].

It is well know that oxygen flux can be increased by employing membranes with small wall thickness [85]. Thus another method of enhancing oxygen flux is using a dense ceramic layer on a porous support (asymmetric membranes). The dense film has to be a defect-free membrane, moreover the layer and the porous support must have thermal and chemical compatibility to assure a strong interface between them. This geometry allows the construction of more resistant membranes as the dense layer can be deposited on a mechanically strong support [86].

2.3.2.4 Applications

Oxygen separation from air using MIEC membranes is already a well known technology competing with conventional methods, such as cryogenic distillation of air and PSA. This technology have attracted great interest in industrial processes as they can provide separation and oxygen supply in one module unit; therefore the overall process becomes more efficient and costs are reduced [87-89].

Besides oxygen separation from air the integration of MIEC membranes in catalytic reactors is considered very promising. Partial oxidation of methane to synthesis gas (syngas) and oxidative coupling of methane to ethylene/ethane production are examples of these applications [73, 90-92]. However there are also a large number of potential applications in energy and environmental areas.

Partial oxidation of methane is probably one of the most important MIEC membranes applications. In this process oxygen is separated from air in one side of the membrane. The oxygen ions are transported through the membrane bulk to react with methane in the reaction side and produce hydrogen and carbon monoxide (syngas) (Figure 2.7). Air separation and reaction occurs in the same reactor avoiding multiple steps as applied in conventional method which can make the overall process energy intensive and expensive [20].

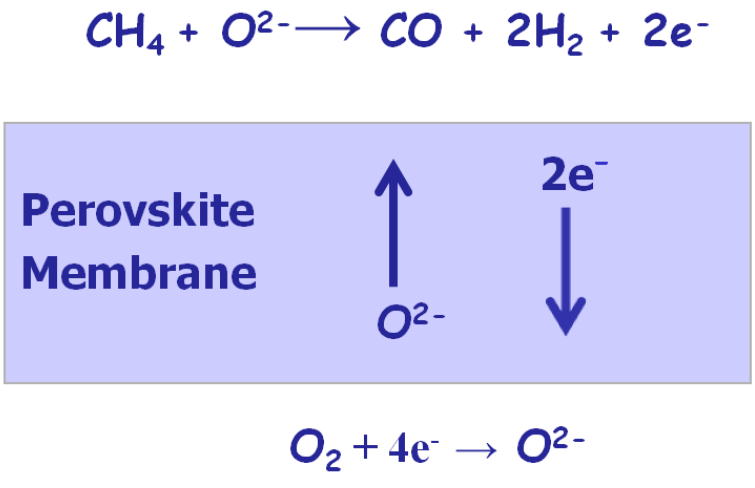

Figure 2.7 Partial oxidation of methane using MIEC membranes. Oxygen ions are transported through the membranes to react with methane to produce syngas.

Using the same principle of oxygen transport through MIEC membranes, pure hydrogen can be produced by water splitting and oxygen separation. This process combines

partial oxidation of methane and water splitting to produce hydrogen and syngas in separated streams (Figure 2.8). This process is described in detail in *Section 2.6.*

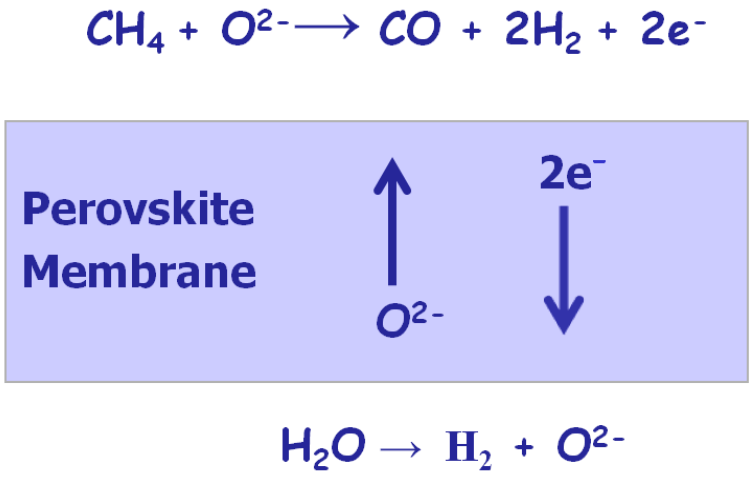

Figure 2.8 Membrane-based steam reforming using MIEC membranes. Oxygen ions are transported through the membranes to react with methane to produce separate streams of hydrogen and syngas.

2.3.2.5 Problems

Although several researchers have been investigating the feasibility of MIEC membranes for catalytic reactions, there are still many drawbacks to industrial applications. There are several major problems associated with long term stability and high temperature sealing of the membranes [93].

The performance of the oxygen carrier material plays a key role towards the selection of a MIEC membrane for a certain process; the membrane has to present thermal and chemical stability when exposed to high temperatures and large chemical potential gradients (*e.g.* air/methane). When such high chemical potential gradients are established the membrane can degrade which may lead to stress and total mechanical failure of the membrane. This degradation may happen due to lattice expansion mismatch of the different sides of the membranes, segregation of constituent cations, formation of different crystalline phases or formation of carbonates [94-97].

Segregation of constituent cations is often reported in studies involving MIEC membranes exposed to large chemical potential gradients [98-101]. This demixing phenomenon can be related to solid state transport mechanism in these OCMs, which can often be described as cation, oxygen anion and electron migration. In a ABO_3 perovskite oxide exposed to an oxygen potential gradient, demixing can occur if the

cations diffusion coefficient (D_A or D_B) are greater than the oxygen anion diffusivity (D_O). In the case of $D_A > D_B$ and $D_A \gg D_O$ the crystal (or membrane) normally will be enriched of A-site species at the high oxygen pressure side.

Another major issue to be solved is the high temperature sealing between the membranes and the vessels. This sealing has to withstand harsh environments and should not interact with the membrane surface (good compatibility). Membrane and sealing materials should have similar thermal expansions to avoid fractures and must perform over long periods. All these parameters are required to prevent mixing between the retentate and permeate streams [66, 102].

Other problems are related to relative low oxygen permeation flux and high energy required to operate most of the processes. Enhanced ionic electronic conductivity of the membranes and low energy processes (autothermal operation) are improvements still required for industrial applications [20, 66].

2.4 Oxygen transport membranes for hydrogen production

A number of hydrocarbon-conversion processes applying oxygen transport membranes (OTM) have recently been investigated with a few reviews published in the area [103-109]. The feasibility of POM and also other hydrocarbons to syngas production are the main subject studied in this area. These processes will be briefly discussed in *Section 2.5* however the scope of this literature review is to report the application of OTM to produce hydrogen from water-splitting (*Section 2.6*); this area has received little attention with fifteen publications since 1982. In these sections, oxygen permeation applications using OTMs are often recalled due to the similarity of the processes.

Of major importance, the oxygen material balance is a point which is rarely reported in works related to hydrocarbon-conversion processes. This material balance would characterise the oxygen transport through the membrane and also prove that hydrogen/syngas production is a direct result of oxygen permeation rather than surface reaction (structural oxygen at membrane surface). Both sides of the membrane gas outlet have to be analysed in order to perform this material balance, however most of the studies report only the outlet gas analysis from the permeated side.

Other aspects that are rarely reported are: (i) duration of operation, (ii) reporting the operating temperature for tubular membrane experiments, (iii) water conversion (in water splitting studies) and (iv) trans-membrane leaks. Relating to the first point it would seem obvious that durability of the membranes under experimental conditions should be an important aspect for any study in this area; often the duration of experiments is not presented or data is collected over a short period of time. Concerning to the second point, studies involving cold-sealed tubular membranes impose a temperature profile along the membrane length leading to different oxygen permeation rates along the membrane. Most studies assume that the membrane operating temperature is the same temperature set at the furnace. In relation to the third point, water splitting studies often do not report instruments for measuring water, such as hygrometers, nor simple calculations for estimating water conversion. Last but not least, most of the studies do not report trans-membrane leak which is an important aspect to investigate possible membrane and/or sealant failure.

2.5 Application of OTMs to syngas production from hydrocarbon sources

The first work with dense oxygen permeable membranes with high ionic and electronic conductivities was reported by Teraoka *et al.*; membranes with the general formula $La_{1-x}Sr_xCo_{1-y}Fe_yO_{3-\delta}$ presented higher performance for oxygen permeation than yttria stabilised zirconia [70, 71]. Since then new MIEC materials have been studied and also different applications have been tested.

One of the most studied applications for OTM membranes is the POM reaction for syngas production. The membrane controls the addition of oxygen to the reaction side as they incorporate oxygen into the oxygen sublattice (Equation (2.13)) and transport through the bulk.

$$^1/_2\, O_2 + V_O^{\cdot\cdot} \rightarrow O_O^x + 2e^- \qquad (2.13)$$

Where $V_O^{\bullet\bullet}$ denotes an oxygen vacancy at a site in the oxygen sub-lattice with a charge of +2, O_O^x denotes an oxygen occupying a site in the oxygen sub-lattice and e^- an electron. The oxygen anions transported react with methane in the other side of the membrane producing syngas (Equation (2.14)).

$$CH_4 + O_O^x \rightarrow V_O^{\cdot\cdot} + 2e^- + CO + 2H_2 \quad (2.14)$$

MIEC membranes are typically used in these studies [83, 90, 110-112]; bare membranes [83, 113, 114] and also membranes with the addition of a catalyst material to improve conversions have been investigated. Nickel has been applied in most of the studies involving catalyst material integrated with OTM membranes [112, 115-118]; this is mainly because of its capability to activate methane and therefore speed up the consumption of the oxygen that is transported across the membrane. Asymmetric membrane configurations also can improve performance; thin layers from the same [119, 120] or different material [121] of the membrane substrate have been used to improve permeation. Oxygen permeation is controlled by bulk and surface exchange rates; reducing the thickness of the membranes is a method used to reduce bulk transport limitations and consequently increase oxygen permeation.

Many techniques are used to apply thin dense layers such as dip coating, spin coating, sputtering and chemical vapour deposition; however the most prominent method to produce asymmetric membranes is the phase inversion technique. Membranes manufactured by this method (hollow fibres or microtubes) have an asymmetric geometry with a thin layer integrated [6, 122]. It is important to note that the sintering method also plays an important role is this process as removes the polymeric binder used during the process.

Membranes of $Ba_{0.5}Sr_{0.5}Co_{0.8}Fe_{0.2}O_{3-\delta}$ for oxygen permeation was first reported by Shao *et al.*[123]. Since then this material has received great attention due to high oxygen permeation rates reported [124] and promising application in methane oxidation studies [125]. Recent studies involving $Ba_{0.5}Sr_{0.5}Co_{0.8}Fe_{0.2}O_{3-\delta}$ microtubular membranes produced by phase inversion technique presented formation of $BaSO_4$ due to a reaction with polysulfone binder, commonly used in the phase inversion technique [7]. The authors stated this contamination affected bulk diffusion and surface kinetics and consequently lowered the oxygen flux across the membrane. The same group developed a new membrane using a sulfur-free phase inversion technique [8]. Post operation showed demixing of the cations constituents; however this has not affected stability of the membrane, which operated for oxygen permeation for *ca* 600 hours at the temperature range of 800-900°C. This work is of extreme importance to draw attention of researches which use phase inversion technique with polysulfone or polyethersulfone as a binder.

Membranes made of $La_{0.6}Sr_{0.4}Co_{0.2}Fe_{0.8}O_{3-\delta}$ perovskite showed good stability and relative high oxygen permeability under air/inert gas atmospheres [126]; therefore they also have been studied for methane oxidation to syngas production. Thursfield and Metcalfe [83] reported the dependence of methane conversion with the oxygen flux across the membrane in studies involving hollow-fibres. The authors stated complete methane conversion, leading to water and carbon dioxide, when high inlet oxygen flow rates were supplied at 860°C. However post methane oxidation studies indicated carbon deposition in the methane exposed side of the membranes, which may have restricted oxygen permeation rates. Segregation of metal constituents is another issue often reported in studies using $La_{0.6}Sr_{0.4}Co_{0.2}Fe_{0.8}O_{3-\delta}$ membranes [90, 98, 99, 127], this demixing process can affect performance of the membranes or even cause mechanical failure after long term operation as presented in *Section 2.3.2.5*.

Some researchers focused on the study of producing syngas from other hydrocarbon sources, such as heptane [128], ethane, propene and propane [129, 130]. However most of these studies have used coke oven gas (COG), which is a mixture gas generated in the production of coke from coal. The main components of COG are hydrogen (*ca* 54-59 mol%), methane (*ca* 24-28 mol%), carbon monoxide (*ca* 5-7 mol%), carbon dioxide (*ca* 1-3 mol%), nitrogen (*ca* 3-5 mol%), oxygen (*ca* 0.3-0.7 mol%), "other hydrocarbons" (*ca* 2-3 mol%) and hydrogen sulfide (*ca* 0.01-0.5 mol%) [131]. The researchers stated that conventional separation methods (PSA) only can separate hydrogen; partial oxidation can be used to obtain higher hydrogen yields from the other energetic components (*e.g*. methane, carbon monoxide) present in the COG.

Yang *et al* [132] have conducted partial oxidation of simulated COG to produce hydrogen at the temperature range of 800-900°C. The authors reported that a disk membrane of $Ba_{1.0}Co_{0.7}Fe_{0.2}Nb_{0.1}O_{3-\delta}$ with NiO/MgO reforming catalyst operated for continuous 100 hours at 875°C providing a hydrogen flux of *ca* 68μmol cm^{-2} s^{-1} (highest reported in COG studies) with 80% of hydrogen selectivity. High hydrogen production rates are reported in studies involving COG however is important to recall that the initial feed already has a high concentration of hydrogen (*ca* 58%). Post operation analysis showed that both sides of the membranes retained the original perovskite structure. However, demixing of constituents is often stated in these studies; *e.g.* barium segregation at the surface exposed to air and cobalt segregation at the surface exposed to COG have been reported in studies with $BaCo_{0.7}Fe_{0.2}Nb_{0.1}O_{3-\delta}$ membranes [133].

As mentioned before durability of the membranes are rarely reported, however some studies presented long term operations, such as Markov *et al.* who reported a 7500 hours continuous operation of a $La_{0.5}Sr_{0.5}FeO_{3-\delta}$ membrane for POM to syngas. Zhang *et al.* [133] also reported a long term experiment (550 hours) for hydrogen production from COG using a $BaCo_{0.7}Fe_{0.2}Nb_{0.1}O_{3-\delta}$ membranes.

2.6 Applications of OTMs to hydrogen production from water splitting

There are only a few publications concerning the application of OTMs to hydrogen from water splitting; composites materials, perovskites-type and non-perovskites oxides are examples of membrane materials used in these investigations. The application of different reducing gases have also been studied, gases such as hydrogen, carbon monoxide, ethane and methane have been applied to remove the oxygen permeated across the membranes. When methane is applied (*Section 2.6.4*) the overall process is the membrane-based steam reforming, which is the method used to produce hydrogen presented in this thesis.

The water splitting work is summarised in a table (adapted from review work published in Energy & Environmental Science [109]) and presented in Table 2.1. The table presents operating conditions employed and also significant results reported in each study. The results from *Chapter 6* of this thesis are also included in the table for completeness.

Hydrogen production from directly water splitting remains a major challenge because of its thermodynamic stability; however the equilibrium can be shifted toward dissociation if OTMs are applied to remove the oxygen from the gas phase during dissociation. Consequently the hydrogen production rate from water splitting will depend directly on the rate oxygen is removed from the dissociation side and consumed in the reaction side. Water splitting over an OTM membrane can be expressed in Kröger-Vink notation as (Equation (2.15)):

$$H_2O + V_O^{\cdot\cdot} + 2e^- \rightarrow O_O^x + H_2 \qquad (2.15)$$

At the reaction side oxygen is released creating an oxygen vacancy in the membrane crystal and also donating two electrons to counterbalance the electronic charge (Equation (2.16)).

$$O_O^x \rightarrow 2e^- + V_O^{\cdot\cdot} + \frac{1}{2}O_2 \qquad (2.16)$$

It is important to mention the ability of MIEC to conduct both ions and electrons without the necessity of an external circuit. The lack of electronic conductivity in the OTMs was the main issue reported by researchers in early work (1982) for hydrogen production from water splitting. To overcome this problem the authors operated the experiments at high temperatures (*ca* 1800°C) to achieve both electronic and ionic conductivities. Cales and Baumard and Lede *et al.* [134, 135] studied water dissociation using calcia-stabilised zirconia tubes to transport oxygen and produce hydrogen. A mix of carbon monoxide and carbon dioxide was applied as reducing agent to consume the oxygen permeated trough the zirconia wall. They also investigated the influence of temperature and partial pressure of oxygen on the permeated side (varying carbon monoxide to carbon dioxide ratio).

Naito and Arashi [5] in 1995 attempted to improve hydrogen production with the application of a MIEC tubular membrane at high temperature (*ca* 1600°C). The oxygen partial pressure on the permeated side was controlled by adjusting the gas mixture of hydrogen-carbon dioxide ratio. The authors also stated that the modified membrane (ZrO_2-TiO_2-$Y2O_3$) with higher electronic conductivity performed better than the bare membrane (ZrO_2-Y_2O_3).

This early work mainly focused on investigating the feasibility of the process and attempted to improve mixed electronic-ionic conductivities of the membranes. It became clear that membranes with higher ionic electronic conductivity were required to optimise the production of hydrogen from water splitting. With the improvements in material science engineering and membrane technology new MIEC membranes for oxygen permeation and POM were manufactured; therefore recent attempts to produce hydrogen from water splitting have been reported.

Table 2.1 Hydrogen production from water-splitting using oxygen transport membranes.

Oxide system	Membrane geometry	Membrane thickness (mm)	Catalyst	Gas composition(s) pH_2O (atm)	Gas composition(s) *p*Sweep (atm)	T range (°C)	Highest reported H_2 production rate per membrane unit area [a]	Longest reported operation period	Leak detection method reported/leak quantified	Material balance reported	Post op' analysis [d]	ref
$0.9ZrO_2$-0.1CaO	COE [b] tube	X	none	0.20	CO-CO_2 0.5-0.5	1400-1800	X	X	X	X	X	**[134]**
$0.9ZrO_2$-0.1CaO	COE [b] tube	X	none	0.20	(i) CO-CO2 mixes (ii) Ar 1.0	1500-1800	~2.2[c]	X	X	X	X	**[135]**
$(ZrO_2)_{0.8}$-$(TiO_2)_{0.1}$-$(Y_2O_3)_{0.1}$	COE [b] tube	2	none	0.17	H_2-CO_2	1600, 1683	0.4	X	"no leakage was found"	X	X	**[5]**
CeO_2-Gd-NiO	disk	0.1-1.5	none	0.03-0.49	(i) H_2 0.04-0.8 (ii) CH_4 0.05	700-900	4.1	X	X	X	X	**[136]**
CeO_2-Gd-Ni CeO_2-Gd-NiO	disk	0.1-0.36	none	0.49	H_2 0.04-0.80	500-900	6.8	X	X	X	X	**[137]**
$BaCo_xFe_yZr_{1-x-y}O_{3-\delta}$	microtube	0.17	Ni/Al_2O_3	0.05-0.75	CH_4 0.01-0.10	800-950	3.4	X	X	X	X	**[138]**
$BaCo_xFe_yZr_{1-x-y}O_{3-\delta}$	microtube	0.17	(i) none (ii) porous $BaCo_xFe_yZr_{0.9-x-y}Pd_{0.1}O_{3-\delta}$ surface layer	(i)-(ii) 0.75	(i)-(ii) CH_4 0.20	(i)-(ii) 800-950	(i) 0.47 (ii) 1.4	(i)-(ii) X	(i)-(ii) pressure test to 5 atm at 25°C & no trans-membrane N_2 at 800-950°C	(i)-(ii) X	SEM STEM EDS	**[139]**
$BaCo_xFe_yZr_{1-x-y}O_{3-\delta}$	microtube	0.17	none	0.75	C_2H_6 0.075 , 0.20	700-800	0.6	100 at 800°C	"gas-tight after 100 hrs"	X	SEM EDS	**[140]**
$BaCo_xFe_yZr_{1-x-y}O_{3-\delta}$	microtube	0.17	Ni/Al_2O_3	0.75	CH_4 0.04	850-950	2.2	X	O_2, $N_2 < 10^{-5}$ atm by GC	X	X	**[141]**
$La_{0.3}Sr_{0.7}FeO_{3-\delta}$	disk	3	none	X	CO X	860	0.01	20 at 860°C	No Ar and He detected	X	X	**[142]**

[a] where necessary derived from volumetric flux data and assuming STP ; [b] closed at one end ; [c] membrane area not given i.e., µmol s^{-1} ; [d] SEM scanning electron microscopy, XRD X-ray diffraction, EDS energy dispersive X-ray spectroscopy, STEM scanning tunnelling electron microscopy ; X not given

Continuation table hydrogen production from water-splitting using oxygen transport membranes

Oxide system	Membrane geometry	Membrane thickness (mm)	Catalyst	Gas composition(s) pH_2O (atm)	Gas composition(s) *p*Sweep (atm)	T range (°C)	Highest reported H_2 production rate per membrane unit area [a]	Longest reported operation period	Leak detection method reported/leak quantified	Material balance reported	Post op' analysis [d]	ref
$La_{0.7}Sr_{0.3}FeO_{3-\delta}$	disk	1-3	none	0.025	CO X	900	0.04	8 at 900°C	no trans-membrane Ar and He detected	X	X	**[143]**
$La_{0.7}Sr_{0.3}Cu_{0.2}Fe_{0.8}O_{3-\delta}$	(i) disk (ii) thin film	(i) 0.33-1.72 (ii) 0.05	(i) Pt and none (ii) Pt	(i)-(ii) 0.03-0.79	(i)-(ii) H_2 0.8	(i)-(ii) 600-900	(i) ~1.4 (ii) 7.8	(i)-(ii) X	no trans-membrane He detected	(i)-(ii) X	(i)-(ii) SEM	**[144]**
$La_{0.7}Sr_{0.3}Cu_{0.2}Fe_{0.8}O_{3-\delta}$	thin film	0.022	none	0.03-0.49	(i) CO 0.99 (ii) CO-CO_2 0.5-0.5 [(i)-(ii) simulated coal-gasification] (iii) H_2 0.8	(i)-(iii) 600-900	(i) 3.2 (iii) ~6.8	X	trans-membrane He detected	X	(i)-(iii) X	**[145]**
(i)$La_{0.7}Sr_{0.3}Cu_{0.2}Fe_{0.8}O_{3-\delta}$ (ii) $BaFe_{0.9}Zr_{0.1}O_{3-\delta}$	(i) supported tubular thin film (ii) disk	(i) 0.03 (ii) 1.6	(i)-(ii) none	(i) 0.49 (ii) 0.03-0.49	(i) CO 0.995 CO-CO_2 0.5-0.5 CO-CO_2 0.25-0.75 (ii) CO_2 0.8 / CO 0.8	(i) 500-900 (ii) 600-900	(i) 13.3 (ii) 0.2	(i) 80 (ii) X	(i)-(ii) trans-membrane He detected	(i)-(ii) X	(i)-(ii) SEM	**[146]**
$SrFeCo_{0.5}O_x$	(i) disk (ii) thin film	(i) 0.23-1.76 (ii) 0.02	(i)-(ii) none	(i)-(ii) 0.49	(i)-(ii) H_2 0.8	(i)-(ii) 900	(i) 11.9 (ii) 4	(i)-(ii) X	(i)-(ii) X	(i)-(ii) X	(i)-(ii) X	**[147]**
$La_{0.6}Sr_{0.4}Co_{0.2}Fe_{0.8}O_{3-\delta}$	microtube	0.25	none	0.07	CH_4 0.05	900	0.05[c]	260 & 400 at 900°C	10^{-4} atm O_2 & trans-membrane CH_4 monitored by GC	Carbon and oxygen	XRD SEM EDS	**This work**

[a] where necessary derived from volumetric flux data and assuming STP ; [b] closed at one end ; [c] membrane area not given i.e., μmol s^{-1} ; [d] SEM scanning electron microscopy, XRD X-ray diffraction, EDS energy dispersive X-ray spectroscopy, STEM scanning tunnelling electron microscopy ; X not given

2.6.1 OTM-based water splitting using hydrogen as reducing agent

Some studies applied hydrogen as a reducing gas to produce hydrogen from water splitting with the purpose of demonstrating the feasibility of the process. However it is clear that this procedure is a proof of concept and the use of hydrogen as a reducing agent to produce hydrogen is impractical (hydrogen produced equivalent to hydrogen consumed). Balachandran *et al.* [136] in 2004 reported the application of disk membranes made of gadolinium doped ceria (CGO) doped with nickel to produce hydrogen at the temperature range of 700-900°C. A higher hydrogen production rate than previous work in the area was reported at this range of temperature demonstrating the improvement in mixed ionic electronic conductivities of OTMs. The authors stated that hydrogen production increased with decreasing membrane thickness, showing bulk transport limitations. Hydrogen production rates also increased with the increase hydrogen (reducing gas) and water partial pressures. Other reducing gases were also investigated in this work; methane was shown to be less reactive than hydrogen and therefore the hydrogen production rate was lower than that obtained with hydrogen as the reducing gas. Hydrogen production concentration was measured by a gas chromatograph at the water side gas outlet of the membrane, however material balance was not possible as the reaction side gas outlet was not measured.

The same group attempted to improve the process by applying a porous layer of the same cermet (ceramic and metallic composite material) on the membranes [137]. Disk membranes of CGO/Ni and CGO/NiO were compared in this study; the application of nickel oxide instead of nickel improved hydrogen production and the surface reaction rates were enhanced by the application of the porous layers. The authors stated this layer extended the triple-phase boundary and therefore increased oxygen dissociation and recombination. However this layer did not affect membranes performance when the thickness was superior to 2mm where oxygen transport was controlled by bulk diffusion.

Balachandran's group in 2008 studied the application of a single phase MIEC disk membrane made of $SrFeCo_{0.5}O_x$ for water splitting at 900°C [147]. The driving force was established with a water partial pressure of 0.49 atm (water feed) and 0.8 atm of hydrogen as sweep (reducing gas). This membrane performed better than the CGO membranes, however when applied at temperatures *ca* 850°C the performance

decreased dramatically as the material undergoes phase transition at temperature range of 825-850°C. The membrane thickness and the deposition of porous layers were investigated. Bulk limitation was observed as the highest hydrogen production rate (11.9 μmol cm^{-2} s^{-1}) in this work was achieved with a really thin membrane of 20 μm thick.

Perovskite-type $La_{0.7}Sr_{0.3}Cu_{0.2}Fe_{0.8}O_{3-\delta}$ disk membrane has also been tested for water splitting using hydrogen as a reducing gas [148, 149]. Porous support with a thin film (*ca* 50μm), both made of $La_{0.7}Sr_{0.3}Cu_{0.2}Fe_{0.8}O_{3-\delta}$, was coated with a platinum catalyst layer to improve kinetics; a high hydrogen production rate of *ca* 7.8 μmol cm^{-2} s^{-1} was reported when the membranes operated at 900°C. Post operation SEM analysis showed that the membrane surfaces did not present any fragments or porosity. However the authors have not presented long term operation.

2.6.2 OTM-based water splitting using ethane as reducing agent

Jiang *et al*. [140, 141] investigated the feasibility of producing hydrogen combining water splitting and ethane dehydrogenation at moderate temperatures (700-800°C). The authors have investigated the performance of a microtubular (hollow-fibre) $BaCo_xFe_yZr_{1-x-y}O_{3-\delta}$ membrane during 100 hours of operation; the hydrogen production rate showed direct dependence on temperature and oxygen partial pressure. The membranes provided 60% ethane conversion and 90% ethene selectivity with water disassociation giving a rate of hydrogen production of *ca* 0.6 μmol cm^{-2} s^{-1}. Post operation SEM analysis showed erosion of the membrane surface (*ca* 10μm deep) exposed to ethane however the authors stated that this had not affected the membrane performance as no cracks were detected and the membrane was still gas-tight after 100 hours of operation when the test was stopped. This is an important point as few researchers report membrane integrity of the membranes when the experiments are complete.

The use of ethane as a reducing agent raises an important aspect in these oxidation/reduction studies; investigate reactivity of different reducing gases under experimental conditions. An interesting study reported by Shen *et al*.[150] investigated the reactivity of the main components in COG (hydrogen, methane and carbon monoxide) in order to understand the reaction mechanism for COG reforming using

$BaCo_{0.7}Fe_{0.2}Nb_{0.1}O_{3-\delta}$ membranes. The authors stated that hydrogen consumes the oxygen permeated at the OTM surface faster than carbon monoxide, which in turn consumes the oxygen permeated faster than methane (H2 > CO > CH4). This was concluded from experiments in which individual components of hydrogen, methane and carbon monoxide diluted in argon were fed into the OTM reactor and the rates of oxidation for each obtained.

2.6.3 OTM-based water splitting using carbon monoxide as reducing agent

Water-gas shift reaction has attracted recent attention in membrane reactors for hydrogen production. In this case water dissociates in one side of the membrane (Equation (2.17)).

$$H_2O + V_O^{\cdot\cdot} + 2e^- \rightarrow O_O^x + H_2 \quad (2.17)$$

At the reaction side carbon monoxide reacts with lattice oxygen to produce carbon dioxide, oxygen vacancies $V_O^{\bullet\bullet}$ and electrons (Equation (2.18)).

$$CO + O_O^x \rightarrow CO_2 + V_O^{\cdot\cdot} + 2e^- \quad (2.18)$$

Resulting in the overall water-gas shift reaction (Equation (2.19)):

$$H_2O + CO \rightarrow H_2 + CO_2 \quad (2.19)$$

Evdou *et al*. [142] studied the feasibility of hydrogen production using a disk $La_{0.3}Sr_{0.7}FeO_3$ membrane; hydrogen could be produced continuously at the temperature of 860°C however essential experimental conditions *e.g.* partial pressure of the inlet carbon monoxide and water are not provided in this work. The authors stated that hydrogen could be produced without the assistance of the reducing gas after a few hours (initial activation) of experiments; the supply of carbon monoxide was interrupted and switched to an inert gas. The membrane continued to produce a lower level of hydrogen during 10 hours. The same authors also investigated the $La_{0.7}Sr_{0.3}FeO_3$ disk membrane under the same experimental conditions, however at the temperature of 900°C [143]. The same capability of producing hydrogen without the assistance of a reducing gas, after an initial activation, was reported. Bulk transport limitations were also observed as

thinner membranes (1mm thick) provided higher oxygen flux than membranes 3mm thick.

Even though both studies of Evdou *et al.* [142, 143] for hydrogen production operated at different temperatures and direct comparison is not adequate, it is worthwhile to notice the effect of strontium doping in the $La_{1-x}Sr_xFeO_{3-\delta}$ family. Higher oxygen flux was obtained with the perovskite containing high strontium concentration ($La_{0.7}Sr_{0.3}FeO_3$). A similar trend was also reported by Elshof ten *et al.*[101], who also reported enhancements in the oxygen flux when the strontium concentration was increased from x = 0.1 to x = 0.3. The authors indicated that higher oxygen vacancies can be obtained by increasing strontium contents; however this enhancement in oxygen flux cannot be directly related only to the strontium content increase.

Park *et al*. [146] performed a study with two different materials and geometries; $La_{0.7}Sr_{0.3}Cu_{0.2}Fe_{0.8}O_{3-\delta}$ tubular and $BaFe_{0.9}Zr_{0.1}O_{3-\delta}$ disks membranes have been used to perform hydrogen production at the temperature range of 500-900°C. A thin film (30 μm) of $La_{0.7}Sr_{0.3}Cu_{0.2}Fe_{0.8}O_{3-\delta}$ was deposited in a tubular substrate of the same material to ensure good interface between them; the membrane operated during *ca* 80 hours showing a high hydrogen production rate (13.3 μmol cm^{-2} s^{-1}) at 900°C. Post operation SEM analysis revealed some porosity however the membrane surfaces did not present cracks. The authors did not present direct comparison between tubular $La_{0.7}Sr_{0.3}Cu_{0.2}Fe_{0.8}O_{3-\delta}$ and $BaFe_{0.9}Zr_{0.1}O_{3-\delta}$ disks, nevertheless they indicated that $BaFe_{0.9}Zr_{0.1}O_{3-\delta}$ membranes have the potential to perform better than $La_{0.7}Sr_{0.3}Cu_{0.2}Fe_{0.8}O_{3-\delta}$; however a better understanding of $BaFe_{0.9}Zr_{0.1}O_{3-\delta}$ defect chemistry is required.

The use of carbon monoxide as sweep gas was also investigated in oxygen permeation studies in the $La_{1-x}Sr_xFeO_{3-\delta}$ family; Elshof ten *et al.*[101] reported strontium segregation after 48 hours of operation, which lead to the formation of SrCO and/or SrO. The authors stated that the main perovskite composition remained however SEM analysis indicated an enlargement of the specific surface area. Similar oxygen permeation studies at 900°C with $La_{0.6}Sr_{0.4}Co_{0.8}Fe_{0.2}O_{3-\delta}$ using carbon dioxide as reducing gas presented carbon deposition, strontium segregation and also corrosion of the membrane surface after 100 hours [100]. The authors stated that oxygen permeation decreased due to chemical adsorption of carbon dioxide on the membrane surface with oxygen atoms of carbon dioxide occupying the oxygen vacancy sites. Perhaps the use of

less reactive reducing agent (e.g. methane) may prevent membrane instability and material segregation.

2.6.4 OTM-based water splitting using methane as reducing agent

Membrane-based steam reforming has also been demonstrated as a good candidate for hydrogen production by water splitting [136, 138, 139, 141]. This process combines POM and water splitting to produce syngas and hydrogen in separate streams of the membrane.

The oxygen generated from water splitting is transported through the membrane to the reaction side (Equation (2.20)):

$$H_2O + V_O^{\cdot\cdot} + 2e^- \rightarrow O_O^x + H_2 \quad (2.20)$$

At the reaction side methane reacts with lattice oxygen to produce syngas, oxygen vacancies,$V_O^{\bullet\bullet}$ and electrons (Equation (2.21)).

$$CH_4 + O_O^x \rightarrow V_O^{\cdot\cdot} + 2e^- + CO + 2H_2 \quad (2.21)$$

Resulting in the steam methane reforming reaction (Equation (2.22)):

$$CH_4 + H_2O \rightarrow CO + 3H_2 \quad (2.22)$$

This process produces pure hydrogen if the membrane is gas-tight as the hydrogen stream never meets the reducing gas stream. Unconverted water can be condensed and pure hydrogen can be collected; this process avoids any expensive hydrogen purification method *e.g.*, pressure swing adsorption or cryogenic distillation.

Jiang *et al*. [138] investigated the process using a $BaCo_xFe_yZr_{1-x-y}O_{3-\delta}$ microtubular membrane with wall thickness *ca* 170 μm; a nickel-based reforming catalyst was packed around the membrane to accelerate the conversion of methane. The influence of temperature at the range of 800 to 950°C was investigated; the highest hydrogen production rate (3.4 μmol cm^{-2} s^{-1}) was obtained at 950°C. Low methane conversions and low carbon monoxide selectivity were observed when a high concentration of methane was fed at the reaction side. The authors indicated this occurred due to carbon deposition at the membrane surface exposed to methane; however no post operation

analysis were presented to provide this evidence. Under such conditions the question of long term stability must be addressed, the authors did not provide any long term studies and it is not clearly stated whether data was collected with the same membrane or different sets of membranes while the influence of temperature and inlet gases concentration was studied. The same group [141] studied the performance of $BaCo_xFe_yZr_{1-x-y}O_{3-\delta}$ membranes with a nickel-based catalyst for membrane-based steam reforming (and also dehydrogenation of ethane with nitrous oxide reduction). The highest hydrogen production rate reported was 2.2 μmol cm^{-2} s^{-1} at 950°C.

Some attention has also been given to surface modification of $BaCo_xFe_yZr_{1-x-y}O_{3-\delta}$ microtubular membranes [139]. A $BaCo_xFe_yZr_{0.9-x-y}Pd_{0.1}O_{3-\delta}$ thin porous layer (40 μm thick) was deposited to improve catalytic performance to methane oxidation. The authors stated that good mechanical stability of the membranes since the porous layer and the substrate have almost the same melting point; therefore good interface compatibility was obtained. A higher hydrogen production rate was obtained with the surface modified membrane compared with the bare membrane; the highest hydrogen production rate presented was of *ca* 1.4 μmol cm^{-2} s^{-1} at 950°C. The enhancement was attributed to the well known activity of palladium catalysts towards methane activation. Gas analysis of the methane feed side exit was not reported; thus oxygen balance and a correlation between oxygen flux and water splitting cannot be made.

2.6.5 Summary

It is important to notice that material balance was not possible in most studies involving water splitting as gas analysis was only performed on the water feed-side to detect hydrogen. Hence it is not possible to demonstrate that hydrogen production is directly related to oxygen permeation across the OTMs. Another omission is the duration of operation; few workers reported long term experiments or did not report at all. The longest reported continuous hydrogen production from water splitting is 100 hours using a $BaCo_xFe_yZr_{1-x-y}O_{3-\delta}$ microtubular membrane with ethane as a reducing agent [140].

Few workers specifically reported the hydrogen production rate; the highest reported flux from OTM-based water splinting work is *ca* 13.3 4 μmol cm^{-2} s^{-1} obtained with a $La_{0.7}Sr_{0.3}Cu_{0.2}Fe_{0.8}O_{3-\delta}$ supported tubular thin film (*ca* 30 μm) [146]. Membrane thickness is definitely an aspect which requires some attention. Thinner membranes are

necessary to enhance oxygen permeation thus hydrogen production. Post-operation analysis is another important point very often neglected in these studies. This analysis can provide useful information about membranes stability/failure over time. This leads to other aspect rarely reported; few workers reported whether/when the membranes presented failure and stopped to perform on the way expected. Finally, another aspect not fully reported is the history of the membranes prior and during operation.

Oxygen permeation in MIEC membranes is controlled by both bulk diffusion and surface kinetics. Most of the studies which reported high oxygen permeation flux attempted to reduce bulk limitation processes by producing membranes with thin dense walls or layers. Many researchers used the phase inversion technique, which is the most prominent method to produce asymmetric membranes with thin dense layer integrated.

This project aims to study the feasibility of perovskite-type membranes (manufactured by phase inversion technique) to produce hydrogen from membrane-based steam reforming over long duration where permeation is more important than dynamic surface redox processes. Analysis of exit gas composition from both sides of the membranes in order to realise a careful oxygen balance will be conducted. Also methods to improve stability of the membranes (*e.g.* operate under lower water partial pressure and methane concentration) will be carried out.

Chapter 3

3 Experimental

3.1 Introduction

This chapter details all fabrication procedures and experimental setups used in this work. The methods used for fabrication/sintering of the microtube membranes and their final dimensions are presented in *Section 3.2*. Temperature programmed studies aimed to compare and select the best material available for hydrogen production by water splitting/methane reforming. *Section 3.3* illustrates the materials used and the experimental setup of these catalytic activity studies. The membrane module design and experimental setup for experiments involving membranes are presented in *Section 3.4.* An outline of the methodologies applied for the oxygen permeation studies and membrane-based steam reforming are presented in *Section 3.5* and *Section 3.6* respectively.

3.2 Membrane fabrication

$La_{0.6}Sr_{0.4}Co_{0.2}Fe_{0.8}O_{3-\delta}$ (LSCF6428), $La_{0.7}Sr_{0.3}FeO_{3-\delta}$ (LSF731) and $Ba_{0.5}Sr_{0.5}Co_{0.8}Fe_{0.2}O_{3-\delta}$ (BSCF5582) microtube membranes were used during this work. LSCF6428 and LSF731 microtubes were prepared by Zhentao Wu at Imperial College London and BSCF5582 microtubes were manufactured by Cedric Buysse at VITO NV, Belgium.

The dense gas-tight LSCF6428 microtube membranes were manufactured by the phase inversion/sintering method (Figure 3.1) described by Tan *et al* [6] using LSCF6428 commercial powder with a surface area of 6.0 m^2/g and $d_{50} < 1$ µm manufactured by combustion spray-pyrolysis (Praxair). LSF731 microtube membranes were produced by similar process than LSCF6428, using LSF731 commercial powder with a surface area of 5.5 m^2/g and $d_{50} < 0.7$ µm also manufactured by Praxair. BSCF5582 microtube membranes were also prepared by phase inversion/sintering method described elsewhere [7] using BSCF5582 powder with a surface area of 1.2 m^2/g and $d_{50} = 3$ µm manufactured by HITK (Hermsdofer Institut für Techinische Keramik).

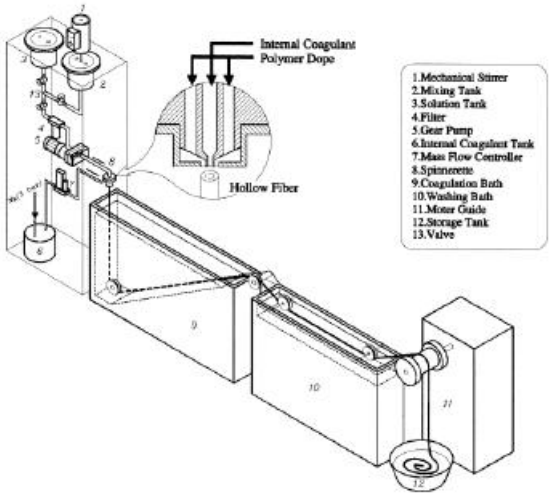

Figure 3.1 Schematic apparatus for microtubes fabrication by phase inversion [151].

Crystallinity and phase purity of the membranes were determined by powder X-ray diffraction (XRD) using a PANalytical X'Pert Pro Multipurpose Diffractometer (PW3040/60) fitted with an X'Celerator and a secondary monochromator. For data acquisition, the Cu anode was supplied with 40 kV and a current of 40 mA to generate Cu K-α radiation (λ = 1.54180 Å) or Cu K-α1 (λ = 1.54060 Å). A nominal step size of 0.0334 two-theta and time per step of 100 s in continuous mode was routinely used. A Rontec Quantax 1.2 FEI XL30 ESEM-FEG system was used to carry out microstructure characterisation by scanning electron microscopy (SEM) and elemental analysis by energy dispersive X-ray spectroscopy (EDS). SEM images of the cross-sections of the fresh microtubes are provided in Figure 3.2. The dimensions of the sintered microtubes are presented in Table 3.1.

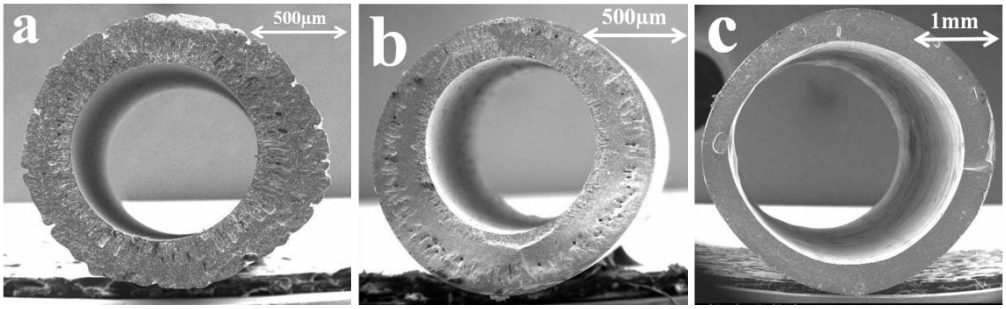

Figure 3.2 SEM images of the membrane cross sections of (a) LSCF6428, (b) LSF731 and (c) BSCF5582.

Table 3.1 Dimensions of the sintered microtube membranes.

Microtube	Outer diameter (≈ mm)	Inner diameter (≈ mm)	Wall thickness (≈ mm)	Total length (≈ cm)
LSCF6428	1.5	1.0	0.25	30.0
LSF731	1.4	0.9	0.25	30.0
BSCF5582	3.5	2.7	0.4	25.0

3.3 Temperature programmed experiments

3.3.1 Material preparation and characterisation

Dense membrane fragments with dimensions *ca* 3mm (*ca* 50 mg of material) from LSCF6428, LSF731 and BSCF5582 microtubes and commercial LSCF6428, LSF731 and BSCF5582 powders (Praxair) were used without further processing.

Surface area analysis was carried out on each powder sample with a Coulter 3100A using N_2 as adsorbate at 77K with BET (Brunauer-Emmett-Teller) analysis. All samples were also characterised by SEM and EDS.

3.3.2 Apparatus

Temperature programmed reaction experiments were performed using a fully automated and programmable microreactor-gas analysis system (CATlab, Hiden Analytical, UK) at 1atm. The system consists of a microreactor and a quadrupole soft ionisation mass spectrometer (QMS) for analysis. The outlet of the microreactor is connected to the QMS via a heated capillary line to avoid condensation. Calibration was carried out and described by Murugan *et al* [152].

To generate fast responses usually *ca* 50 mg of sample was placed in the quartz microreactor (plug flow reactor) integrated with internal K-type thermocouple to control and monitor the temperature. Reduction and oxidation of the material was performed by alternating the flow of reducing and oxidation gases. The products were sent to the QMS for gas analysis.

Water was fed into the microreactor by a water saturator system (Grant Scientific, UK) using helium as a carrier gas. The concentration of the water could be controlled by the temperature of the water bath and monitored by a platinum cold mirror dew point

hygrometer (CMH-1, Alpha Moisture Systems, UK). This unit was also used to calibrate the water signal for the QMS.

3.3.3 Temperature programmed experiments procedure

The sample (*ca* 50mg) was placed inside the microreactor and immediately was flushed out under a helium flow of 100 (STP) ml min^{-1} prior to testing to evacuate the air from the sampling tube. The furnace temperature was raised to 900°C, under a helium atmosphere, using a ramp of 10°C min^{-1}. Fifteen isothermal redox cycles were performed at 900°C using alternating flows of 5% methane in helium and then 2.6% water in helium, each supplied at a total inlet flow rate of 20 ml min^{-1}. Reduction and oxidation steps were performed for 30 minutes. Following the experiment the sample was removed for post operation analysis (SEM-EDS analysis).

3.4 Membranes experimental setup

Oxygen permeation and membrane-based steam reforming experiments for this work were performing using an experimental setup illustrated in Figure 3.3. This setup can be divided in three sections; the feed system, membrane reactor plus furnace and the analysis system. Pictures of the experimental setup are presented in *Appendix 3-A.*

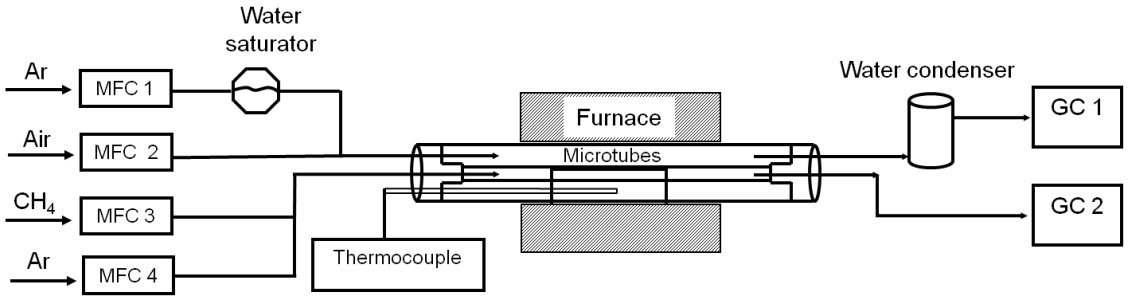

Figure 3.3 Schematic of the experimental setup for oxygen permeation and membrane-based steam reforming experiments.

3.4.1 Feed system

The gases supplied to the membrane module are controlled by four mass flow controllers (MFC) (Brooks, UK) connected to different gas cylinders as presented:

- MFC 1: Compressed argon (BOC, UK)
- MFC 2: Compressed air (BOC, UK)
- MFC 3: 5% methane in argon (BOC,UK)
- MFC 4: Compressed argon (BOC, UK)

During oxygen permeation MFC 2 is used to supply air to the feed side of the membranes and MFC 4 to supply sweep argon to the other side. During membrane-based steam reforming MFC 1 is used to supply water vapour plus argon to the shell side of the membranes and MFC 3 to supply methane to the lumen side. The water was delivered by a water saturator system (Grant Scientific, UK), which water bath (Figure 3.4) temperature could be varied to control the saturation of the water.

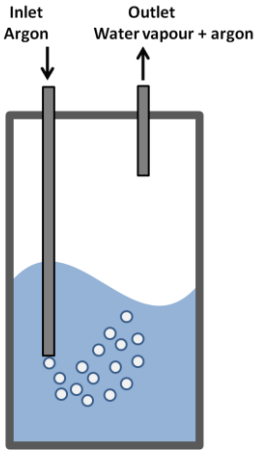

Figure 3.4 Schematic diagram of the water saturator system.

The concentration of water leaving the water saturator was monitored and also calibrated by a hygrometer (VAISALA HMT330). The water concentration could be adjusted (at equilibrium) according to the water saturator calibration curve show in Figure 3.5. The results from this calibration test are presented in *Appendix 3-B*, they slight diverge from the typical water vapour pressure table. This variation could be related to actual fluctuation in inlet flow rates or temperature and/or pressure. The other factor that cannot be neglected is condensation, which is a common problem in systems that user water as a reactant. To avoid condensation heating lines at 80°C were used between the water saturator and the membrane module and also between the membrane module and the gas chromatograph GC 1 (Varian 3900).

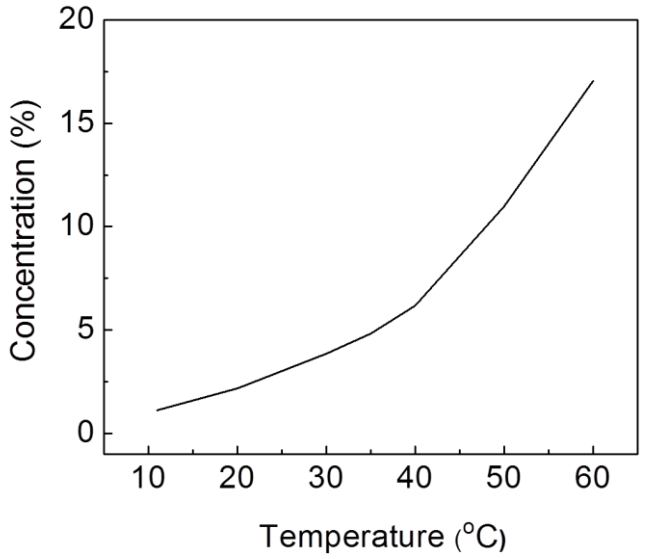

Figure 3.5 Water saturator calibration curve.

3.4.2 Furnace

The membrane module was placed inside a furnace (Vecstar Furnaces, UK) which was used to heat the membranes using a programmed temperature ramp to the required operating temperature which was measured by an internal thermocouple. Two custom-made furnaces were used to run the experiments:

- SW furnace (short length and wide bore) - total length of 10 cm with a bore diameter of 5 cm.
- LN furnace (long length and narrow bore) – total length of 15 cm with a bore diameter of 4 cm

Most of the experiments were run at the temperature of 900°C; therefore temperature profiles at the interior of the reactor module at this temperature were recorded for both furnaces and presented in Figure 3.6. The thermocouple was originally placed at the centre of the membrane module and then moved out in 0.5 cm steps to the end-caps of the reactor. It was assumed that the furnaces had symmetrical temperature profiles.

Isothermal zone lengths of 3 cm and 5 cm at the centre of the membrane modules were measured using the SW furnace and LN furnace, respectively. The experimental setup ensures that in both cases the sealing points are situated in the “cold” zone outside of the furnace at the temperature of *ca* 100°C.

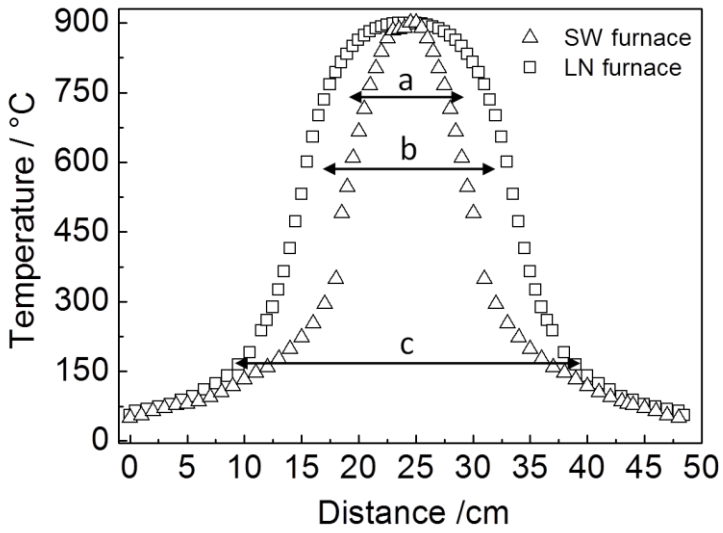

Figure 3.6 SW and LN furnaces; internal temperature profile of reactor at 900°C. Horizontal lines indicate (a) total heated length of membranes using SW furnace, (b) total heated length of membranes using LN furnace and (c) total length of membranes used during the experiments.

3.4.3 Membrane module

3.4.3.1 1st membrane module design

During the first year of this research a membrane module design illustrated in Figure 3.7 was tested for oxygen permeation and redox experiments. In this membrane module the microtubes are contained in a quartz tube which has 40 cm in length with an internal diameter of 3.2 cm and external diameter of 3.6 cm. The shell tube is closed with two aluminium end-caps; one cap containing three longitudinal holes and the other two holes. The central holes from the end-caps were connected to the microtubes lumen-side (the inner side) and the other holes connected to the membranes shell-side (the outer side). Four holes of the end-caps were attached to two pairs of gas inlet/outlet made of stainless steel (Swagelok compression fittings with 1/8 in). A K-type thermocouple was housed inside an inert alumina sleeve and inserted in the remaining hole from the end-cap. The thermocouple is free to move along the length of the module.

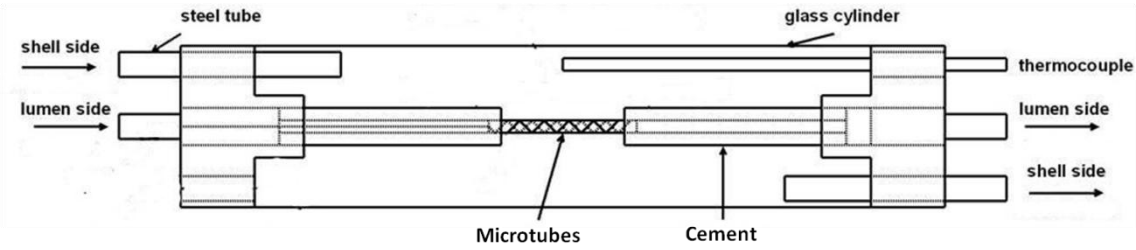

Figure 3.7 Schematic of the microtubes membrane module.

The microtubes are placed in the module using two tubes made of MACOR (Precision Ceramics, UK), these tubes have one end open and the other end closed with holes drilled to fit the microtubes. The microtubes are sealed to the MACOR tube with a glass ceramic sealant (Fortafix, UK) and also coated with the same ceramic sealant throughout the length, leaving only 5 cm (isothermal zone of the furnace) uncoated to ensure that only this area of the membranes is active. A silicone rubber, which can withstand temperatures *ca* 240°C is attached to the open side of the MACOR tube and connected to the lumen-side gas inlet/outlet. Images of the membrane module before sealed are presented in *Appendix 3-C*. Silicone sealant (RS® Silicone rubber compound) was used for the end-caps, thermocouple sleeve and gas inlet/outlet sealing. Before sealing the end-caps and the quartz together the structure (microtubes + MACOR + end-caps) is checked for leaks using a flow meter (Varian® analytical instruments) and a leak detector. The membrane module is also leak tested after sealed.

3.4.3.2 New membrane module design

In preliminary studies described in *Chapter 4* it was found that the "cold" zones were unsuccessfully blanked off using commercial water based glass-ceramic sealant. Although this material could withstand high temperatures, it did not allow the microtubes to bend (necessary when exposed to high temperatures due to the membranes' thermal expansion) causing mechanical stress leading to fracture. In addition, post operation inspection by Thursfield and Metcalfe [153] indicated that the sealant tends to become porous, raising doubts as to its suitability for this application.

In order to overcome this issue a new membrane module was designed. To avoid fracture the microtubes were not blanked off with the glass-ceramic sealant and a silicone sealant rated to 300°C (ACC Silicoset 158; composition; 1-5% diacetoxy-di-tertbutoxy silane and 1-5% methyl triacetoxy silane) was used to seal the membranes with the MACOR tube; therefore the microtubes were allowed to bend when exposed to

high temperatures. A photo image of a typical microtube membrane module showing the silicone sealant (in black) is presented in Figure 3.8.

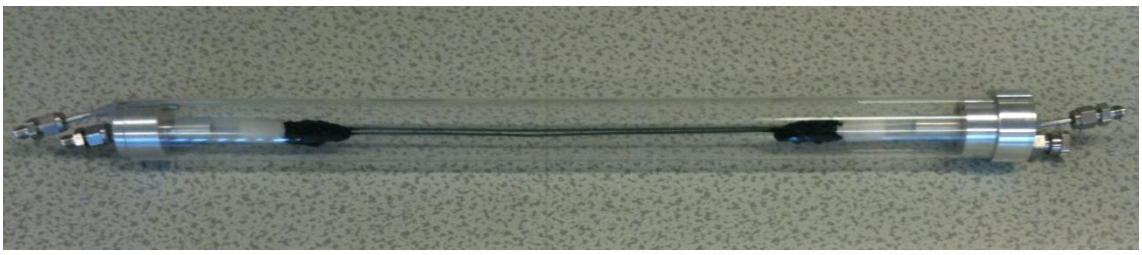

Figure 3.8 New microtube membrane module design; using silicone sealant (in black).

The experimental setup ensures the sealing points are situated in the "cold" zone outside of the furnace but creates the problem of different oxygen fluxes along the length of the membranes due to the temperature profile inside the reactor. Therefore the active permeation area of the system is not fixed, as increasing the operating temperature the active length of the microtube would also increase. However, the effective membrane area S_A of the module can be approximated by the log mean permeation area:

$$S_A = \frac{2\pi(r_o - r_i)}{\ln(r_o / r_i)} nl \qquad (3.1)$$

Where *ro* and *ri* are the outer and inner radius, respectively, of the microtubes, *n* is the number of microtubes used and *l* is the effective heating length of the membranes.

The LSCF6428 and LSF731 membrane modules were constructed and each comprised of four microtubes. The BSCF5582 membrane module was constructed with only one microtube. Approximated effective area for each membrane module at 900°C, using SW and LN furnaces are presented in *Chapter 4*.

3.4.4 Analysis system

During this work gas chromatography was the main technique used to analyse the products (gases) from oxygen permeation and redox experiments. This technique was selected due to the gradual speed of the reactions occurring at the membrane experiments.

The interactions of the gases with the walls of the GC column causes different elution times of the compounds, this is called retention time and the comparison of these retention times is the analytical power of GC [154]. The thermal conductivity detectors (TCDs) do not interact with the compound chemically but responds to a physical

property (thermal conductivity) of the carrier gas compared with the compound/carrier gas mixture. TCDs are also sensitive to concentration.

Helium is the most common carrier gas used in gas chromatography for its large difference of thermal conductivity for the other gases. Therefore the choice for the carrier gas has to be determined according to the nature of the experiments. In this work hydrogen was one of the main products; hence the use of helium as a carrier gas could not be employed as the thermal conductivity of hydrogen-helium mixtures at low concentrations of hydrogen is anomalous [155]. The use of helium as a carrier gas would have led to uncertainty and non linear responses. Argon was used as a carrier gas instead helium during this research.

In order to obtain material balances to demonstrate permeation through the membranes both exit gas composition of the membrane module were analysed simultaneously; two gas chromatographs (Varian 3900) equipped with a molecular sieve 5A column (GC 1) and a SHIN carbon column (GC 2), a thermal conductivity detector and argon as carrier gas, were used to analyse the outlets from the shell side (GC 1) and the lumen side (GC 2). Analysis interval time was *ca* 30 minutes. The discrete data obtained by GC were plotted as connected points for clarity

GC 1 was calibrated using a standard containing; 1% hydrogen 2% oxygen and 2% nitrogen in argon and GC 2 calibrated using a standard containing; 2% hydrogen 0.5% oxygen 2% carbon dioxide 2% nitrogen 2% carbon monoxide 2% methane 2% ethylene and 2% ethane in argon.

3.5 Oxygen permeation

Oxygen permeation through the microtubes was studied as a function of temperature and gases flow rate. The membrane module was placed inside a furnace (Vecstar Furnaces, UK) which was used to heat the membranes using a programmed temperature ramp of 0.5°C min^{-1} to the required operating temperature which was measured by an internal thermocouple. Air (BOC, UK) was supplied to the feed side of the microtubes and argon (BOC, UK) was used as the sweep gas on the permeate side (Figure 3.9). The oxygen partial pressure on both sides was varied by adjusting the total flow rate of the gases, which could be varied from 20 to 500 ml (STP) min^{-1}. All oxygen permeation results reported here refer to measurements at the permeated side. The oxygen permeation rate and also the rate of cross-membrane leak of nitrogen, J_x (mol s^{-1}), was

determined by the percentage mole fraction of the gas phase species, x, in the argon sweep side outlet, $[x]_{out}$ measured by gas chromatography using GC 1 (Varian 3900).

$$J_x = [x]_{out}\, F\, \frac{1}{V_m}\frac{1}{60} \tag{3.2}$$

Where F is the flow rate of the argon sweep gas in ml (STP) min^{-1}, V_m is the molar volume (1 mole is equivalent to 22,400 ml at STP) and the 1/60 factor converts the rate from minutes to seconds. The rate of gas supply to the membrane module was controlled by mass flow controllers (Brooks, UK) and monitored using a digital flow meter (Varian, UK). All experiments were performed at 1 atm on both sides of the membranes.

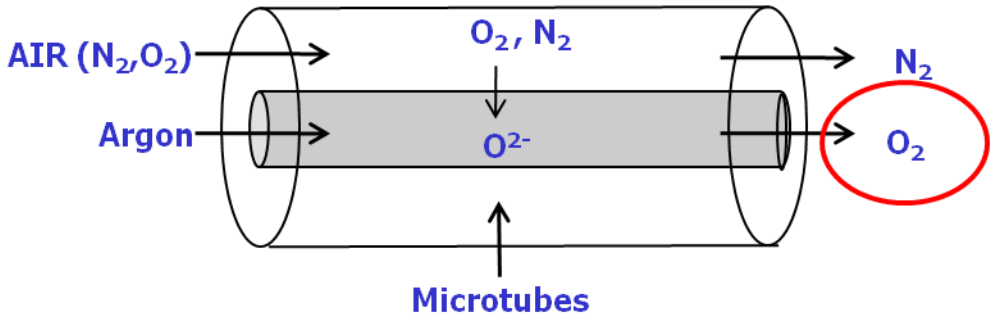

Figure 3.9 Schematic diagram of oxygen permeation experiments.

The presence of nitrogen (leaks) in the outlet of the sweep side was observed in most oxygen permeation experiments at similar levels. The oxygen permeation rate is adjusted to take this into account by subtracting the rate of oxygen leakage based on the rate of nitrogen leakage (assuming a 1:4 oxygen:nitrogen ratio).

3.6 Membrane-based steam reforming

During the membrane-based steam-reforming experiments the membrane module was placed inside a furnace (Vecstar Furnaces, UK) and the membranes were heated to the required operating temperature using a programmed temperature ramp of 0.5°C min^{-1}. Water vapour was supplied at a total flow rate of 20 ml (STP) min^{-1} to the shell side of the microtubes by a water saturator system (Grant Scientific, UK) using argon as a carrier gas. The methane (balance gas argon) was supplied at a total flow rate of 20 ml (STP) min^{-1} to the lumen side as a reducing gas. A schematic diagram of membrane-based steam reforming is given in Figure 3.10.

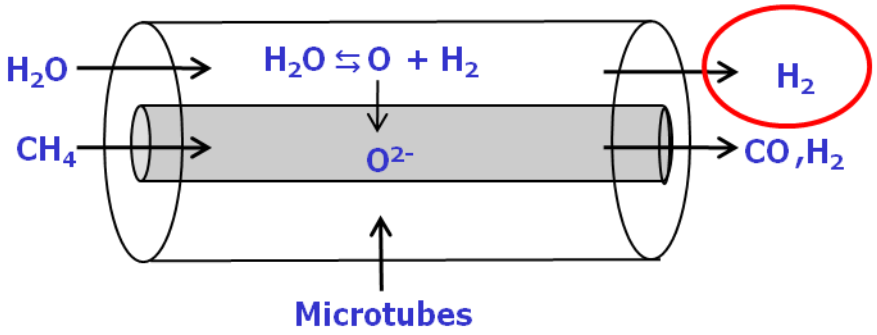

Figure 3.10 schematic diagram of membrane-based steam reforming.

The saturation of water vapour supplied could be controlled by varying the temperature of the water saturator, which in most of the experiments was maintained at 40°C so that water vapour (nominally 7.2%) was supplied to the shell side of the microtubes. The water content was monitored by a hygrometer (VAISALA HMT330) at the inlet of the membrane module. Methane concentration could be varied between 1% and 5%.

Gas chromatographs GC 1 and GC 2 (Varian 3900) were used to analyse the outlet from the shell side (for hydrogen production) and the outlet from the lumen side (for syngas production), respectively. Gas phase transport through micro-cracks in the membranes was determined by monitoring the presence of methane from the shell-side outlet.

After membrane failure the module was cooled down to room temperature under air. Membrane samples from the "hot" zone (central zone) and "cold" zone (outside the furnace) were taken from the modules for post operation analysis (SEM, EDS and XRD); the analysed samples were uncrushed.

A blank membrane-based steam-reforming experiment using dense, gas-tight alumina tubes, approximately the same dimensions of the microtubes and operated under the same conditions as described above, was performed to check if a refractory membrane could be adequately sealed under reaction conditions (900°C and methane and water vapour feeds as described above). The results of this blank experiment are presented in *Chapter 4*.

Chapter 4

4 Preliminary studies

4.1 Introduction

Prior to starting experiments evolving microtubes some important studies were carried out in order to understand how the microtubes and also the membrane module perform when exposed to the experiment environment. The effect of exposing the microtubes to high temperatures produces a few problems such as hot sealing, fracture and active surface area. These issues and their respective solution are reported in *section 4.2*. Residence time distribution studies, presented in *Section 4.3*, were performed in order to understand how the gases behave within the membrane module. Also a blank membrane-based steam reforming experiment (*Section 4.4*) was carried out using bare membranes to check if the new membrane module design could withstand the experiment conditions. In *Section 4.5* other research approaches which were attempted (*e.g.* water-gas shift reaction and catalyst deposition) are briefly discussed; although time consuming they were not fully investigated/reported here as they presented unsorted drawbacks.

4.2 Thermal expansion of the microtubes

Most studies in this area have been performed using disk membranes in an attempt to simplify the interpretation of results and also to keep the membrane at the same temperature zone during the experiments. Future application of such membranes will require high surface area and reduced wall thickness to minimise resistance to oxygen transport while maintaining mechanical strength. Microtubular membrane geometries meet this requirement and also provide a way to avoid high temperature sealing problems as long membrane lengths can facilitate "cold" sealing [122].

During the first year of this research a membrane module using a ceramic cement to blank off the "cold zones" of the microtubes leaving only 5 cm uncovered (isothermal zone) was used to perform the experiments. The microtubes used to fracture during the long process of heating up the membrane module to the required temperature of *ca*

900°C, using a programmed temperature ramp of 0.5°C min^{-1}. If the microtubes resisted the heating process they used to fracture after *ca* 40 min under reaction conditions. The fractures could be detected by checking the level of nitrogen at the permeated side outlet when running oxygen permeation and the level of methane at the hydrogen production side outlet when running membrane-based steam reforming experiments.

After many observations it was found that the microtubes often used to fracture at the interface between the uncovered microtube and the ceramic cement. Therefore it was deduced the microtubes have high thermal expansions coefficients, which may introduce internal mechanical stress across the microtubes, especially under an oxygen gradient [127]. The thermal expansion of these materials depends on the electrostatic attraction forces within the lattice, which are disturbed due to the oscillation of atomic vibrations when exposed to high temperatures [156, 157].

It was also observed that the membranes use to bend when exposed to temperatures above *ca* 750°C; however the presence of the cement prevented the microtubes to bend due to incompatibility of these materials thermal expansion leading to fracture. Hence a new membrane module was designed (described in *Chapter 3*); without the cement coating the microtubes length and using flexible silicon sealant. By this means the microtubes were able to bend when heated up to the desired temperature without fracturing as illustrated in Figure 4.1.

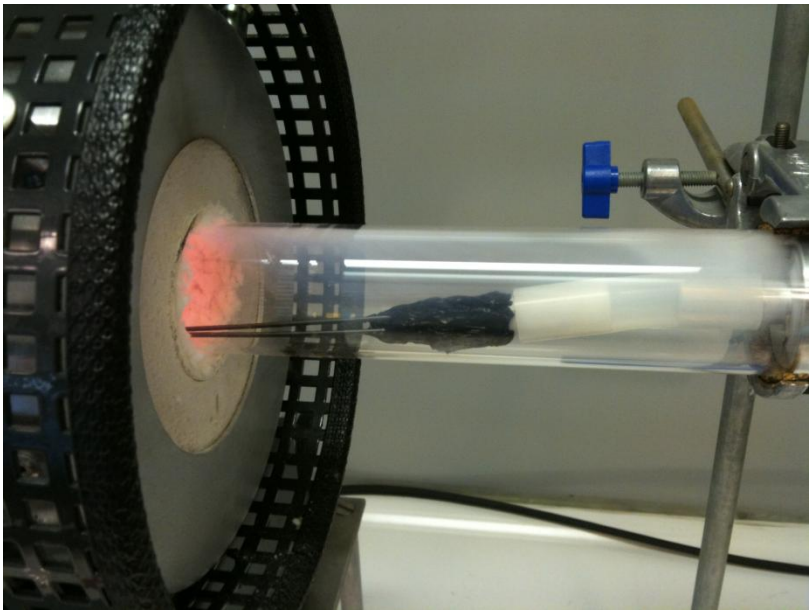

Figure 4.1 Microtubes bending when exposed to high temperatures due to high thermal expansion coefficient.

The new membrane setup addresses the problem of sealing and fractures, however produces the problem of the membrane length being exposed to different temperatures along the membrane module. This issue is reported in *section 4.2.1*.

4.2.1 Effective membrane area calculation

Reporting the operating temperature in studies employing cold-sealed long tubular microtubular membranes presents the problem of determining the temperature at which oxygen permeation is occurring. It is often assumed that the membrane operating temperature is the same as the furnace set-point temperature. However the axial temperature profile along the membrane complicates matters as the true geometric active membrane area is difficult to calculate. As presented in *Chapter 3* two custom-made furnaces were used in this work; SW furnace (isothermal zone of 3 cm) and LN furnace (isothermal zone of 5 cm). Therefore each membrane module had a different effective area *(S_A)* of the membranes calculated by Equation (3.1). The results are presented in Table 4.1.

Table 4.1 Approximated active area (S_A) of each membrane module.

Furnace	**S_A LSCF6428 (cm^2)**	**S_A LSF731 (cm^2)**	**S_A BSCF5582 (cm^2)**
SW	4.6	4.2	2.9
LN	7.7	7.1	4.8

There is some significant uncertainty in calculating the effective area in these membrane module systems. Therefore, it is difficult to report area-specific fluxes, and, instead in this work, flux is related to nominal inlet molar concentrations or transport rates. When comparing this work with other research the permeation rate is divided by the geometric effective area (S_A) of the membrane module to obtain the flux.

4.3 Residence time distribution

Working with membrane modules raises an important and poorly appreciated point for membrane studies: t o determine how gases behave within the membrane reactor. Some molecules spend longer than others to come out of the reactor. This time spent in the reactor is called the residence time and the distribution of the various atoms coming out the reactor with respect to time is called the residence time distribution [158]. This

information is important in order to determine some parameters such as conversion and yield. In this work is mainly important to know how long the flowing fluid stays in the membrane module.

The residence time distribution can be determined directly by stimulus-response experiments. Basically these experiments consist of injecting an inert gas, called the tracer, into a reactor and measuring its concentration at the outlet as function of time. In this work argon was used as a tracer to determine the residence time of the membrane module (new design with four LSCF6428 microtubes). Both, lumen and shell sides were analysed with the membrane module operating at the temperature of 900°C. The carrier flow of nitrogen was supplied at a total flow rate of 20 ml (STP) min^{-1} till the QMS could detect only the nitrogen signal, then the tracer (argon) was introduced, also at a total flow rate of 20 ml (STP) min^{-1}, by turning the argon sample valve on and turning the nitrogen supply off. The necessary time for only argon leave the reactor was then recorded. The elution profiles for the lumen-side and the shell-side are presented in Figure 4.2 and Figure 4.3, respectively.

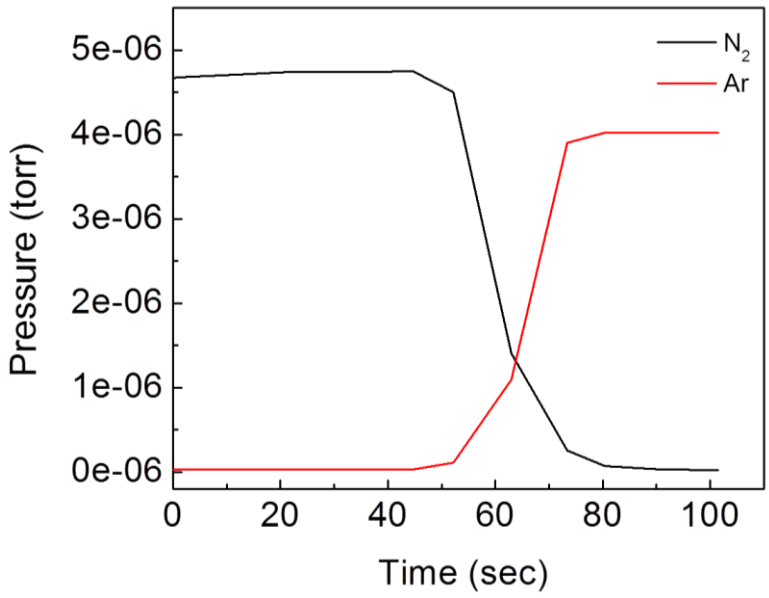

Figure 4.2 Lumen-side stimulus-response residence time distribution profile at 900°C, using nitrogen (20 ml (STP) min^{-1}) as a carrier gas and argon (20 ml (STP) min^{-1}) as a tracer.

As can be observed in Figure 4.2 at the lumen-side outlet, when argon is introduced at *ca* 50 sec there is a fast and intense response signal and after *ca* 20 sec only argon was detected by the QMS. Therefore it can be assumed that the lumen-side performs in a plug flow regime when compared to the shell-side (Figure 4.3). This is characterised by the fluid travelling in the axial direction of the reactor with no element of fluid

overtaking or mixing. In this case the residence time in the lumen-side of the membranes is the same for all elements of fluid.

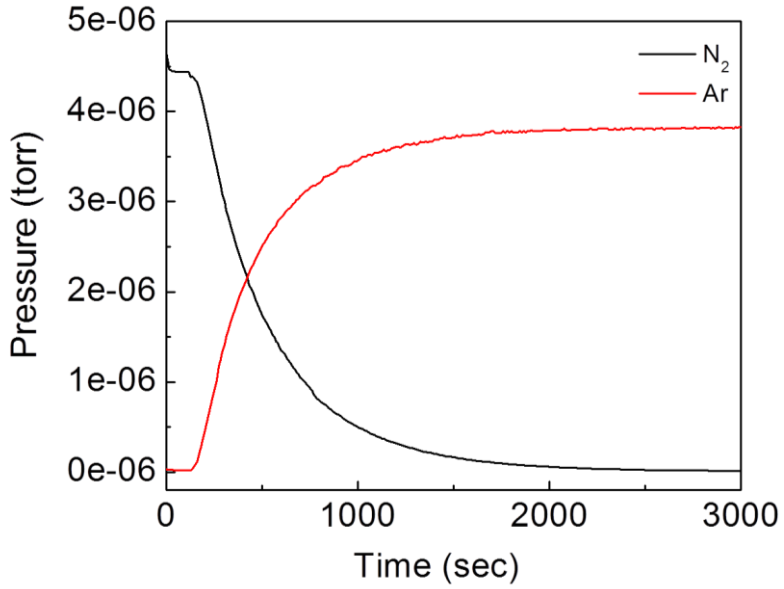

Figure 4.3 Shell-side stimulus-response residence time distribution profile at 900°C, using nitrogen (20 ml (STP) min^{-1}) as a carrier gas and argon (20 ml (STP) min^{-1}) as a tracer.

As shown in Figure 4.3 at the shell-side outlet, when argon is introduced at *ca* 120 sec there is a slow response and a broad signal of argon can be observed. The signal of argon becomes constant after *ca* 30 min. Therefore it can be assumed that the shell side of the membranes performs as a well mixed reactor. This regime is characterised by the fact that the gases introduced into a reactor are left to react for a period, and then the final mixture exits the reactor. The composition of the mixture varies with time however in certain period the composition throughout the shell-side is consistent.

The theoretical mean residence time (t_R) can also be estimated by Equation (4.1), where $V$is the reactor volume and Q is the flow rate.

$$t_R = \frac{V}{Q} \qquad (4.1)$$

The lumen side consists of four LSCF6428 microtubes with total length *ca* 30 cm and internal diameter of *ca* 1.0 mm. A calculation of volume of the four microtubes (assuming the membranes are perfect cylinders) gives a volume of *ca* 0.94 ml, which divided by the total flow rate (20 ml min^{-1}) gives a t_R of *ca* 3 seconds. The quartz tube of the reactor has 40 cm in length with an internal diameter of 3.2 cm; assuming no dead volume the volume of the shell side is *ca* 321 ml, which divided by the total flow rate (20 ml min^{-1}) gives a t_R of *ca* 16 minutes. From the calculations presented, it can be

assumed that the lumen-side performs in a plug flow regime when compared to the shell-side, which can be described as a well mixed reactor.

4.4 Blank membrane-based steam reforming test

The purpose of this study was to check if using the new membrane module design; a refractory membrane could be adequately sealed under the membrane-based steam reforming reaction conditions at 900°C. Four gas-tight alumina tubes, approximately the same dimensions of the LSCF6428 microtubes were used to simulate the microtubes. The lumen side was supplied with methane (5%) at 20 ml min^{-1} and the shell side with water vapour (7.2%) at 20 ml min^{-1}. GC1 recorded the products from the shell side outlet.

As can be seen in Figure 4.4 the presence of a background leak of oxygen (0.104% in outlet) and nitrogen (0.344% in outlet) was observed on the H_2O side. However, no methane was observed in the H_2O side outlet indicating that the alumina membranes and their sealing was gas tight. The air leak may be due to membrane module sealing or from the connections of the water vapour feed apparatus. Also, a trace amount of hydrogen (0.002%, at the limit of detection) was observed at the outlet of the H_2O side indicating a very low water-splitting activity. Any significant hydrogen production can therefore be attributed to the presence of the perovskite microtubular membranes.

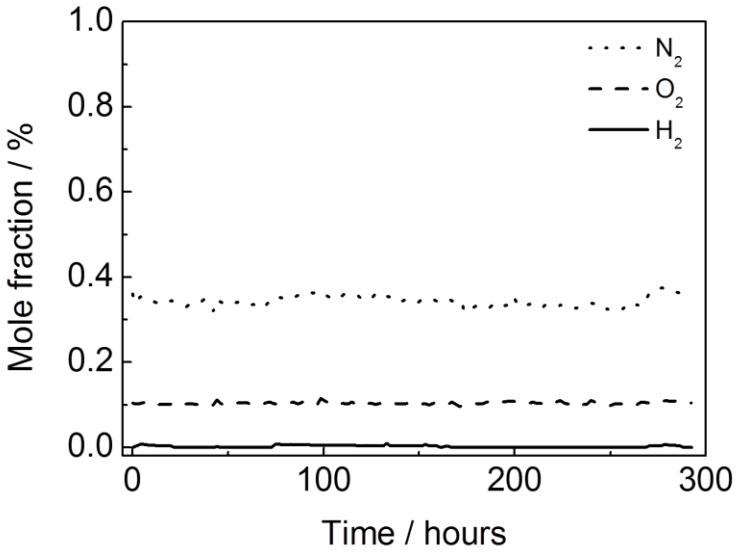

Figure 4.4 Blank membrane-based reforming at 900°C using alumina tubes to simulate the microtubes. Lumen side was supplied with methane (5%) at 20 ml min^{-1} and the shell side with water vapour (7.2%) at 20 ml min^{-1}.

4.5 Attempted studies

Although most of the work presented in this thesis refers to methods which presented satisfactory results for hydrogen production via membrane-based steam reforming, many other studies were attempted which however presented drawbacks. These attempts were based in previous work reported in the literature and also in novel ideas. Nevertheless they have not presented satisfactory operation conditions and further investigation/conclusions were not possible within the scheduled time. In this section they are briefly presented.

These drawbacks were expected as membrane-based hydrogen production from water splitting is an emerging area with many developments still being required. The state of art does not allow yet a fully efficient use of this technology in commercial applications as there are some limiting factors (*e.g* membrane stability).

Concerning publications in this area, research could benefit if some aspects were clearly reported, such as experimental protocol, duration of operation, membrane history, membrane stability, material balance and specially membrane failure. These are often neglected or incomplete described, hence the reproducibility of these studies are difficult or even impossible.

4.5.1 Tubular membrane reactors

During this research project more than 150 tubular membrane reactors were assembled, each module requiring an average period of three days to be successfully assembled. This time lapse is necessary as leaking tests can only be performed after silicone sealant cure. From whole reactors produced, a failure rate of approximately 80% was observed since satisfactory operation conditions were only achieved in *ca* 20%. The main issues observed were the already mentioned instabilities, both thermal and chemical, of the membranes under operating conditions.

Inhomogeneity of the membranes appears to affect performance of a single membrane reactor (consisting of four microtubes) as membranes from the same "bunch" presented different behaviour when used at the same experiential conditions, *e.g*. during the process of heating up, some membranes usually bent (eventually fracturing) to a greater extent than other membranes in the same reactor. This non-homogeneity may occur due to impossibility of perfect reproducibility of the membranes.

The sintering process of the microtubes can also lead to non-homogeneity in a single membrane. The temperature profile of the horizontal furnace used to sinter the microtubes (LSCF and LSF) applied in this research is presented in Figure 4.5. Most of the microtubes were sintered at the temperature of 1200°C; therefore temperature profile at the interior of the furnace at this temperature was recorded. The thermocouple was originally placed at the centre of the furnace and then moved out in 2.0 cm steps to the end of the furnace. It was assumed that the furnace had symmetrical temperature profile.

An isothermal zone length of 20 cm at the centre of the furnace was measured; however the temperature dropped when the thermocouple was moved out the furnace. This drop on the temperature can generate some non-uniform sintering properties, leading to different properties along the microtube length.

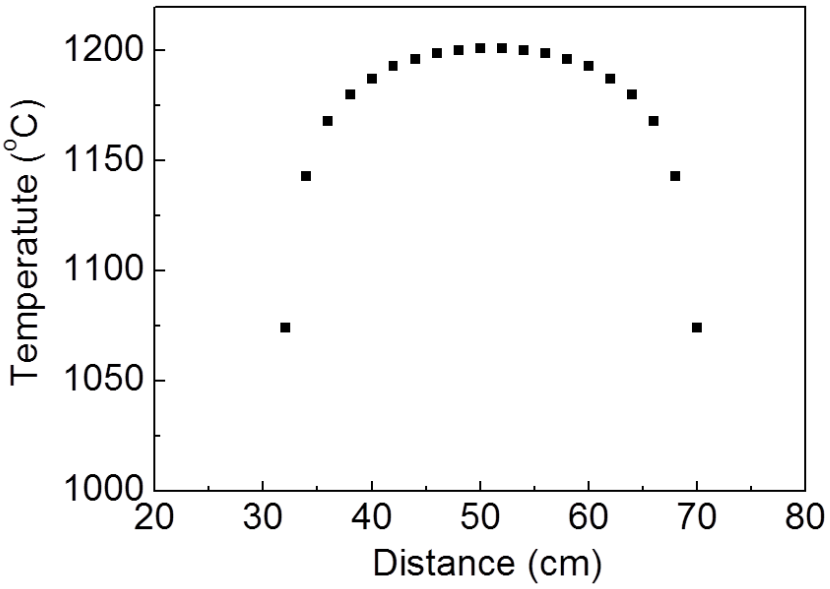

Figure 4.5 Microtubes sintering furnace; internal temperature profile of at 1200°C.

The non-uniformity of ion-exchange membranes has great influence on many physical and chemical properties of ion-exchange systems and their operational characteristics. As an example, Figure 4.6 presents a membrane module which was cooled down to room temperature after two membranes presented mechanical failure, however it was observed that the other two membranes in the module remained in good conditions. This behaviour shows non-homogeneity of microtubes from the same “bunch” when exposed to the same operation conditions.

Figure 4.6 Mechanical failure of two membranes in the reactor; the other two membranes remained in good conditions.

4.5.2 Disk membrane reactors

Disk membranes were also studied in this project; powder material of LSCF6428, LSF731 and BSCF5582 were pressed into disks 1mm thick (Figure 4.7). Calcined powders were ground using a mortar and pestle followed by green disk formation (15mm diameter) using a 3 tons force hydraulic press. The disks were finally sintered at 1300°C for 12h.

This simpler membrane geometry would have facilitated the fast investigation of certain processes (*e.g.* kinetics) as the reactor assembling process is easier than tubular reactors. The main issue encountered with these membrane reactors was the incapability to perform a gas-tight seal between the membrane and the alumina tube (support). Hot sealant materials are discussed in the following section.

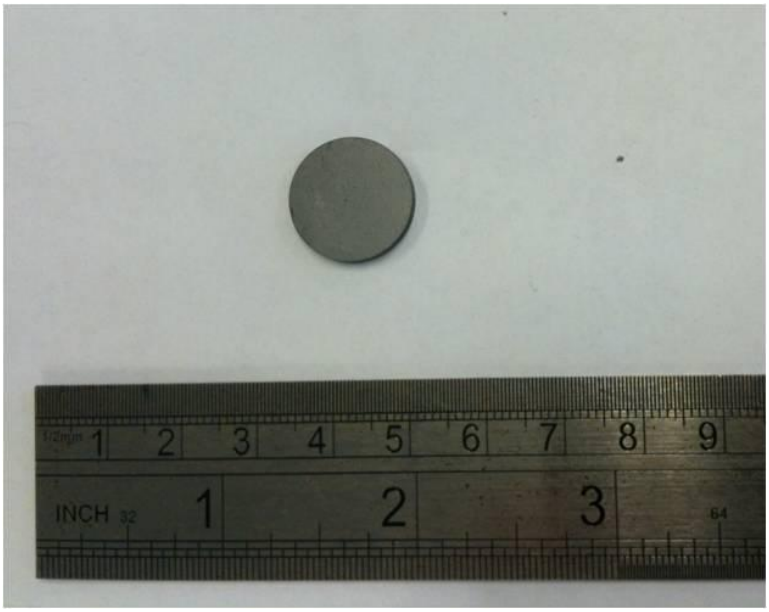

Figure 4.7 Disk membranes (1mm thick) produced by hydraulic press.

4.5.3 Sealant materials

Other drawbacks encountered during this project were the high temperature sealant materials to membrane reactors as the sealant material has to withstand the experimental conditions and should present compatibility with the membrane material. Hot sealant materials and "cold" sealant materials were studied during this research and discussed in the following sections.

4.5.3.1 Hot sealant

Hot sealant material must present good compatibility with the membrane. It is of major importance that both (sealant and membrane) present similar thermal expansions to avoid fractures during the operating mode. Moreover this sealant material has to present good chemical stability to perform over long period. Some hot sealant material tried during this project presented promising results, but most of them presented undesirable properties and did not perform as expected, leading to leaks or mechanical failure of the microtubes (incompatibility).

An alkali-free glass sealant material (provided by Henny Bouwmeester's group) cut into rings with an outer diameter of 12 mm and inner diameter of 8 mm was tested to seal disk membranes. This sealant material had to be operated at the temperature range of 750-900°C; in a first attempt the seal presented desired properties however after *ca* 20 min of oxygen permeation operation the seal failed and leakage could be detected. Other

attempts presented success in sealing the disk membranes with this glass sealant material; however no oxygen permeation was detected during these experiments. Post operation analysis has shown the glass melted and blocked the permeation area of the membranes as observed in Figure 4.8. Semi-quantitative EDS analysis (Table 4.2) of the blocked permeation area (point 0) presented elements from the glass sealant material.

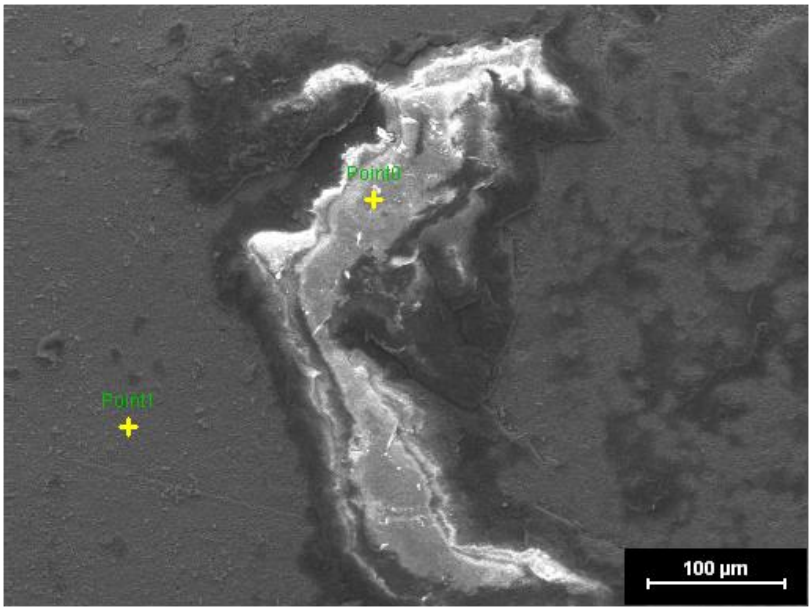

Figure 4.8 Glass sealant material blocking permeation area of a disk membrane.

Table 4.2 Semi-quantitative EDS analysis of disk membrane blocked by glass sealant material.

		Approximate atom (%)			
Si	**Al**	**P**	**Mg**	**Ca**	**C**
24.0	12.0	1.5	2.8	2.0	57.7

A ceramic sealant material (Aremco Ceramabond) was also tested for disk membranes and microtubular membranes. This sealant material presented good compatibility only with BSCF5582 tubular membranes. A short BSCF5582 membrane of *ca* 5 cm was sealed at the isothermal zone of the SW furnace and operated over 90 hours under oxygen permeation conditions.

The oxygen permeation rate was measured on the lumen-side outlet as a function of the air flow rate on the shell-side when the sweep gas (argon) flow rate was kept constant at 20 ml (STP) min^{-1} on the lumen-side. Measurements were made with the SW furnace at 900°C. Oxygen permeation measurements are presented in Figure 4.9. As expected, the oxygen permeation flux increases with increasing air flow rate, as the oxygen partial

pressure on the shell-side is increased, consequently increasing the driving force for oxygen permeation. Oxygen permeation rate increased from *ca* 1.2µmol O_2 s^{-1} to *ca* 1.6µmol O_2 s^{-1} when the air flow rate was raised from 20 to 100 ml(STP)min^{-1}. The highest permeation achieved in these experiments was *ca* 1.7µmol O_2 s^{-1} when the air flow rate was 300 ml(STP)min^{-1}. After 90 hours of operation a leakage was detected and the experiment stopped.

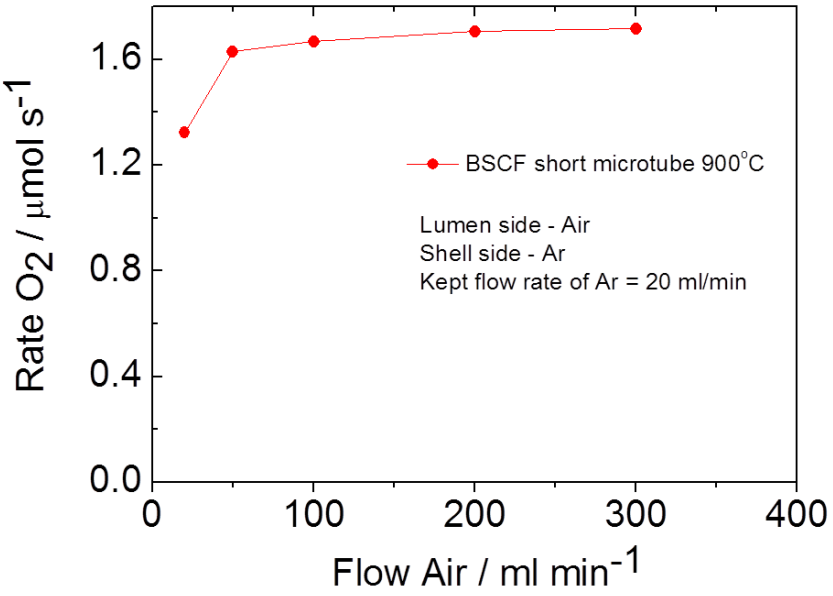

Figure 4.9 Oxygen permeation with BSCF short microtube on the lumen-side outlet, varying air supplied on the shell side with argon as sweep gas on the lumen side at 20 ml min-1.

4.5.3.2 "Cold" sealant

The new membrane module design ensures the sealing points are situated in the "cold" zone outside of the furnace; silicone sealant rated to 300°C was successfully applied guarantying gas-tightness during all the experiment. However silicon contamination of the membrane surfaces was often detected at operation conditions. It is conceivable that silicon leached out of the sealant and contaminated the membranes. In some extreme cases a "white powder" was observed on the top of the membranes and also at the quartz shell (Figure 4.10). Semi-quantitative EDS analysis (Table 4.3) confirmed the presence of silicon in this powder and also at the shell-side surface of the contaminated membranes. Membranes which presented silicon contamination showed low oxygen permeation rates and therefore did not perform as expected.

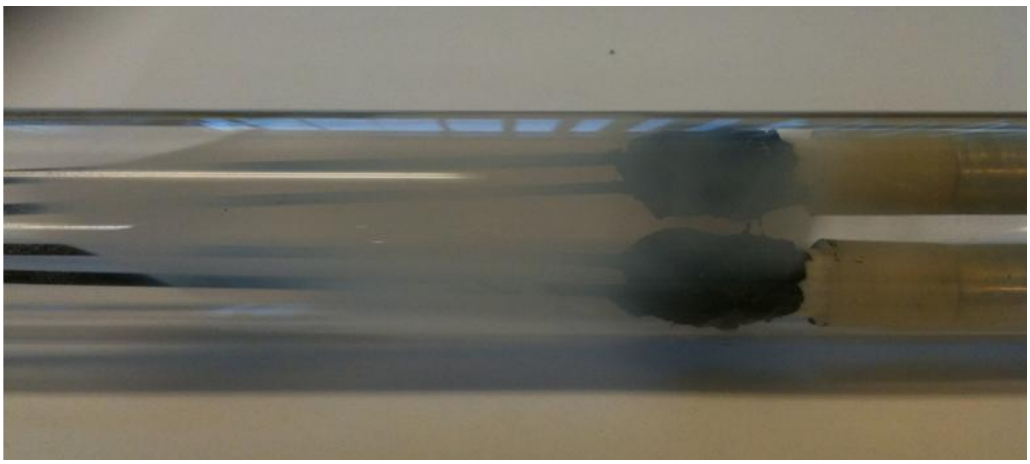

Figure 4.10 “White powder” observed at the quartz shell.

Table 4.3 Semi-quantitative EDS analysis of LSCF membranes with no oxygen permeation due to silicon contamination and "white powder" encountered on the top of the membranes.

Material	**Approximate atom (%)**					
	La	**Sr**	**Co**	**Fe**	**Si**	**O**
White powder	-	-	-	-	36.0	64.0
LSCF no permeation	-	7.7	2.6	3.3	86.4	-

From the furnaces internal temperature profile (Figure 3.6) it was observed that the sealant material was exposed to temperatures *ca* 100°C during operation. In order to avoid silicon contamination the membrane/sealant material was exposed to temperatures *ca* 100°C before the assembling of the membrane reactor. This has shown to reduce this effect as the white powder was not observed after this procedure.

4.5.4 Catalyst materials

Catalyst material deposition in order to improve surface exchange kinetics was also studied. Thin palladium films were deposited by sputtering (by David Book’s group at Birmingham University) in LSCF6428 membranes. Two disk membranes and one microtubular were coated according to the time of palladium deposition:

- Disk membrane (D1) coated for a period of 5 seconds.
- Disk membrane (D2) coated for a period of 50 seconds.
- Microtubular membrane (T1) coated for a period of 5 seconds.

A preliminary investigation of the deposition of palladium on the membranes was carried out. Semi-quantitative EDS analysis (Table 4.4) indicated the presence of small amounts of palladium (*ca* 3 atom %) in the disk (D1) and microtubular (T1) membranes coated for 5 sec. The disk membrane coated for 50 sec (D2) presented a higher amount of palladium (*ca* 10 atom %). Although the thickness of the layers was not measured it is expected that thickness increases linearly with time in sputtering processes [159].

Table 4.4 EDS analyses of LSCF6428 membranes coated with palladium catalyst.

Material	**Approximate atom (%)**				
	La	**Sr**	**Co**	**Fe**	**Pd**
LSCF6428 (D1)	30.0	13.1	9.2	43.9	3.8
LSCF6428 (D2)	27.9	8.6	11.2	41.6	10.7
LSCF6428 (T1)	31.7	11.0	10.2	43.8	3.3

Figure 4.11 presents SEM images of the two coated LSCF6428 disks, coupled with EDS maps which show the palladium distribution. It is clear that the coating (both 5 and 50 sec) has not covered the surfaces as the grains are clearly observed. Palladium was found to be eventually distributed on the both surface of both disks; however, as expected, with a higher concentration in D2. The deposition of palladium in the microtubular membrane (T1) showed similar SEM and EDS mapping results to D1.

Similar studies using palladium surface modified LSCF microtubes showed that palladium coating procedure was beneficial in improving oxygen fluxes [160]. The authors stated that the palladium coating onto the surface of the LSCF microtubes overcame the surface exchange reaction kinetics and enhanced the oxygen flux by up to 350%, in comparison to unmodified LSCF hollow fibres. Nevertheless some of the membranes coated with palladium did not present any effect on the oxygen flux due to the non-homogeneous distribution and aggregation of palladium nanoparticles, hence reducing the spill-over effect of the catalyst.

However the palladium deposition presented promising results, its application in disk membrane reactors was not possible for reasons mentioned before (hot sealant issues). The microtubular membrane with palladium deposition was assembled in a membrane reactor and placed inside the SW furnace for further investigation. The membrane, however, fractured during the heating up process using a programmed temperature ramp of 0.5°C min^{-1}. Cleary stability issues (compatibility, palladium aggregation, thermal

expansion, etc) caused the mechanical failure and further experiments with this catalyst material are necessary to understand the failure process.

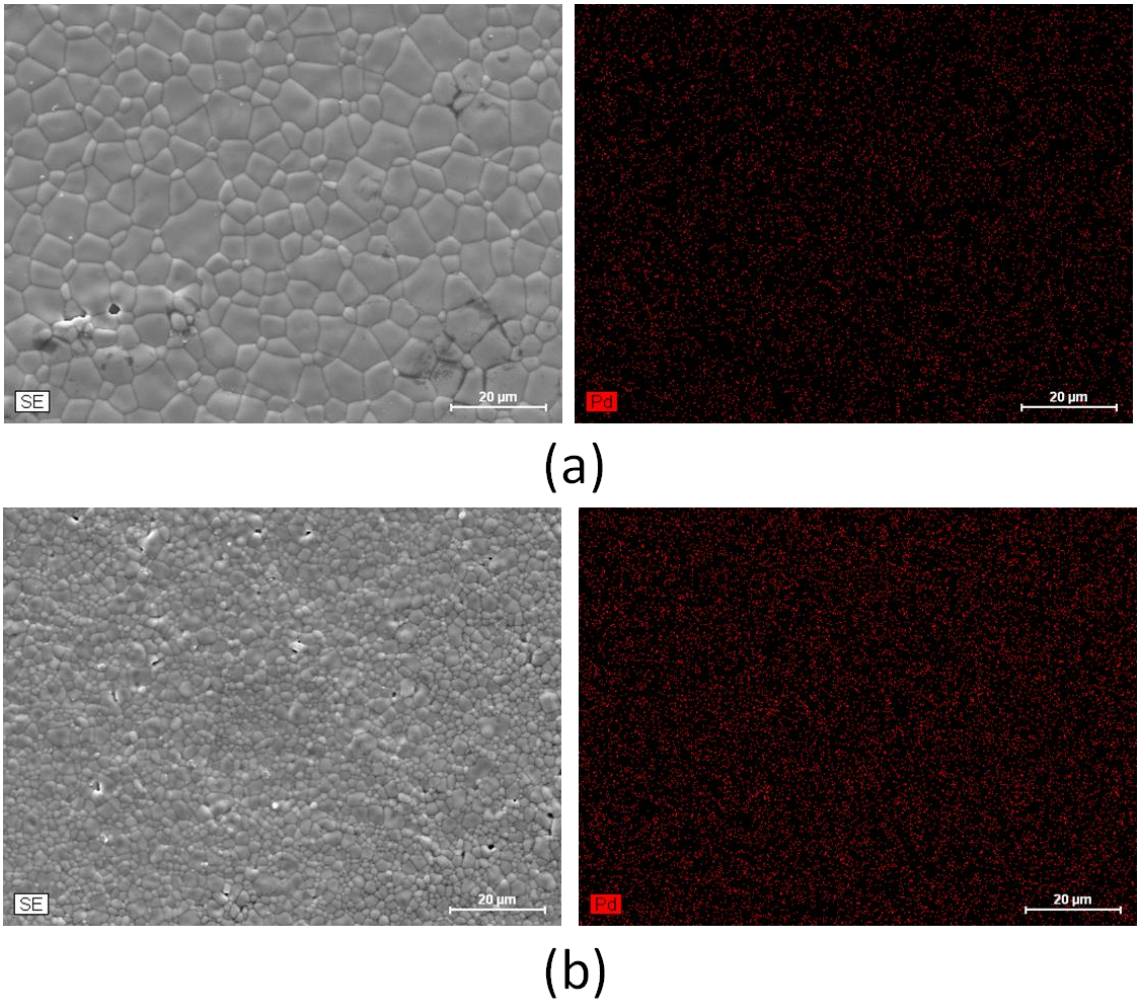

Figure 4.11 SEM images and EDS maps of the surface of LSCF6428 disk membranes after (a) 5 seconds and (b) 50 seconds of palladium deposition.

4.5.5 Membrane-based water-gas shift

Membrane-water gas shift was also briefly investigated with LSCF6428 microtubes. During these experiments the membrane module (consisting of four microtubes) was placed inside the LN furnace and heated up (0.5°C min^{-1}) to 900°C. Water vapour (nominally 7.2%) was supplied at a total flow rate of 20 ml (STP) min^{-1} to the lumen side of the microtubes using argon as a carrier gas. Carbon monoxide (10% balanced in nitrogen) was supplied at a total flow rate of 20 ml (STP) min^{-1} to the shell side as a reducing gas. A schematic diagram of membrane-based steam reforming is given in Figure 4.12.

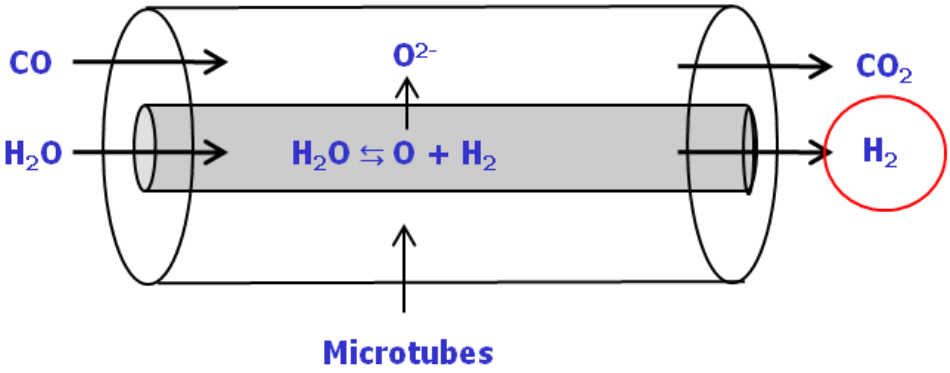

Figure 4.12 Schematic diagram of water-gas shift experiments.

The membranes used in this first attempt (carbon monoxide concentration of 10%) presented mechanical failure after *ca* 30 min of operation and no data was collected. In an attempted to operate the membranes under a less aggressive environment the carbon monoxide concentration was reduced (0.5%). A new membrane reactor was then tested (Figure 4.13); the membranes presented trans-membrane leakage of oxygen, nitrogen and carbon monoxide (not presented) probably due to gas phase transport through micro-cracks in the membranes. Hydrogen production was detected at very low levels (*ca* 0.07%). The membranes presented mechanical failure after 300 minutes of operation.

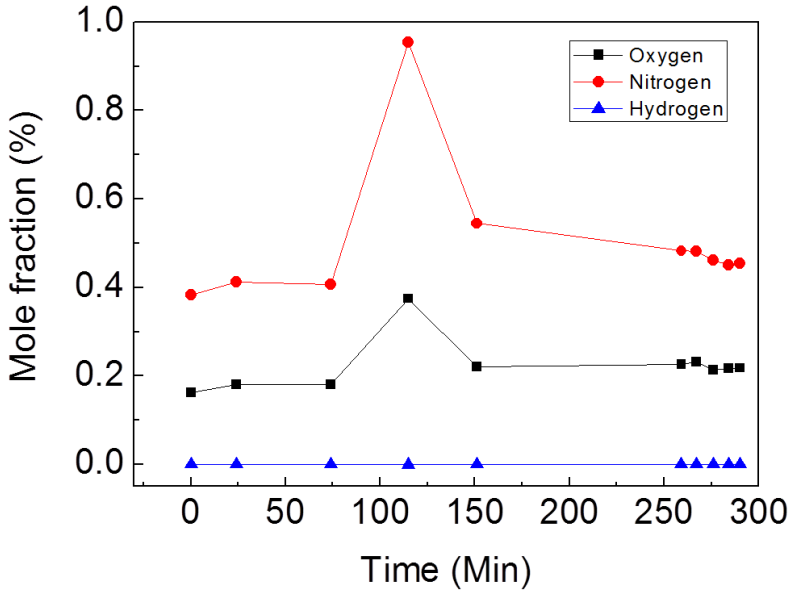

Figure 4.13 Membrane-based water-gas shift with water vapour supplied on the lumen side at 20 ml min^{-1} and carbon monoxide (0.5%) on the shell side at 20 ml min^{-1}using LN furnace (900°C).

Semi-quantitative EDS analysis (Table 4.5) with the membranes used in the first experiment (10% of carbon monoxide) indicated the presence of carbon on the shell-side (not observed in fresh membranes); carbon deposition may have caused corrosion and further mechanical failure of the membranes. Similar behaviour has been reported with perovskite membranes for hydrocarbons conversions [100, 101]. Other characterisation techniques are required to fully understand the failure mechanism in these membranes.

Table 4.5 Post operation EDS data of LSCF6428 microtubes after membrane-based water-gas shift.

Material	**Approximate atom (%)**					
	La	**Sr**	**Co**	**Fe**	**C**	**S**
LSCF6428 (Shell side)	12.3	10.5	3.0	15.7	51.8	6.7
LSCF6428 (Lumenside)	23.2	20.5	13.0	32.8	-	10.5

4.5.6 Autothermal membrane-based steam reforming studies

It is important to state that this experiment was only a preliminary study for autothermal membrane-based steam reforming operation; material balance or post-operation analysis were not the purpose of this experiment. Complete analysis of hydrogen production from membrane-based steam reforming is presented in *Chapter 6*.

Membrane-based steam reforming is an endothermic process; in order to achieve autothermal operation some of the reducing gas can be used to be combusted and provide the required heat (Figure 4.14). In a first attempt to achieve this autothermal operation a membrane module (consisting of four microtubes) was placed inside the LN furnace and the membranes were heated to 940°C. Water vapour (nominally 7.2%) was supplied at a total flow rate of 20 ml (STP) min^{-1} to the shell side of the microtubes using argon as a carrier gas. Methane (5% balanced in argon) was supplied at a total flow rate of 20 ml (STP) min^{-1} to the lumen side as a reducing gas.

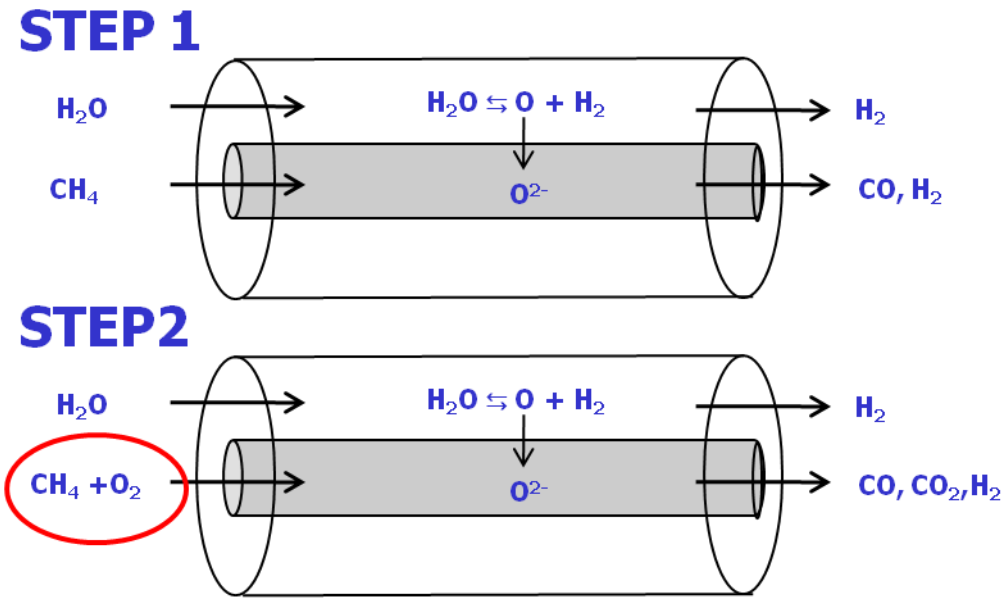

Figure 4.14 Schematic representation of autothermal membrane-based process for hydrogen production.

As can be observed in Figure 4.15(a) at the shell-side outlet the level of hydrogen increased and after *ca* 40 hours reached a steady state mole fraction of *ca* 0.7%. After 60 hours the temperature was lowered to 900°C followed by a decrease of hydrogen production to *ca* 0.4%. After *ca* 85 hours diluted oxygen (1%) was supplied with methane in order to combust some methane and produce heat to the system. However methane rapidly consumed the oxygen supplied, indicating complete combustion of methane and carbon dioxide production on the lumen side (Figure 4.15 (b)). Therefore the hydrogen production on the shell side rapidly decreased as the methane stopped to remove oxygen across the membrane. This demonstrates the need for an oxygen vacancy concentration gradient across the membrane in order to observe water splitting. The oxygen supply was interrupted and only methane supplied after *ca* 200 hours of experiment, the oxygen vacancy gradient was re-established and hydrogen on the shell-side outlet was observed at approximately the same level as before interruption. The addition of oxygen may have generated heat to the system, however interrupted the hydrogen production. A novel approach for autothermal membrane-based steam reforming is suggested in *Section 7.2* (suggested future work).

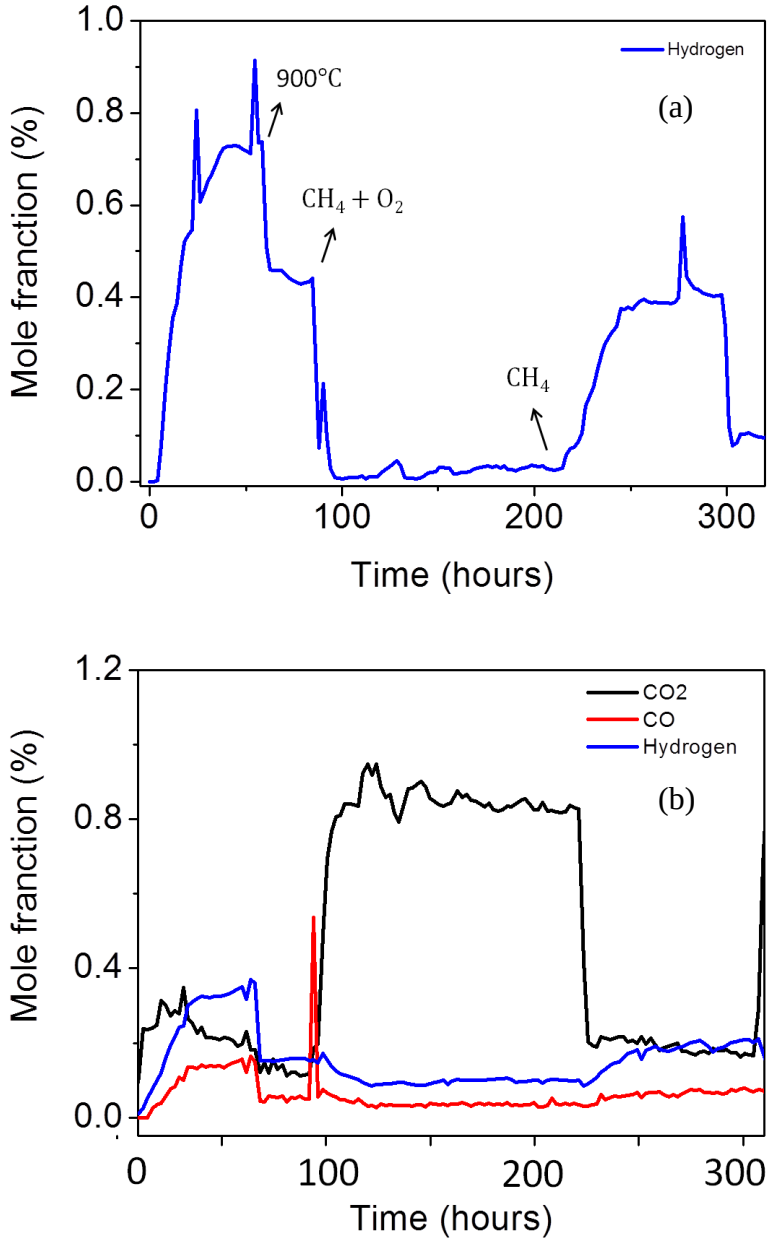

Figure 4.15 Outlet composition from autothermal membrane-based steam reforming studies using the LN furnace (a) on the shell side and (b) on the lumen side.

Chapter 5

5 Materials Selection

5.1 Introduction

The main objective of the work presented in this chapter is to investigate the feasibility of three perovskite materials (later presented) to produce hydrogen from water splitting. Temperature programmed and membrane-based experiments were carried out to evaluate the reactivity of each perovskite. Also the suitable conditions for long term membrane-based steam reforming experiment were investigated. Material balance and detailed post operation analysis are not the main goal and therefore not presented in this chapter; those are presented in *Chapter 6* when long term experiments were performed.

Materials that exhibit oxygen transport and the capability to undergo surface oxidation and reduction can be operated in membrane processes and in the dynamic mode of temperature programmed processes. In this work the oxide would be reduced in methane in the first step followed by reoxidation in water; during the second step the feasibility of producing hydrogen by water splitting will be investigated. The membrane system also works in a similar process, which one side of the membrane is exposed to methane and the other to water. In this way the temperature programmed redox processes are separated temporally rather than spatially across a membrane (Figure 5.1).

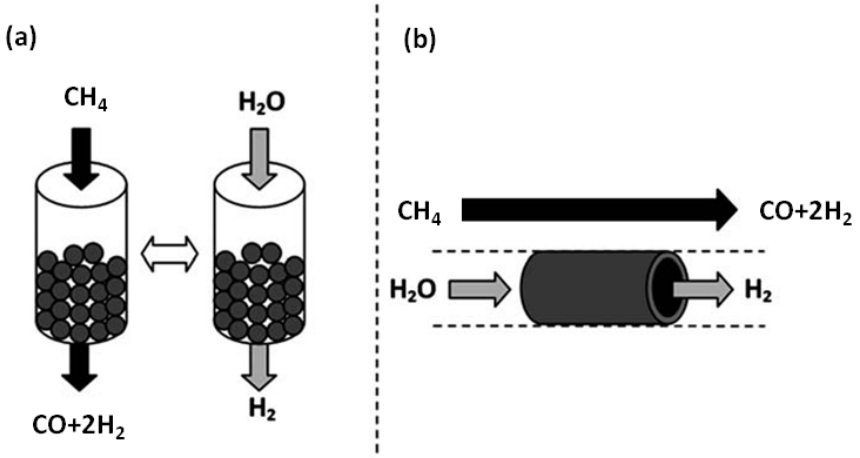

Figure 5.1 Schematic representing (a) periodically temperature programmed process and (b) oxygen permeating mebrane system for hydrogen production via steam reforming [109].

For practical applications the oxygen carrier material (OCM) itself and the membranes must be able to transport oxygen through the bulk and not just surface oxidation and reduction. Operation of the material in temperature programmed processes can offer information on the oxygen storage/transport capacity of the OCM and the feasibility of producing hydrogen from water splitting under the experimented conditions.

In order to determine which OCM material, among LSCF6428, LSF731 and BSCF5582 is the most suitable for hydrogen production via methane activation and water splitting, temperature programmed experiments were performed (*Section 5.2*). Powder material and dense membrane fragments were used in the experiments, LSCF6428 and LSF731 performed better than BSCF5582, however LSCF6428 membrane fragment presented better performance among all OCM tested.

Experiments using membrane modules were also studied and presented in this chapter; oxygen permeation experiments (*Section 5.3.2*) were carried in order to evaluate the capability of the microtubes to permeate oxygen; BSCF5582 microtubes presented higher oxygen permeation rates than LSCF6428 and LSF731. However LSCF6428 demonstrated better potential for hydrogen production from water splitting (*Section 5.3.3*). The influence of oxygen partial pressure was also analysed, this focused on systematically varying the inlet methane and water concentrations during the membrane-based steam reforming experiments.

Post operation analyses (*Section 5.3.4*) revealed the presence of a strontium/sulfur layer on the LSF731 microtubes which may have affected the oxygen permeation and consequently hydrogen production.

5.2 Temperature programmed experiments

Powder material and dense membrane fragments (50 mg of material was used in each case) were evaluated in a microreactor testing system. Fifteen isothermal redox cycles were performed at 900°C using alternating flows of 5% methane and then 2.6% water, each supplied at a total inlet flow rate of 20 ml min^{-1}. Temperature programmed reduction (TPR) and oxidation (TPO) steps were performed for 30 minutes.

5.2.1 Characterisation of fresh materials

BET analysis of the fresh OCM powder materials are presented in Table 5.1. LSCF6428 presented the highest specific surface area per mass of sample so this material would be expected to present higher kinetics than the others. However this cannot be considered the main property of the material as oxygen transfer to the bulk of the material would play an important role due to the presence of oxygen vacancies in the perovskite structure.

Table 5.1 BET analysis of fresh OCM samples.

OCM	Abbreviation	BET ($m^2 g^{-1}$)
$La_{0.6}Sr_{0.4}Co_{0.2}Fe_{0.8}O_{3-\delta}$	LSCF6428	9.0
$La_{0.7}Sr_{0.3}FeO_{3-\delta}$	LSF731	6.0
$Ba_{0.5}Sr_{0.5}Co_{0.8}Fe_{0.2}O_{3-\delta}$	BSCF5582	1.2

SEM images were taken of the surfaces of the fresh microtubes fragments and are shown in Figure 5.2. BSCF5582 and LSCF6428 surfaces consists of well sintered particles with grains connected and clear boundaries. Grain size range from *ca* 2 to 7µm and *ca* 1 to 5µm is observed in BSCF5582 and LSCF6428 respectively. LSF731 shows an irregular rough surface with unclear grains and boundaries. Spot EDS analysis (Table 5.2) of the fresh microtubes fragments show the presence of sulfur and segregation of strontium on the LSF731 surface and may be the reason that the SEM did not present clear images. Further analysis of the LSF731 fresh microtubes are presented in *Section 5.3.1*.

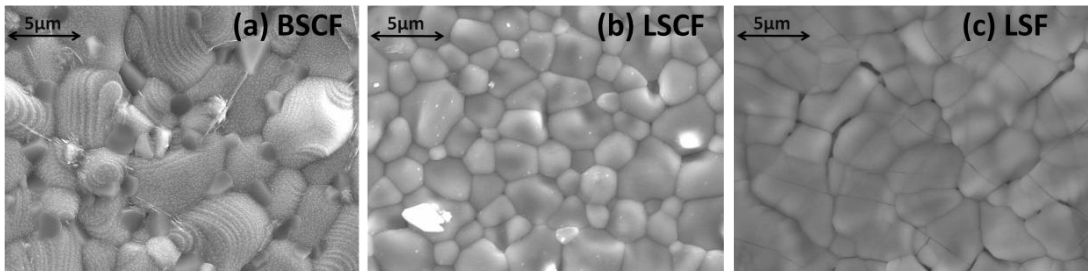

Figure 5.2 SEM Images of fresh microtubes fragments (a) BSCF5582, (b) LSCF6428 and (c) LSF731.

Spot EDS of the LSCF6482 did not show the presence of foreign elements or segregation of any constituents of the perovskite. However BSCF5582 surface shows the presence of sulfur, probably from polysulfone binder used at the microtube fabrication [7]. Studies with BSCF5582 microtubes showed that sulfur-containing compounds can react with barium and form $BaSO_4$ [161, 162], which can decrease the oxygen permeation of the membranes [163].

Table 5.2 Spot EDS analyses of fresh microtubes fragments.

Material	**Approximate atom (%)**					
	La	**Ba**	**Sr**	**Co**	**Fe**	**S**
BSCF5582	-	21.4	14.3	42.7	13.4	8.2
LSCF6428	32.5	-	8.9	10.0	48.6	-
LSF731	2.7	-	38.2	-	4.0	55.1

5.2.2 TPR/TPO cycles

Methane was used as the reducing agent during the TPR cycles and water as the oxidising agent during the TPO cycles. The overall reaction is the steam reforming of methane (Equation (5.1)).

$$CH_4 + H_2O \rightarrow CO + 3H_2 \quad (5.1)$$

During the TPR steps mainly carbon monoxide and hydrogen are produced by the following reaction (Equation (5.2)), using Kröger-Vink notation:

$$CH_4 + O_O^x \leftrightarrow CO + 2H_2 + V_O^{\bullet\bullet} + 2e^- \quad (5.2)$$

Hydrogen is produced during TPO steps by the Equation (5.3).

$$H_2O + V_O^{\bullet\bullet} + 2e^- \leftrightarrow H_2 + O_O^x \quad (5.3)$$

Temperature programmed reaction of the powder materials and membrane fragments were carried out in order to analyse and compare the oxygen capacity and reactivity for water splitting and methane activation of the OCMs during 15 cycles for 50mg of sample. The products of TPR/TPO for powder materials and membrane fragments are presented in *Appendix 5-A*. Operation of powder and membrane material in the dynamic mode of TPR/TPO can in principle offer additional kinetic information for the

membrane processes. As hydrogen production is the main focus of this research only the TPO cycles presenting hydrogen production are reported in Figure 5.3.

As can be observed in Figure 5.3a BSCF5582 powder produced initially *ca* 300µmols of hydrogen per cycle and after the 6th cycle the level of hydrogen decreased to *ca* 160µmols per cycle. LSCF6428 powder produced steady hydrogen (*ca* 400µmols per cycle) during the 15 cycles. The level of hydrogen decreased after the 6th cycle of TPO using LSF731 from *ca* 560µmols per cycle to *ca* 430µmols per cycle.

BSCF5582 membrane fragments presented low hydrogen production activity from water splitting as can be observed in Figure 5.3b, producing *ca* 5µmols per cycle during the 15 cycles. LSCF6428 produced *ca 5*µmols per cycle during the first 5 cycles then rapidly increased to 36µmols per cycle and later (9th cycle) to *ca* 45µmols per cycle, remaining steady until the 15th cycle. LSF731 also presented an induction period until the 6th cycle, producing *ca 5*µmols per cycle then increasing to *ca* 15µmols per cycle until the 15th cycle.

The results of the investigation indicated that LSCF6428 and LSF731 performed better for hydrogen production from water splitting and methane activation than BSCF5582. However the LSF731 membrane fragment did not present good activity for hydrogen production from water splitting. Post operation analysis revealed that surface contamination may have caused this effect and is discussed in *Section 5.2.3*.

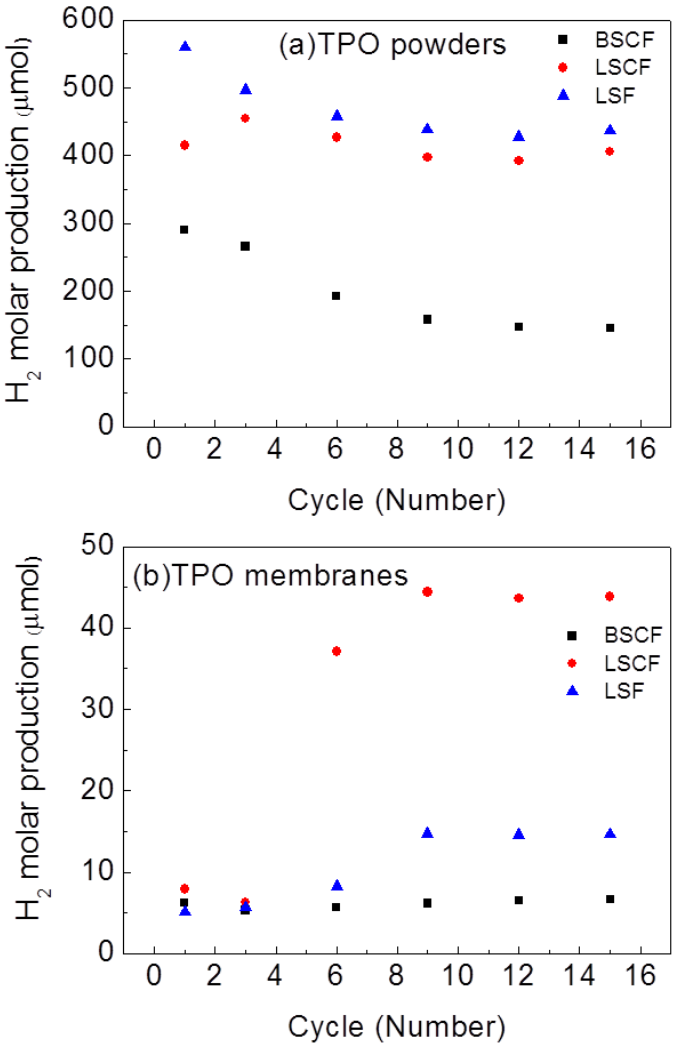

Figure 5.3 Hydrogen production during 1st and 15th TPOs at 900°C of *ca* 50mg of BSCF5582, LSCF6428, LSF731 (a) powder materials and (b) membrane fragments.

LSCF6428 samples (powder and membrane fragment) produced hydrogen during oxidation with water and also syngas during reduction in methane (*Appendix 5-A*). Although, during oxidation the LSCF6428 powder gave a significant amount of hydrogen from the first cycle, the LSCF6428 membrane fragments showed an induction period in which almost no hydrogen from water splitting was observed until the 6th redox cycle. This is consistent with a slowly changing oxidation state of the membrane material in membrane form over the first five cycles and may be related to the induction also observed in the operating membrane (*Section 6.4.1*). Similar behaviour was also observed in temperature programmed studies involving $La_{0.3}Sr_{0.7}FeO_3$ powder materials; Evdou *et al* affirmed that a certain activation process is necessary in prior to the material split water and produce hydrogen [142].

During reoxidation (TPO) steps, carbon monoxide and traces of carbon dioxide were produced (*Appendix 5-A*) for all OCM materials (powder and membrane fragments),

probably due to water oxidation of deposited carbon (Equations (5.4) and (5.5)), which could have been formed during the TPR steps. Carbon formation during reduction will result in carbon being carried over to the water-splitting process and result in impure hydrogen in the product stream.

$$C + H_2O \rightarrow CO + H_2 \quad (5.4)$$

$$C + 2H_2O \rightarrow CO_2 + 2H_2 \quad (5.5)$$

It is important to mention that in terms of the purity of hydrogen produced which is critical for water-splitting processes, a membrane system (if gas-tight) should give only hydrogen in water as a product (as the product stream never sees the reducing surface).

5.2.3 Post operation characterisation

After the 15 redox cycles were completed, the powder samples were removed and reweighed. Sample loss was observed for all OCM samples. BSCF5582, LSCF6428 and LSF731 powders suffered 12%, 10% and 9% loss in mass respectively. These mass losses are large and the most suitable explanation is due to powder lost during the experiment and/or during removal of the sampling tube from the microreactor. Irreversible oxygen removal and also impurities burnout cannot be neglected.

The membrane fragments were characterised by SEM-EDS (only remarkable results are presented) after performing the TPR/TPO experiments. BSCF5582 and LSCF6428 microscopy surface morphologies (Figure 5.4) appears to be rougher than the fresh samples, however spot EDS analysis (Table 5.3) did not show evidence of any foreign element compared to the fresh materials (BSCF5582 already presented sulfur) nor was evidence of segregation of elements observed.

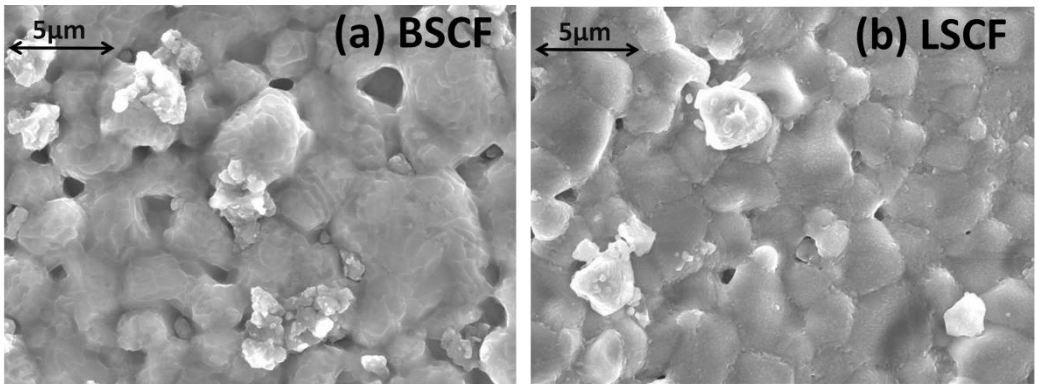

Figure 5.4Post operation SEM images of (a) BSCF5582 and (b) LSCF6428 membrane fragments after 15th TPR/TPO cycles.

Table 5.3 Spot EDS analyses of fresh microtubes fragments after 15th TPR/TPO cycles.

Material	Approximate atom (%)					
	La	**Ba**	**Sr**	**Co**	**Fe**	**S**
BSCF5582	-	24.1	15.4	38.0	14.5	8.0
LSCF6428	28.8	-	11.2	12.0	48.0	-
LSF731 point 0	6.3	-	42.3	-	39.4	12.0
LSF731 point 1	4.0	-	40.2	-	55.8	-

Post operation SEM images from the LSF731 membrane fragments are presented in Figure 5.5. As can be observed, the surface is decorated with a sponge-like cluster (point 0) of *ca* 60µm size that differs from the surface microscopy structure (point 1). Spot EDS indicated enrichment of strontium and presence of sulfur in the sponge-like cluster (point 0) and enrichment of strontium at the surface (point 1). It is also important to notice the increase of iron content (to the expected composition of $La_{0.7}Sr_{0.3}FeO_{3-\delta}$) at the membrane surface when compared with the fresh membrane fragment. It seems that the fresh LSF731 material possessed a sulfur layer, which started to leach out after 15 TPR/TPO cycles. It is important to state that EDS is a quick semi-quantitative analysis technique thus extra characterisation methods are required to indicate any surface modification. Further characterisation studies of the LSF731 fresh microtubes (*Section 5.3.1*) and post membrane-based steam reforming operation (*Section 5.3.4*) are presented later in this work.

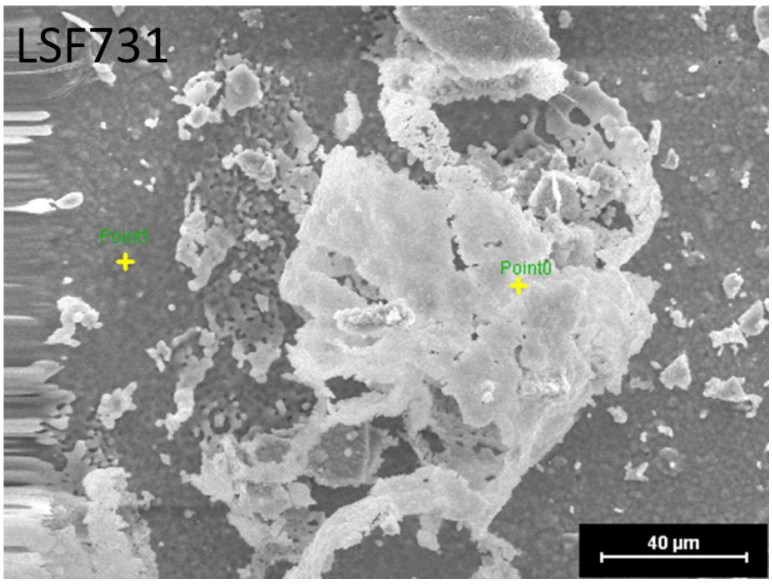

Figure 5.5 Post operation SEM images of the LSF731 membrane fragment after 15th TPR/TPO cycles.

5.3 Membrane Experiments

Oxygen permeation and membrane-based steam reforming experiments were performed using the new module design described in *Section 3.4.3.2*. The LSCF6428 and LSF731 membrane modules were constructed and each comprised of four microtubes. The BSCF5582 membrane module was constructed with only one microtube. The SW furnace was used in all membrane experiments described in this chapter.

5.3.1 Characterisation of fresh microtubes

LSCF6428 microtubes characterisation is not presented in this section as detailed studies with this OCM are presented in *Chapter 6*, including fresh and post operation characterisation. Images of the surfaces and cross-section of the fresh BSCF5582 and LSF731 microtubes are presented in Figure 5.6 and Figure 5.7 respectively.

As can be seen on the lumen-side surface (Figure 5.6b) of the BSCF5582 microtubes the grains are connected with clear boundaries. The grain size ranges from *ca* 2 to 8 µm. The shell-side surface (Figure 5.6a) shows an irregular surface decorated with small crystals (*ca* 1 µm). A regular cross-section (Figure 5.6c) could be observed. Spot EDS analysis (Table 5.4) show the presence of sulfur at both lumen and shell surfaces. The presence of sulfur has been already discussed in *Section 5.2.1*.

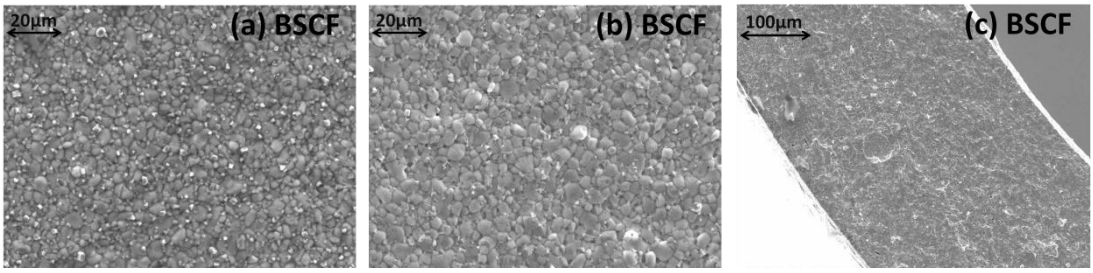

Figure 5.6 SEM images of the fresh BSCF5582 (a) shell-side surface of the microtubes, (b) the lumen-side surface and (c) cross-section.

As can be observed in Figure 5.7a and Figure 5.7b LSF731microtubes show irregular rough surfaces with unclear grains and boundaries. Spot EDS (Table 5.4) show the presence of sulfur and segregation of strontium on the LSF731 surfaces. A regular circular cross-section could be observed as shown in Figure 5.7c. The microtubes possess enclosed finger-like pores that are visible in the cross section but do not communicate with either membrane surface.

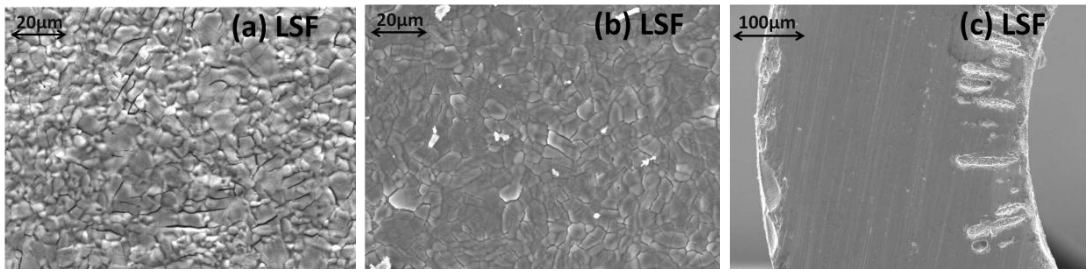

Figure 5.7 SEM images of the fresh LSF731 (a) shell-side surface of the microtubes, (b) the lumen-side surface and (c) cross-section.

A higher magnification SEM image of the cross-section (Figure 5.8) shows the presence of a layer of needle-like crystals covering the lumen-side surface. From spot EDS analyses (Table 5.4) was found this layer (point 0) is rich in sulfur and strontium. This layer was also observed in the shell-side surface and confirmed by EDS analysis. The bulk of the material (point 1) did not present sulfur or segregation of strontium. The stoichiometry at the bulk was closer to the expected to $La_{0.7}Sr_{0.33}FeO_{3-\delta}$.

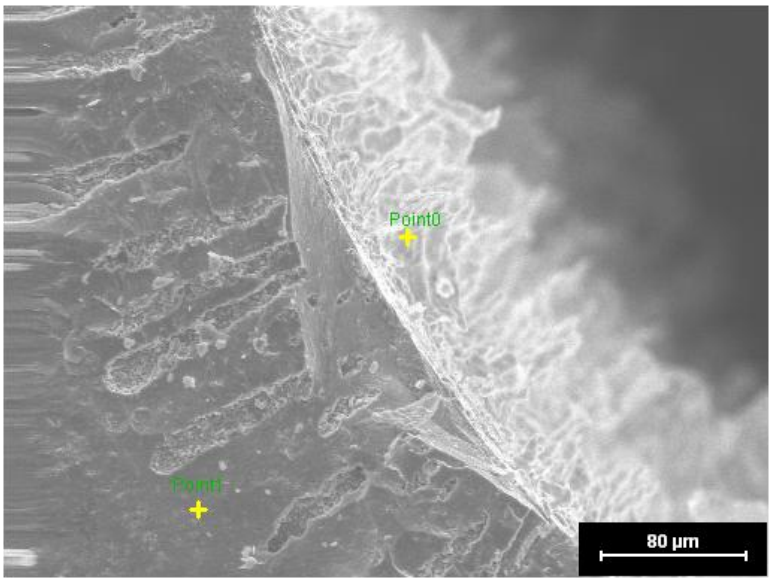

Figure 5.8 SEM image of the fresh LSF731 cross-section showing enriched sulfur/strontium layer.

Table 5.4 Spot EDS data of fresh BSCF5582 and LSF731 microtubes; LS (Lumen side) and SS (Shell side).

Material/ Location	Approximate atom (%)					
	La	Ba	Sr	Co	Fe	S
BSCF5582/(SS)	-	21.4	14.3	42.7	13.4	8.2
BSCF5582/(LS)	-	25.8	13.6	42.1	14.4	4.1
LSF731/(SS)	2.7	-	38.2	-	4.0	55.1
LSF731/(LS)	5.5	-	37.3	-	7.9	49.3
LSF731(point 0)	5.0	-	44.3	-	7.9	42.8
LSF731(point 1)	39.5	-	6.7	-	53.8	-

5.3.2 Oxygen Permeation

The oxygen permeation rate was measured on the lumen-side outlet as a function of the air flow rate on the shell-side when the sweep gas (argon) flow rate was kept constant at 20 ml (STP) min^{-1} on the lumen-side. Measurements were made for the microtubes LSCF6428 and BSCF5582 at 900°C and LSF731 at 950°C using SW furnace, as at 900°C the LSF731 microtubes did not show any oxygen permeation. The reason for that behaviour is explained later in *Section 5.3.4*.

Oxygen permeation measurements are presented in Figure 5.9. As expected, the oxygen permeation flux increases (to a limiting value showing the presence of surface exchange limitations) with increasing air flow rate, as the oxygen partial pressure on the shell-side is increased, consequently increasing the driving force for oxygen permeation (as expressed in Equation (2.11).

LSF731 and LSCF6428 microtubes showed similar oxygen permeation rates of *ca* 0.2µmol O_2 s^{-1}, however as explained before at different temperatures. With the LSCF6428 membrane the oxygen permeation rate increased from *ca* 0.15µmol O_2 s^{-1} to *ca* 0.2µmol O_2 s^{-1} when the air flow rate was raised from 50 to 100 ml(STP)min^{-1}. With the LSF731 microtube the oxygen permeation rate increased from *ca* 0.13µmol O_2 s^{-1} to *ca* 0.16µmol O_2 s^{-1} when the air flow rate was raised from 50 to 100 ml(STP)min^{-1}. No significantly changes were observed when the air flow rate was increased higher than 100 ml(STP)min^{-1}.

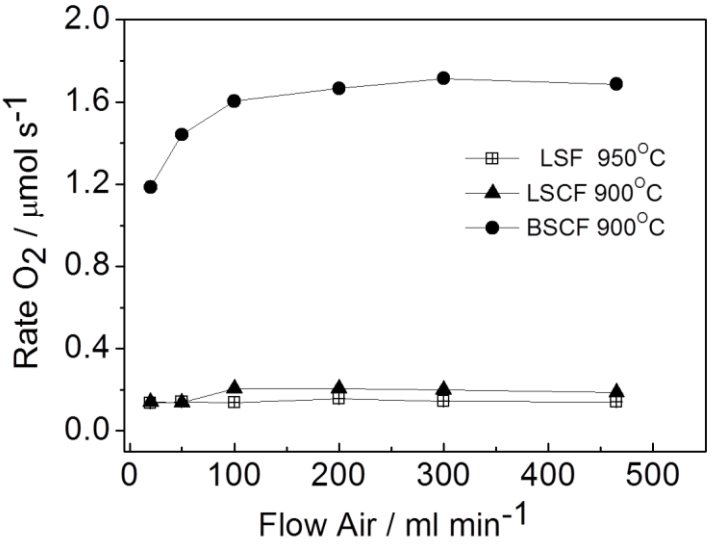

Figure 5.9 Oxygen permeation on the lumen-side outlet, varying air supplied on the shell side with argon as sweep gas on the lumen side at 20 ml min^{-1}.

BSCF5582 presented much higher oxygen fluxes than LSCF6428 and LSF731, indicating fast bulk transport of O^{2-} through the membrane. Similar studies also showed the same behaviour [7, 83]. Oxygen permeation rate increased from *ca* 1.2µmol O_2 s^{-1} to *ca* 1.6µmol O_2 s^{-1} when the air flow rate was raised from 20 to 100 ml(STP)min^{-1}. The highest permeation achieved in these experiments was *ca* 1.7µmol O_2 s^{-1} when the air flow rate was 300 ml(STP)min^{-1}. The importance of the membrane thickness is not apparent as BSCF5582 microtube has wall thickness twice as large as LSCF6428 and LSF731. This indicates surface oxygen exchange kinetics as the rate limiting step for oxygen permeation in BSCF5582 membranes

5.3.3 Membrane-based steam reforming

Membrane-based steam reforming at 900°C was undertaken directly after the oxygen permeation experiments. Water vapour was supplied to the shell side of the microtubes at 20 ml (STP) min^{-1} and methane was supplied at a total flow rate of 20 ml (STP) min^{-1} to the lumen side as a reducing gas.

To investigate the influence of oxygen partial pressure associated with hydrogen production, studies on surface oxidation and reduction processes were conducted. This focused on systematically varying the partial pressures of water vapour and the methane concentration. To analyse the influence of the reducing gas on hydrogen production with the microtubes, the concentration of methane was varied from 1.0% to 5.0%. The

influence of the oxidising gas was also studied by varying the water saturator temperature and consequently the water vapour concentration from 1.0% to 11.0%.

LSF731 did not show any hydrogen production during the membrane-based steam reforming experiments. Post operation analysis revealed that surface contamination may have caused this effect and is discussed in *Section 5.3.4.*

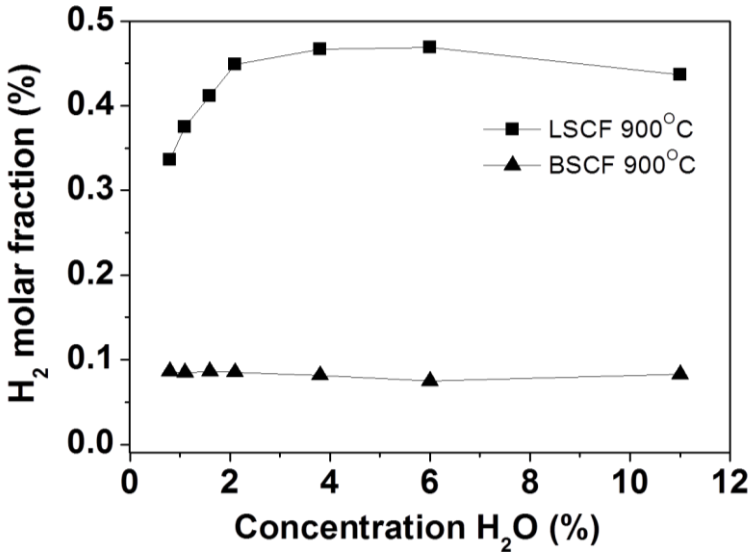

Figure 5.10 Hydrogen production molar fraction on the shell-side outlet at different water vapour concentrations (shell-side inlet) when methane was maintained constant on the lumen-side inlet at 5%. .

Investigation of the oxidation step was carried out by increasing the water partial pressure while the methane concentration was maintained at 5%. As can be observed in Figure 5.10 BSCF5582 hydrogen production maintained steady *ca* 0.08% when the water vapour concentration was increased, showing low oxidation activity to water vapour.

In the other hand with the increasing of water vapour from 1% to 6%, LSCF6428 hydrogen production increased from *ca* 0.33% to *ca* 0.46%. With increasing the water vapour concentration the oxygen partial pressure will be raised; consequently a higher driving force for oxygen permeation is produced and the level of hydrogen produced would also increase. However when the water vapour concentration was increased to 11% the hydrogen production decreased to *ca* 0.43% showing surface exchange limitations.

The influence of methane concentration was also investigated and presented in Figure 5.11; during this experiment water vapour was maintained constant at 7.2% (highest

oxidation level obtained from previous experiment). BSCF5582 and LSCF6428 hydrogen production increased from *ca* 0.03% to *ca* 0.08% and *ca* 0.2% to *ca* 0.44% respectively, when the methane concentration was raised from 1 to 5%.

These results demonstrate that hydrogen production can be improved by increasing the concentration of the reducing gas; consequently the oxygen permeated is rapidly consumed, establishing a higher oxygen partial pressure gradient across the microtubes and therefore a higher hydrogen production rate from water dissociation.

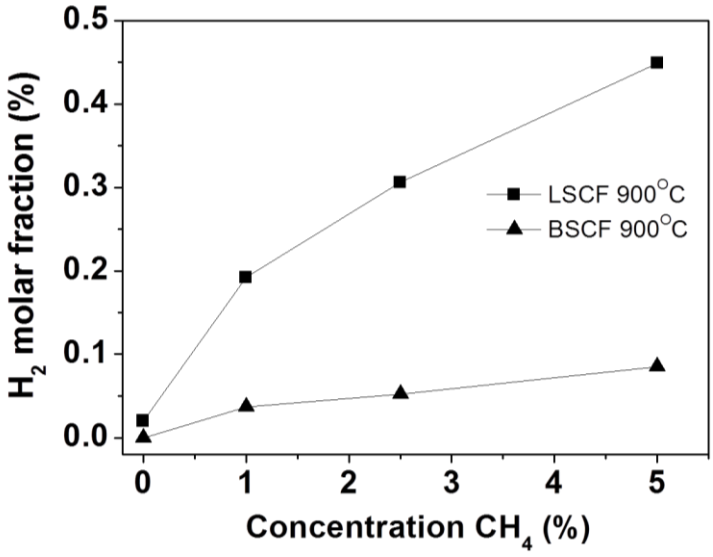

Figure 5.11 Hydrogen production molar fraction on the shell-side outlet at different methane concentrations (lumen-side inlet), when water vapour was maintained constant on the shell-side inlet at 7.2%.

5.3.4 Post operation characterisation

As explained in *Section 5.3.1*, LSCF6428 post operation characterisation is not presented here as detailed studies and characterisation with this OCM are discussed in *Chapter 6*.

BSCF5582 shell-side surface (exposed to water vapour) microscopy morphology (Figure 5.12a) did not show remarkable changes from the fresh microtube, however spot EDS (Table 5.5) revealed high segregation levels of barium and strontium. Apparently barium and strontium are leaching out from the microtube structure. Studies with BSCF5582 also showed strontium and barium segregation when exposed to high temperatures and water vapour. Leo *et al* assigned the formation of barium carbonate and strontium carbonate at the membrane surface which affected the oxygen ionic diffusion [164]. The formation of carbonates was unexpected and the authors speculated

the presence of carbon dioxide from the atmosphere in the distilled water fed to the evaporator. The BSCF5582 lumen-side surface (exposed to methane) showed a rougher surface than the fresh membranes as can be observed in Figure 5.12b. Spot EDS indicated segregation of barium and enrichment of sulfur when compared with the fresh membranes. Non-stability and perovskite structure modification have been reported when BSCF5582 membranes were exposed to reducing atmospheres [165, 166]. These results could indicate the reason for the low activity for hydrogen production via water splitting and methane activation. However other factors (i.e. surface exchange limitations and catalytic activity) cannot be neglected.

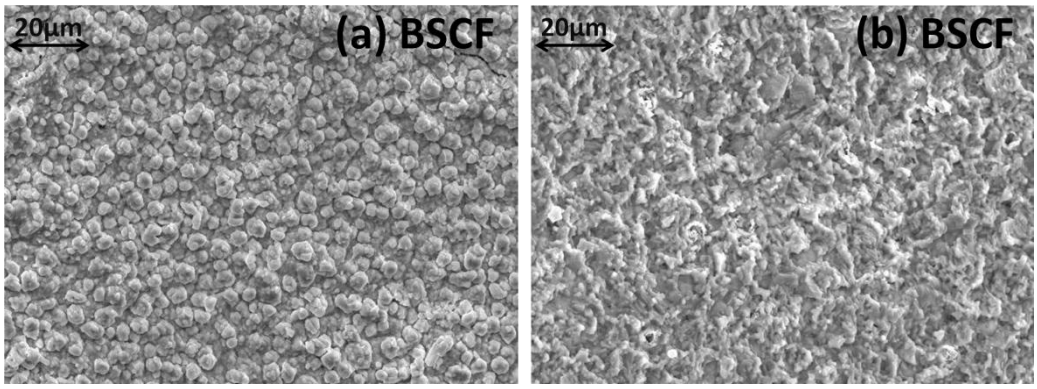

Figure 5.12 Post operation SEM images of BSCF5582 microtube (a) shell-side surface and (b) lumen-side surface.

As can be observed in Figure 5.13, LSF731 microtube presented a layer (point 0) which appears to sit on top of the shell-side surface (exposed to water). Spot EDS (Table 5.5) indicated this layer is rich strontium, however no evidence of sulfur (presented in the fresh microtubes) was found. Spot EDS indicated that the shell side underneath the layer (point1) did not present strontium enrichment. It seems the rich sulfur/strontium layer (presented in the fresh membranes) was leached out during the membrane-based steam reforming experiments.

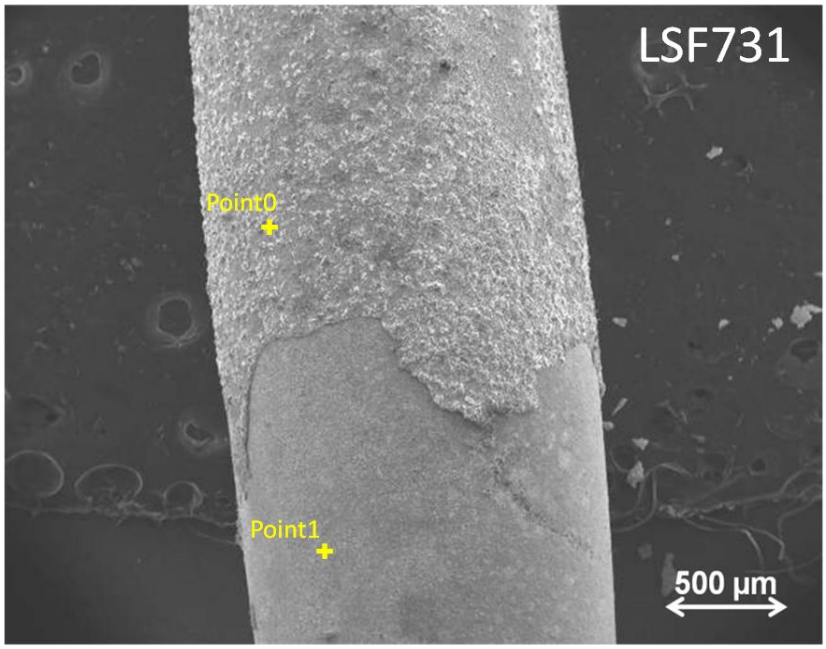

Figure 5.13 Post operation SEM images of LSF731 microtube shell-side surface showing dense strontium layer.

The rich strontium layer formed can clearly be observed in the cross-section SEM image (Figure 5.14) and has *ca* 10µm of thickness. It is plausible that this dense layer could be responsible for the lower than expected oxygen permeation rates and none hydrogen production using LSF731 microtubes.

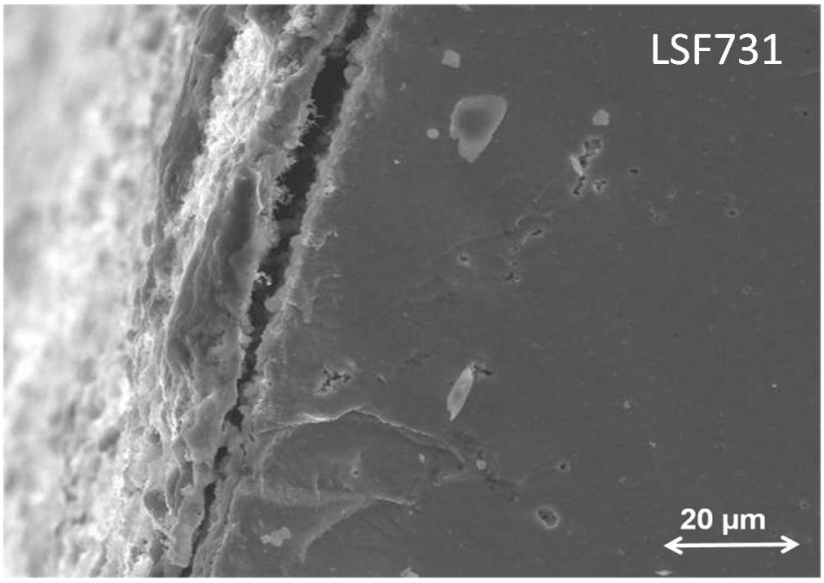

Figure 5.14 Post operation SEM images of LSF731 microtube cross-section showing dense strontium layer.

Table 5.5 Post operation EDS data of BSCF5582 and LSF731 microtubes.

Material/ Location	Approximate atom (%)					
	Ba	**La**	**Sr**	**Co**	**Fe**	**S**
BSCF5582 (SS)	42.3	-	34.6	12.4	6.9	3.8
BSCF5582 (LS)	47.8	-	10.0	13.2	4.5	24.5
LSF731/(SS)	-	2.3	27.0	-	67.9	2.8
LSF731/(LS)	-	25.7	19.3	-	55.0	-
LSF731(point 0)	-	2.0	45.2	-	52.8	-
LSF731(point 1)	-	36.0	6.9	-	57.1	-
LSF731 (bulk)	-	43.7	4.3	-	52.0	-

5.4 Summary

Temperature programmed reduction and oxidation cycles were carried out with the OCM materials to understand the kinetic behaviour and reaction steps involved during oxidation in water and reduction in methane. It is clear that both LSCF6428 and LSF731 materials showed better activity for hydrogen production than BSCF5582. However LSF731 membrane presented an enriched sulfur/strontium layer and may be reduced the relative permeation rate and consequently hydrogen production.

Oxygen permeation at 900°C showed that BSCF5582 microtubes possess higher oxygen permeation rates than LSCF6428. However LSCF6428 demonstrated better potential for hydrogen production from water splitting than BSCF5582. Hydrogen production from water splitting depends on the catalytic capability of the perovskite-type membrane surface to split water and activate methane. Fast bulk transport of O^{2-} through the membrane is not necessarily the main consideration. By varying water and methane concentrations, it was observed that hydrogen production can be improved by increasing the methane concentration supply.

During the studies presented in this chapter; LSCF6428 microtubes performed better for hydrogen production via membrane-based steam reforming among the other materials and it was chosen to long term studies presented in *Chapter 6*. The most suitable conditions of experiment (water vapour *ca* 7% and methane concentration at *ca* 5%), determined from varying water and methane concentrations in *Section 5.3.3*, would be applied during these studies.

Chapter 6

6 $La_{0.6}Sr_{0.4}Co_{0.2}Fe_{0.8}O_{3-\delta}$ microtubular membranes for hydrogen production from water splitting

6.1 Introduction

The work presented in this chapter has been published in the Journal of Membrane Science and the following sections have been adapted from this paper [167].

Based in the results from *Chapter 5* LSCF6428 has shown the best performance (under the experiments conditions) among the studied materials to hydrogen production by membrane-based steam reforming (Figure 6.1). The most suitable water vapour inlet concentration (7.2%) and methane inlet concentration (5%) were also obtained (highest oxidation and reduction levels) and applied in the following sections.

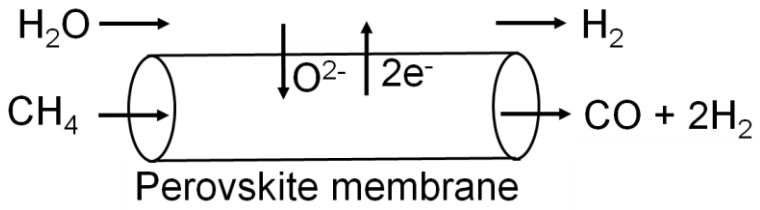

Figure 6.1 Schematic diagram of membrane-based steam reforming at 900°C

The membranes were subjected to two known axial temperature profiles (SW and LN furnaces) in the temperature of 900°C. The microtubes showed good stability under reaction conditions, operating over a total operation period of *ca* 400 hours of oxygen permeation (*Section 6.3*) followed by *ca* 400 hours of steam reforming (*Section 6.4*). An induction period of approximately 30 hours was observed before steam reforming commenced due to oxygen gradient re-establishment and oxygen transport through the membrane.

Previous work has lacked the detail necessary to conclusively prove that hydrogen production is due to oxygen permeation across the membrane (*e.g.* a perovskite membrane can store and release oxygen; a reduced surface will produce hydrogen over

some period of time without net oxygen permeation being required). In this work the exit gas composition from both sides of the membrane was analysed and material balances (*Section 6.5*) were obtain to demonstrate permeation (as opposed to dynamic changes in membrane state). Long duration operation was also carried out where permeation is more important than dynamic surface redox processes.

Post operation analysis (*Section 6.6*) of the microtubes revealed the presence of a strontium enriched dense layer on the water exposed membrane surface and of crystallites enriched with cobalt and sulfur on the methane feed side surface.

6.2 Characterisation of fresh LSCF6428

The XRD of the lumen-side and shell-side surfaces of unused fresh membranes (presented in *Appendix 6-A*) indicated the presence of a single perovskite phase and the absence of foreign phases. Spot EDS analysis (Table 6.1) also did not show the presence of foreign elements or segregation of any of the constituents of the perovskite.

Table 6.1EDS data of fresh LSCF6428 microtubes.

Location	**Approximate atom (%)**			
	La	**Sr**	**Co**	**Fe**
Fresh lumen-side	34.1	13.5	8.2	43.9
Fresh shell-side	28.6	16.5	12.4	42.5

As can be seen on the lumen-side surface of the microtubes (Figure 6.2a) the grains are connected with clear grain boundaries, surface cavities are also present. The grain size ranges from *ca* 1 to 5 µm. The shell-side surface (Figure 6.2b) shows an irregular rough surface. An irregular circular cross-section could be observed as shown in Figure 6.2c indicating wall thickness of *ca* 250 µm. The microtubes possess enclosed finger-like pores that are visible in the cross section but do not communicate with either membrane surface.

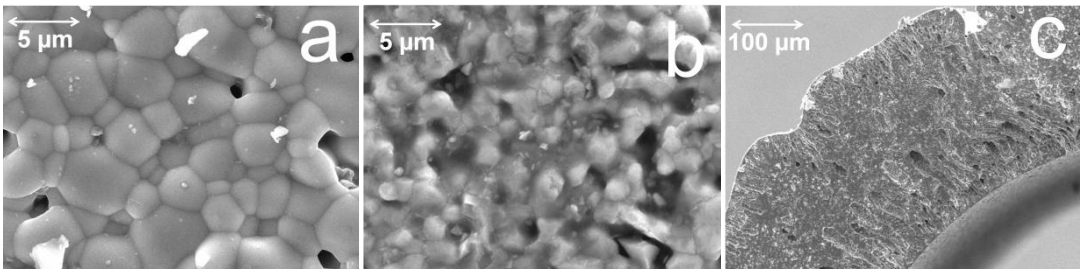

Figure 6.2 SEM images of the fresh (a) lumen-side surface of the microtubes, (b) the shell-side surface and (c) cross-section.

The treatment histories of the membrane modules reported in this chapter are provided in Table 6.2.

Table 6.2 Membrane treatment history

Heating/hold (^oC)	Cooling/hold (^oC)	Shell side sweep rate(s) (ml min^{-1})	Lumen side sweep rate(s) (ml min^{-1})	Duration (hours)
Experimental conditions (SW furnace 916°C / 900°C)				
25 to 916	-	Atmospheric air – 0	Atmospheric air – 0	29.7
916	-	Synthetic air – 20	Argon – 20	400.6
-	916 to 900	Synthetic air – 20	Argon – 20	0.5
-	900	Synthetic air – 20	Argon – 20	163.4
-	900	H_2O (7.2%) – 20	CH_4 (5%) – 20	240.0
-	900	H_2O (7.2%) – 20	Argon – 20	5.0
-	900	H_2O (7.2%) – 20	CH_4 (5%) – 20	21.4
-	900 to 25	Atmospheric air – 0	Atmospheric air – 0	29.1
Experimental conditions (LN furnace 900°C)				
25 to 900	-	Atmospheric air – 0	Atmospheric air – 0	29.1
900	-	Synthetic air – 20	Argon – 20	411.7
900	-	H2O (7.2%) – 20	CH4 (5%) – 20	430.2
-	900 to 25	Atmospheric air – 0	Atmospheric air – 0	29.1
Experimental conditions (LN furnace 960°C)				
25 to 960		Atmospheric air – 0	Atmospheric air – 0	31.1
960		H_2O (7.2%) - 20	CH_4 (5%)- 20	333
	960 to 25	Atmospheric air – 0	Atmospheric air – 0	31.1

6.3 Oxygen permeation studies

For the purposes of this study, the oxygen permeation investigation was first undertaken using both furnaces (SW and LN) to verify the capability of the membranes to permeate oxygen. Air was supplied to the shell side of the microtubes at 20 ml (STP) min^{-1} and argon at 20 ml (STP) min^{-1} was used as the sweep gas on the lumen side.

Generally, as can be seen in Figure 6.3 and Figure 6.4, the microtubes could permeate oxygen continuously for at least 400 hours. The presence of nitrogen in the outlet of the sweep side was observed in both experiments at similar levels. The oxygen permeation rate is adjusted to take this into account by subtracting the rate of oxygen leakage based

on the rate of nitrogen leakage (assuming a 1:4 oxygen:nitrogen ratio). Furthermore, fluctuations of the calculated oxygen and nitrogen permeation and leakage rates can be seen in both oxygen permeation experiments. This may be related to actual fluctuation in permeation rates or could be as a result of fluctuations in inlet flow rates or temperature and/or pressure. The fluctuations follow a 24 hours pattern and issues with the mass flow controller calibration cannot be neglected. Similar fluctuations have previously been reported in studies using the same rig used in this research [83]

Using the SW furnace (Figure 6.3) the oxygen permeation and nitrogen leakage rates at 916°C were initially *ca* 0.25 µmol O_2 s^{-1} and 0.08 µmol N_2 s^{-1} respectively indicating mainly oxygen permeation through solid state transport. Over time the oxygen permeation gradually increased to *ca* 0.33 µmol O_2 s^{-1} and the nitrogen leakage rate decreased to *ca* 0.03 µmol N_2 s^{-1} and was constant during the remainder of this experiment. The behaviour may be associated with slow disordering of oxygen vacancies causing the gradual increase of the oxygen permeation rate. After 400 hours at 916°C the temperature was lowered to 900°C to probe sensitivity to small temperature changes. The rate of oxygen permeation decreased over two hours to 0.30 µmol O_2 s^{-1} showing the expected dependence on temperature. Over the next 150 hours at this temperature the fluctuations in the rate continued but the underlying permeation rate remained constant.

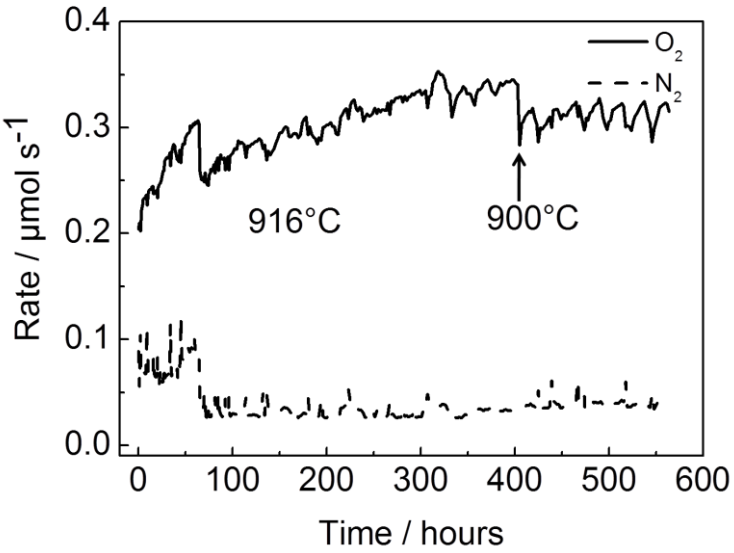

Figure 6.3 Oxygen permeation with air supplied on the shell side at 20 ml min^{-1} and argon as sweep gas on the lumen side at 20 ml min^{-1}using SW furnace (916°C and 900°C).

Using the LN furnace (Figure 6.4) the initial oxygen permeation and nitrogen leakage rates were *ca* 0.15 µmol O_2 s^{-1} and 0.04 N_2 µmol s^{-1} respectively. After 200 hours the nitrogen leakage rate decreased to *ca* 0.03 µmol N_2 s^{-1} and then remained constant. The oxygen permeation rate gradually increased during the first 300 hours of the experiment, reaching the highest value of 0.24 µmol O_2 s^{-1}, followed by a decrease over ten hours back to the starting value of *ca* 0.15 µmol O_2 s^{-1}. The membranes used in the LN furnace gave a lower oxygen permeation rate than those used in the SW furnace. This is unexpected as the LN furnace has a longer central hot zone; post operation analysis revealed that surface contamination may have caused this effect and is discussed in *Section 6.6*.

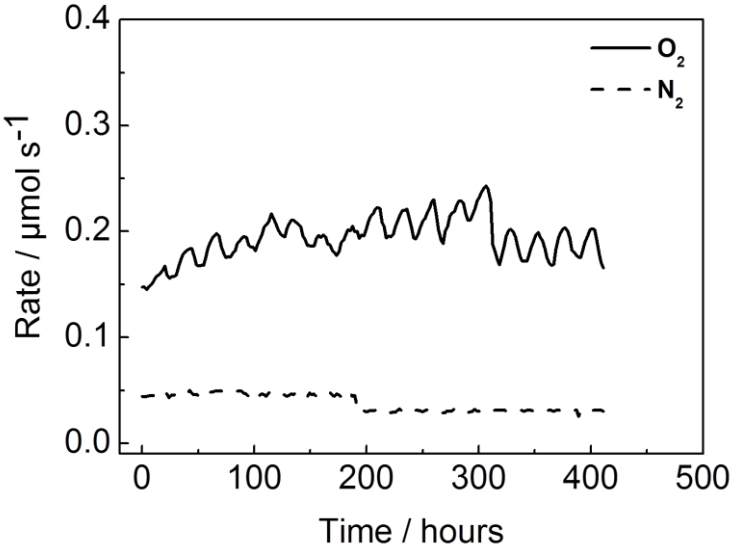

Figure 6.4 Oxygen permeation with air supplied on the shell side at 20 ml min^{-1} and argon as sweep gas on the lumen side at 20 ml min^{-1}using LN furnace (900°C).

6.4 Membrane-based steam reforming studies

Membrane-based steam reforming at 900°C was undertaken directly after the oxygen permeation experiments. Water vapour (nominally 7.2%) was supplied to the shell side of the microtubes at 20 ml (STP) min^{-1} and methane, nominally 5% (measured as 4.8% ± 0.5%), was supplied at a total flow rate of 20 ml (STP) min^{-1} to the lumen side as a reducing gas. At the same time as hydrogen is produced by water splitting on the shell side of the membrane, hydrogen, carbon dioxide and carbon monoxide are produced on the lumen side. The low levels of background oxygen and nitrogen leaks into the shell side are not shown (these were characterised earlier with alumina membranes in *Section 4.4* and do not differ significantly here). In addition the methane mole fraction in the

outlet of the lumen side is not shown as this mole fraction is much higher than that of the other species. However, this mole fraction is used in determining material balances and did not behave in any unexpected way.

6.4.1 Induction Period

As shown in Figure 6.5a at the shell-side outlet using the SW furnace, an induction period of *ca* 30 hours was observed before any trace of hydrogen was detected. The same induction period for methane consumption was also observed at the lumen side (Figure 6.5c). In previously similar reported work [136, 138, 168, 169] , there tends to be an implicit assumption that any hydrogen production is due to oxygen permeation (and not just a change in the state of the membrane) and that this permeation rate is established rapidly and remains at steady state. It must recall that prior to this experiment the membranes were used for oxygen permeation experiments and as such would still hold the previously established oxygen chemical potential gradient. It would be expected that it may take some time for this gradient to re-establish itself (depending upon the rate-determining steps involved, note the more reducing gas is always supplied to the lumen) and this could be a reason for the induction (and the induction period itself will depend upon the nature of preceding experiments).

Based on a typical oxygen permeation rate for hydrogen production (0.04 μmol O s^{-1}), an estimated effective area for permeation (8 cm^2 for the SW furnace and 19 cm^2 for the LN furnace), a membrane thickness of 250 μm, an assumed maximum change in the degree of nonstoichiometry, $\Delta\delta$, of 0.5 and a membrane molar volume of 35 cm^3 mol^{-1} [170], a time constant for membrane oxidation/reduction of *ca* 20 hours (SW furnace) and *ca* 50 hours (LN furnace) can be estimated. This is similar to the length of the induction period.

6.4.2 SW furnace (900°C)

As can be observed Figure 6.5a shows that for the membranes in the SW furnace, the level of hydrogen increased and after *ca* 50 hours reached a steady state mole fraction in the gas stream of *ca* 0.35%. After 240 hours the methane supply through the lumen side was interrupted and argon was introduced as the sweep gas for five hours as presented in Figure 6.5b. The hydrogen level at the shell side rapidly decreased, to a low level (0.02%) but we note that it did not reach 0.002% as would be expected based on the

blank experiment (*Section 4.4*). Also was noticed that the cross-membrane methane leak into the shell side decreased to zero.

The resultant low level of hydrogen production from water splitting was one order of magnitude higher than that obtained for the blank experiment; the produced hydrogen may be from water splitting on the membrane surface but in the absence of permeation (no oxygen-containing species were detected on the lumen side during this operation). This further demonstrates the need for an oxygen vacancy concentration gradient across the membrane in order to observe significant steady state water splitting. Reintroduction of methane established the oxygen vacancy gradient and hydrogen was observed at approximately the same level as before interruption. Low level hydrogen production has also been observed in membrane-based WGS studies when the carbon monoxide supply was interrupted but the water vapour feed maintained [142].

Pulses of hydrogen were observed superimposed on steady hydrogen production at both sides of the microtubes as observed in Figure 6.5. These two sets of pulses do not occur at exactly the same time. Similar periodic fluctuations have previously been reported in methane oxidation studies using LSCF6428 microtubes but the origin of this effect is not clear [83].

The level of hydrogen at the lumen side (methane oxidation side) increased after induction and reached a steady state after *ca* 60 hours of *ca* 0.16%, as shown in Figure 6.5c, with mainly carbon dioxide and hydrogen being produced (note that the pulses result in carbon monoxide production and not carbon dioxide production). The level of carbon dioxide decreased after 50 hours to a steady state of *ca* 0.09%.

Traces of methane were observed in the shell-side outlet and should be related to gas phase transport through micro-cracks in the membranes. The level of methane started to increase after 120 hours and increased significantly after 260 hours; this leakage is related to the failure of the membranes. The failure can be related to chemical stress due to reduction and oxidation of the perovskite and also axial stress due to the temperature gradient along the length of the membrane.

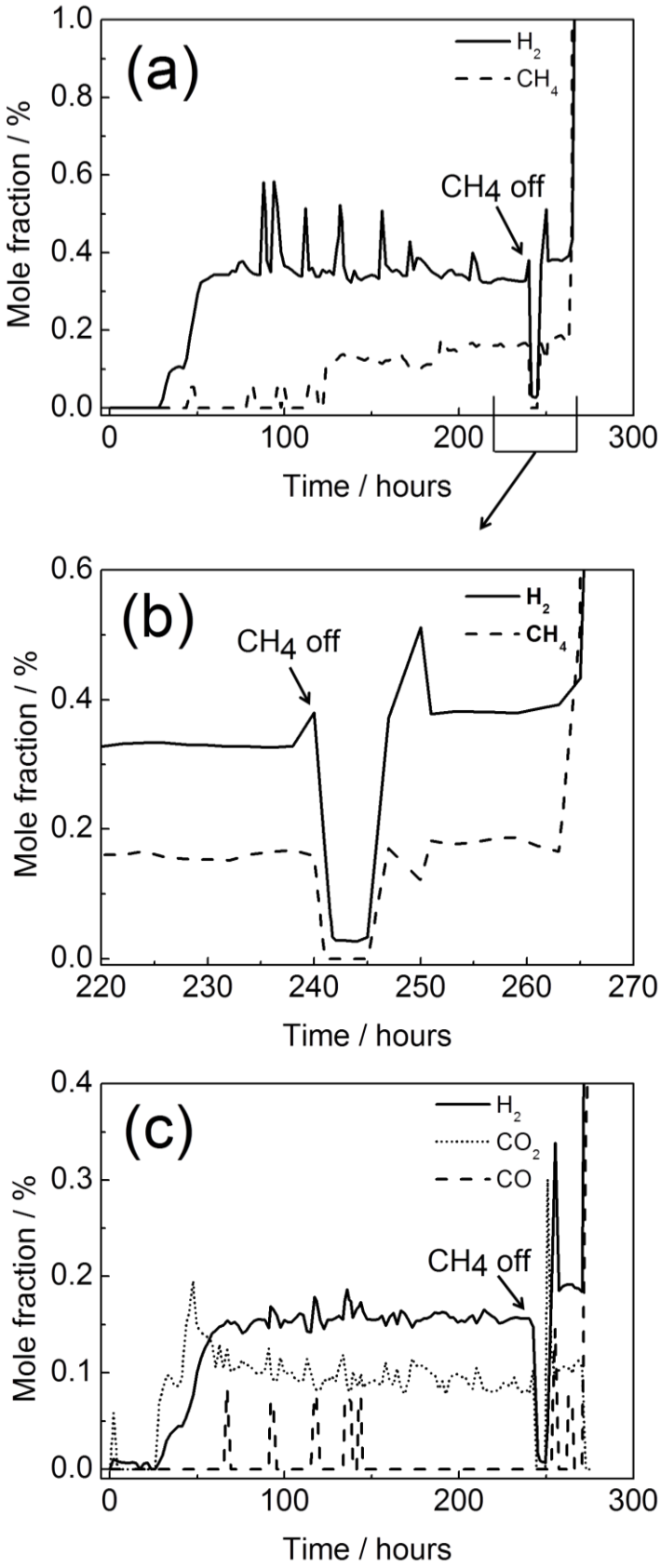

Figure 6.5 Outlet composition from membrane-based steam reforming at 900°C using the SW furnace on the (a) shell side (water-splitting side) when methane is supplied as a reducing gas at the lumen side, (b) expanded view of showing the affect of interruption of the methane supply with argon and (c) lumen side (methane oxidation side) when methane is supplied as a reducing gas.

6.4.3 LN furnace (900°C)

Similar to the SW furnace, the membranes used with the LN furnace had an induction period of *ca* 30 hours before any trace of hydrogen or products of methane consumption (Figure 6.6) were detected at the shell side and lumen side respectively.

The level of hydrogen at the shell side (Figure 6.6a) increased and peaked to *ca* 0.5% and then fell to *ca* 0.28%. After 220 hours it rose to *ca* 0.35% and remained at this level until termination of the experiment. The hydrogen production rate is essentially the same as for the SW furnace even though the temperature profile would be expected to result in a higher hydrogen production rate for the LN furnace. Post operation analysis revealed that surface contamination may have caused this effect and is discussed in *Section 6.6.*

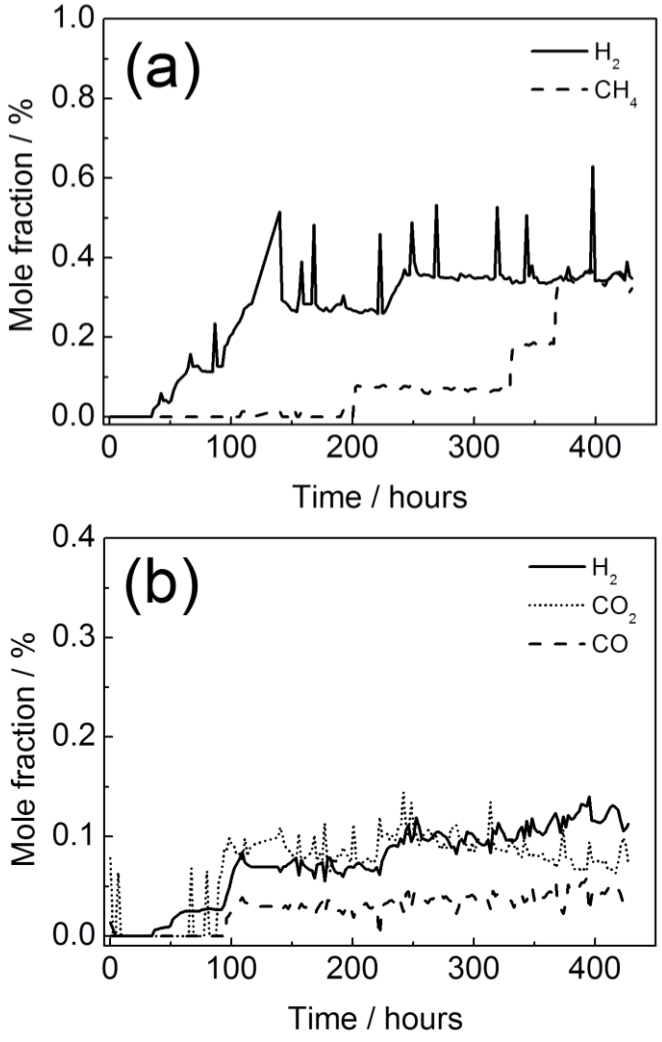

Figure 6.6 Outlet composition from membrane-based steam reforming at 900°C using LN furnace on the (a) shell side (water-splitting side) and (b) lumen side (methane oxidation side) when methane is supplied as a reducing gas.

Pulses of hydrogen were also observed in the experiments using the LN furnace. As shown in Figure 6.6b carbon monoxide, carbon dioxide and hydrogen were produced on the lumen side using the LN furnace. The longer isothermal section of the LN furnace gave carbon monoxide and carbon dioxide in contrast to the SW furnace which gave mostly carbon dioxide with a trace of carbon monoxide. This difference in carbon selectivities will be due to differences in oxygen permeated and the different effective reactor residence times changing the relative importance of further reactions of carbon dioxide through [171], *e.g.*, dry reforming (Equation (6.1)) where carbon dioxide reacts with methane to produce carbon monoxide and hydrogen;

$$CO_2 + CH_4 \rightarrow 2H_2 + 2CO \tag{6.1}$$

and reverse water-gas shift (Equation (6.2)) where carbon dioxide reacts with hydrogen to produce carbon monoxide and water.

$$CO_2 + H_2 \rightarrow CO + H_2O \tag{6.2}$$

6.4.3.1 Membrane-based steam reforming 960°C

Membrane-based steam reforming was carried out under the same inlet flow rate and composition conditions using the LN furnace at 960°C with a fresh membrane module. Here, we report only the shell-side outlet gas composition. As can be seen in Figure 6.7 hydrogen level rapidly increased to *ca* 0.74 % and maintained this level throughout the experiment.

This result showed that the driving force of oxygen permeation has an exponential dependence with temperature as the rate of hydrogen production at 960°C was approximately double that observed at 900°C (Figure 6.6a) and the required oxygen vacancy gradient was rapidly established. The level of cross-membrane methane leak was constant (0.02%) during most of the experiment but increased significantly after 300 hours. This is directly related to the mechanical failure of the membranes. Again hydrogen pulses are observed but at this temperature they are more intense and occur in a more periodic fashion, approximately every 100 hours. For all membrane modules the membranes cracked near the centre and the investigation stopped after the total elapsed time indicated in the figures.

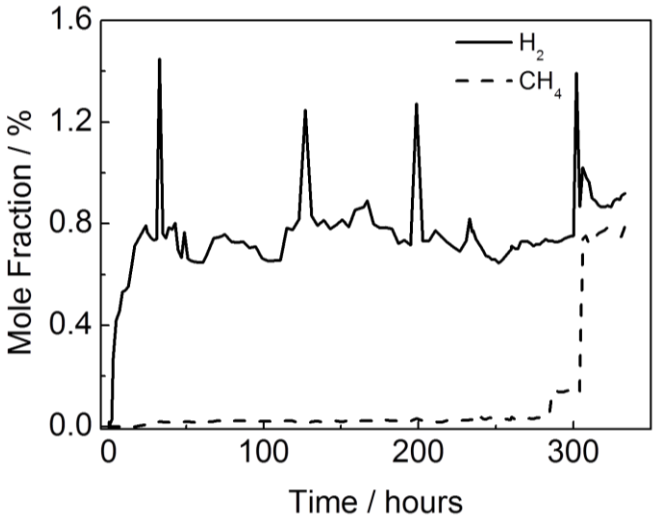

Figure 6.7 Shell-side outlet composition from membrane-based steam reforming at 960°C using LN furnace when methane is supplied as a reducing gas.

6.5 Material Balance

In order to perform material balances for the steam reforming experiments at 900˚C, a table showing the average product mole fractions from 100 to 200 hours (SW furnace) and 150-350 (LN furnace) is provided (Table 6.3). The table also shows the uncertainty in measuring the gas phase mole fractions of the products (approximately 10% error in absolute values – note that errors in absolute values and not relative values are needed because the material balance requires the consolidation of data from two independent GCs; this leads to higher uncertainties). Error analysis is presented in *Appendix 6-B*.

Table 6.3 Average mole fractions of products from membrane-based steam reforming at 900°C using SW furnace (between 100 and 200 hours) and LN furnace (between 150 and 350 hours).

	H_2^{out} (%)	CH_4^{out} (%)	CO^{out} (%)	CO_2^{out} (%)
SW furnace				
Shell side (SS)	0.366 ± 0.036	0.102 ± 0.010	-	-
Lumen side (LS)	0.159 ± 0.016	4.095 ± 0.409	0.011 ± 0.001	0.094 ± 0.009
LN furnace				
Shell side (SS)	0.330 ± 0.033	0.064 ± 0.006	-	-
Lumen side (LS)	0.087 ± 0.008	4.101 ± 0.410	0.033 ± 0.003	0.091 ± 0.009

We can estimate the amount of oxygen transported across the membrane from both the lumen-side composition change and the shell-side composition change. These amounts of oxygen can then be compared to see if the oxygen balance closes within the uncertainty due to the analytical technique.

On the shell side the oxygen permeated (in this case removed), OP_{SS}, is simply equal to the rate of hydrogen production (hydrogen mole fraction in the outlet, $H_{2,SS}^{out}$, minus hydrogen mole fraction in the inlet (zero in this case), $H_{2,SS}^{in}$, multiplied by the total molar flow on the shell side, $n_{T,SS}$):

$$OP_{SS} = \left(H_{2,SS}^{out} - H_{2,SS}^{in}\right) n_{T,SS} \tag{6.3}$$

Or

$$OP_{SS} = H_{2,SS}^{out} n_{T,SS} \tag{6.4}$$

On the lumen side the permeated oxygen, OP_{LS}, appears in the carbon oxides and would also appear in water (not monitored).

$$OP_{LS} = \left(2\left(CO_{2,LS}^{out} - CO_{2,LS}^{in}\right) + \left(CO_{LS}^{out} - CO_{LS}^{in}\right) + \left(H_2O_{LS}^{out} - H_2O_{LS}^{in}\right)\right) n_{T,LS} \tag{6.5}$$

We assume that all carbon monoxide and carbon dioxide produced results in the simultaneous production of hydrogen and/or water (the role of carbon deposition is neglected):

$$\left(H_{2,LS}^{out} - H_{2,LS}^{in}\right) + \left(H_2O_{LS}^{out} - H_2O_{LS}^{in}\right) = 2\left(CO_{2,LS}^{out} - CO_{2,LS}^{in}\right) + 2\left(CO_{LS}^{out} - CO_{LS}^{in}\right) \tag{6.6}$$

Therefore water production can be estimated by:

$$\left(H_2O_{LS}^{out} - H_2O_{LS}^{in}\right) = 2\left(CO_{2,LS}^{out} - CO_{2,LS}^{in}\right) + 2\left(CO_{LS}^{out} - CO_{LS}^{in}\right) - \left(H_{2,LS}^{out} - H_{2,LS}^{in}\right) \tag{6.7}$$

Substituting into (6.5) for OP_{LS} gives:

$$OP_{LS} = 4\left(CO_{2,LS}^{out} - CO_{2,LS}^{in}\right) + 3\left(CO_{LS}^{out} - CO_{LS}^{in}\right) - \left(H_{2,LS}^{out} - H_{2,LS}^{in}\right) \tag{6.8}$$

Or in the case of none of these components being present in the feed:

$$OP_{LS} = \left(4CO_{2,LS}^{out} + 3CO_{LS}^{out} - H_{2,LS}^{out}\right) n_{T,LS} \tag{6.9}$$

Based upon the above expressions for the experiments, using the SW furnace, the rate of oxygen removal from the shell side (OP_{SS}) is 0.054 ± 0.005 µmol O s^{-1} and the oxygen permeation rate to the lumen side (OP_{LS}) is 0.037 ± 0.01 µmol O s^{-1}. Using the LN furnace, OP_{SS} and OP_{LS} are 0.049 ± 0.005 µmol O s^{-1} and 0.056 ± 0.01 µmol O s^{-1}, respectively. The values of OP_{SS} and OP_{LS} show that within measurement error the oxygen removed from the shell side matches the oxygen permeated to the lumen side

for the LN experiment. For the SW experiment there is some disagreement but the error is relatively small compared to the flux and does not appear to be a cause for concern.

The closure of the oxygen material balance is supporting evidence that the hydrogen production from water splitting is directly related to the oxygen permeation flux through the membrane. The carbon balance closed within the measurement uncertainty. Furthermore, after 400 hours of operation there were no visible signs of carbon build up anywhere in the system indicating that rate of carbon accumulation is low.

6.5.1 Conversion and selectivity

For the SW furnace the methane conversion (Equation (6.10)) was 2.1% ± 0.2 and the water conversion (Equation (6.11)) 5.0%. ± 0.5. For the LN furnace the conversions were 2.5% ± 0.2 and 4.6%. ± 0.4. This confirms that both membranes were operated under differential conditions (conversions less that 10%).

$$XCH_4 = (CO_{2,LS}^{out} + CO_{LS}^{out}) / CH_{4,LS}^{in} \tag{6.10}$$

$$XH_2O = H_{2,SS}^{out} / H_2O_{SS}^{in} \tag{6.11}$$

On the lumen side, in both cases (SW and LN furnace) the selectivity to carbon dioxide, $S_{CO2,LS}$, is greater than 0.7 consistent with a degree of total oxidation where,

$$S_{CO2,LS} = CO_{2,LS}^{out} / \left(CO_{2,LS}^{out} + CO_{LS}^{out}\right) \tag{6.12}$$

The selectivity to hydrogen, $S_{H2,LS}$, is 0.75 ± 0.004 for the SW furnace and 0.35 ± 0.002 for the LN furnace where the selectivity to hydrogen is defined in terms of exit carbon oxide mole fractions in light of the lack of information on the exit water mole fraction,

$$S_{H2,LS} = H_{2,LS}^{out} / 2\left(CO_{2,LS}^{out} + CO_{LS}^{out}\right) \tag{6.13}$$

The selectivity to water is therefore 0.25 ± 0.004 and 0.65 ± 0.002, again indicating significant total oxidation.

6.6 Post operation characterisation

After membrane failure the module was cooled down to room temperature under air. Membrane samples from the "hot" zone (central zone) and "cold" zone (outside the furnace) were taken from the modules used in the SW (900 and 916˚C) and LN (900˚C) furnaces for SEM, EDS and XRD; the analysed samples were uncrushed.

6.6.1 SW furnace

The XRD patterns of the membranes using the SW furnace were not remarkable; reflections corresponding to the fresh LSCF6428 perovskite were observed and none foreign elements were found.

Post operation SEM images from the membranes used in the SW furnace are presented (only remarkable results) in Figure 6.8. As can be observed the lumen surface (Figure 6.8a) at the cold zone had become decorated with small crystallites less than 1 μm in size (absent in the fresh membranes). Spot EDS (Table 6.4) on the crystallites indicated the presence of sulfur and enrichment of cobalt. Possible sources of sulfur contamination include the methane feed and the polyether sulfone used to form the membrane by the phase inversion technique [161, 162].

The hot zone shell-side membrane surface (Figure 6.8b) shows the development of cracks and the presence of needle and sphere-like crystals. There was no evidence from EDS or XRD that these needles and spheres had a composition different from the bulk membrane. EDS indicated the presence of carbon in isolated areas for both the shell-side and lumen-side surfaces; it can be concluded that this carbon originates from the methane. Carbonates were not observed in the XRD patterns but have been reported previously in POM studies [90].

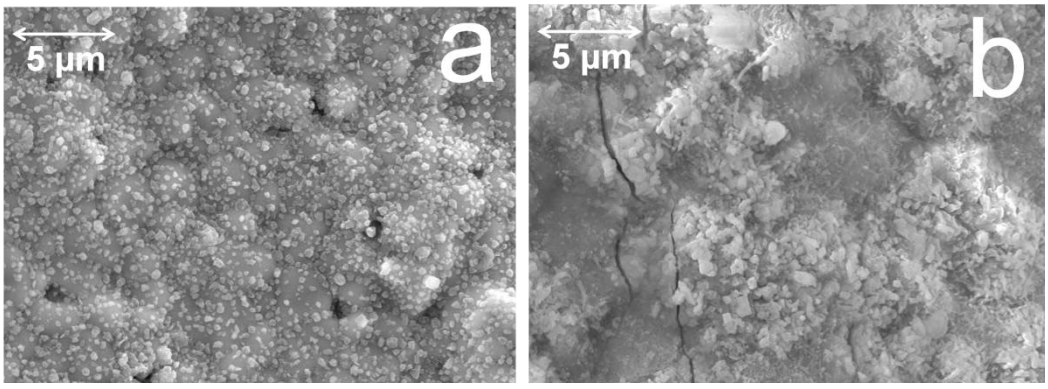

Figure 6.8 Post operation SEM images of the microtubes using the SW furnace: (a) the lumen-side surface of cold zone showing small crystals, and (b) the shell-side surface of the hot zone showing the development of cracks on the membrane surface and the presence of needle and sphere-like crystals.

Table 6.4 Post operation EDS data of microtubes using SW furnace.

Location	Approximate atom (%)					
	La	**Sr**	**Co**	**Fe**	**S**	**C**
Cold zone lumen-side surface crystals	10.7	3.4	28.5	46.3	11.1	-
Cold zone lumen-side surface (carbon spot)	3.7	2.3	0.8	4.3	-	88.9
Hot zone lumen-side surface (carbon spot)	3.0	1.5	1.3	3.9	-	90.3
Hot zone shell-side surface (carbon spot)	7.3	42.1	6.0	14.8	-	29.8

6.6.2 LN furnace

The XRD patterns presented in Figure 6.9 provided evidence of SiO_2 (PDF01-083-2465) contamination at the hot zone shell-side membrane surface when using the LN furnace; the contamination probably has its origin in the silicone sealant or quartz shell. In addition there is evidence of segregation of SrO (PDF01-074-1227) and La_2O_3 (PDF00-022-0641) at both the hot and cold zones at the shell-side surface. Spot EDS (Table 6.5) did not confirm deposition of SiO_2 but confirmed enrichment of strontium.

Table 6.5 Post operation EDS data of microtubes using LN furnace.

Location	Approximate atom (%)					
	La	**Sr**	**Co**	**Fe**	**S**	**C**
Hot zone lumen-side surface crystals	10.5	8.7	58.4	17.3	5.1	-
Hot zone shell-side surface	5.6	69.6	4.8	20.0	-	-

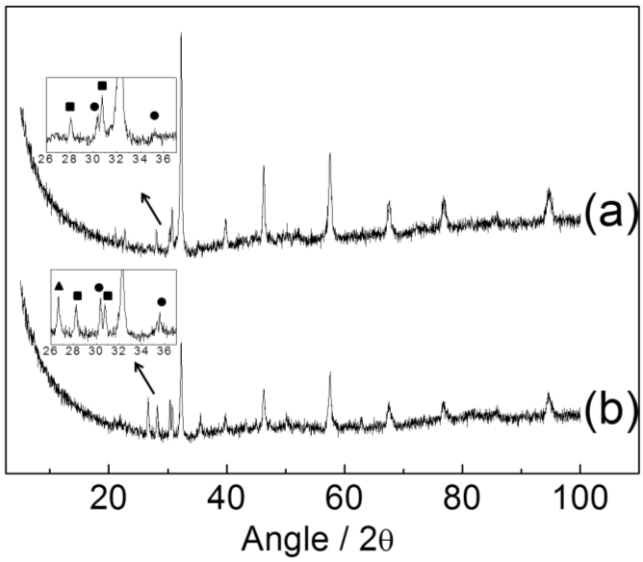

Figure 6.9 Post operation XRD pattern of microtubes using the LN furnace of (a) shell-side cold zone and (b) shell-side hot zone. Low intensity peak assignments; (▲) SiO_2 (■)) La_2O_3 (●) SrO.

Turning to microstructural changes the membranes used in the LN furnace features similar to those described for SW furnace. In Figure 6.10a it can be seen that in the hot zone the lumen-side surface is sparsely decorated with small crystals of *ca* 1 μm in size (not observed in the cold zone in contrast to the case of the SW furnace). EDS unambiguously indicated high cobalt content and the presence of sulfur again. The shell-side membrane surface in the hot zone using the LN furnace also had needle like crystals (Figure 6.10b), which were more pronounced than those formed using the SW furnace (Figure 6.9(b)). Spot EDS indicated enrichment of strontium but no carbon, silicon or sulfur. These needles are also observed in cross-section (Figure 6.10c) and appear to sit on a dense layer on top of the membrane (this dense layer was not observed for the SW furnace). Several spot EDS measurements indicated an approximate composition of $La_{0.05}Sr_{0.95}Co_{0.2}Fe_{0.8}O_3$ for this dense layer. It is conceivable that this dense layer could be responsible for the lower than expected oxygen permeation rates and hydrogen production rates for the LN furnace as compared to the SW furnace.

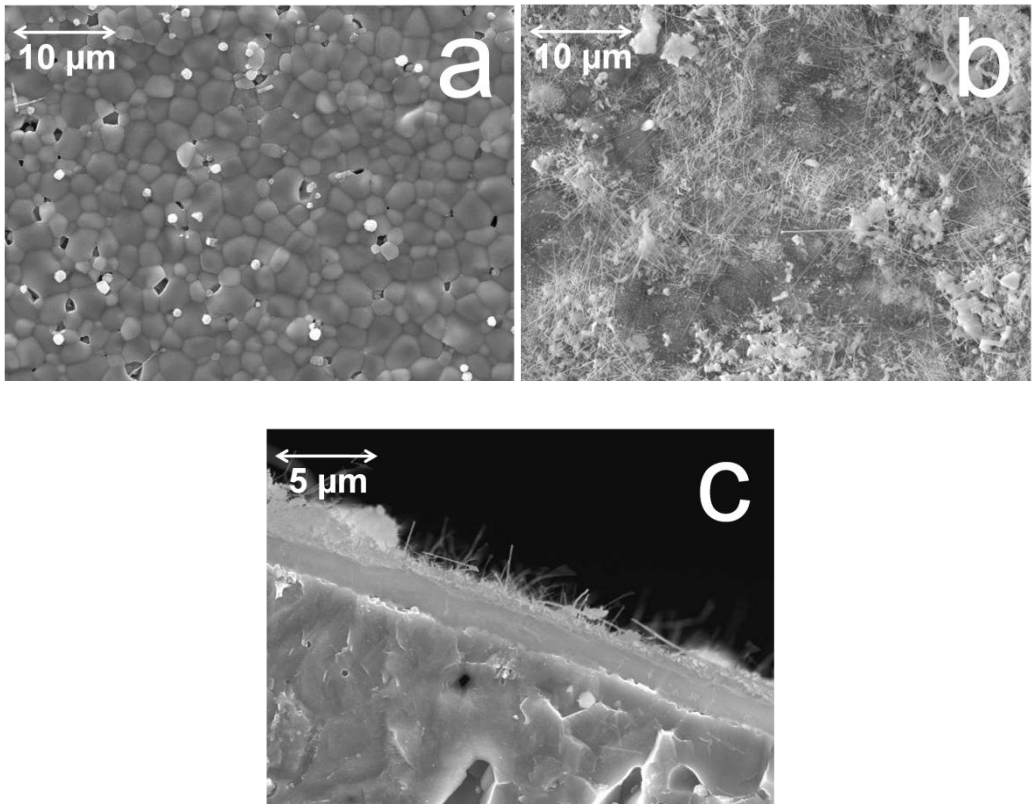

Figure 6.10 Post operation SEM images of the microtubes using the LN furnace: (a) the lumen-side surface of hot zone showing small crystals, (b) the shell-side surface of the hot zone showing needle like crystals and (c) the cross-section showing the shell-side surface of the hot zone covered with a micro-layer.

6.7 Summary

Microtubular membranes have been employed for hydrogen production via steam reforming of methane across oxygen permeable LSCF6428 membranes. A dual gas analysis strategy was undertaken in order to simultaneously monitor the gas outlet composition from both sides of the membrane. This allowed for material balances to be undertaken and confirmed that the production of hydrogen from water splitting was not from transient surface reaction but from steady oxygen permeation as a result of an oxygen vacancy gradient. The role of oxygen permeation was confirmed by interruption of the methane supply. The influence of the axial temperature profile of the furnace was investigated by using two furnaces in order to subject the membranes to two different temperature profiles over a total operation period of *ca* 400 hours of oxygen permeation followed by *ca* 400 hours of steam reforming (the membranes suffered mechanical failure at the end of this period). The two temperature profiles imposed on the membranes gave rise to differences in performance and degradation. While the main perovskite phase is generally maintained, SrO and La_2O_3 segregation were observed at the water vapour exposed membrane surface (shell side) for membranes used in the longer furnace. A strontium rich dense layer on this surface was observed by SEM-EDS and may have reduced the relative permeation rate. This highlights a potential complication due to variable chemistry as a result of differing axial temperature gradients at the inlet and outlet of tubular membrane modules.

Chapter 7

7 Conclusions and suggested future work

7.1 Research outcome

The main objective of this project was to evaluate the feasibility of using microtubular perovskite membranes, as oxygen carrier materials, in membrane-based processes for hydrogen production from water splitting. Membrane-based water splitting investigations was hindered during the '80s due to low capability of the membranes to conduct electrons; however with recent developments in material science engineering and membrane technology new membranes able to overcome this deficit have been designed. Three perovskite $Ba_{0.5}Sr_{0.5}Co_{0.8}Fe_{0.2}O_{3-\delta}$, $La_{0.7}Sr_{0.3}FeO_{3-\delta}$ and $La_{0.6}Sr_{0.4}Co_{0.2}Fe_{0.8}O_{3-\delta}$ were selected in this project as potential candidate for hydrogen production from water splitting due to desirable properties for oxygen permeation when exposed to oxygen partial pressure gradient [6-9].

Preliminary tests with the perovskites in the powder form were carried out; both $La_{0.7}Sr_{0.3}FeO_{3-\delta}$ and $La_{0.6}Sr_{0.4}Co_{0.2}Fe_{0.8}O_{3-\delta}$ generated steady hydrogen production over fifteen temperature programmed oxidation cycles in water and reduction in methane at the temperature of 900°C. $Ba_{0.5}Sr_{0.5}Co_{0.8}Fe_{0.2}O_{3-\delta}$ powder material however presented low hydrogen production activity from water splitting and methane reduction.

Temperature programmed redox cycles were also carried out with dense membrane fragments (*ca* 50mg) of each perovskite; membrane fragments presented much lower hydrogen production activity than the powder material. However it is clear that the surface area of the powder is much higher than dense membrane fragments. $Ba_{0.5}Sr_{0.5}Co_{0.8}Fe_{0.2}O_{3-\delta}$ and $La_{0.7}Sr_{0.3}FeO_{3-\delta}$ membrane fragments presented low activity for water splitting: This was expected to $Ba_{0.5}Sr_{0.5}Co_{0.8}Fe_{0.2}O_{3-\delta}$ as the powder material presented the same behaviour. However $La_{0.7}Sr_{0.3}FeO_{3-\delta}$ membrane fragment low activity was unexpected as its powder material showed good performance for water splitting. Material characterisation showed the presence of an enriched sulfur/strontium layer on the membrane surface and may have reduced the relative permeation rate and consequently hydrogen production. $La_{0.6}Sr_{0.4}Co_{0.2}Fe_{0.8}O_{3-\delta}$ dense membrane fragments

presented an induction period (first five redox cycles) with low hydrogen production from water splitting, after this the hydrogen production had a significant increase indicating that an activation period is necessary for steady hydrogen production. During reoxidation cycles with water, hydrogen and also carbon monoxide and traces of carbon dioxide were produced probably due to water oxidation of deposited carbon generated during the reduction step with methane.

Microtubular membranes of each perovskite were also tested in membrane-based processes, oxygen permeation and membrane-based steam reforming were carried out in order to evaluate the capability to permeate oxygen and produce hydrogen from water dissociation and methane reduction. $Ba_{0.5}Sr_{0.5}Co_{0.8}Fe_{0.2}O_{3-\delta}$ membranes presented high oxygen permeation rates at 900°C (higher than $La_{0.6}Sr_{0.4}Co_{0.2}Fe_{0.8}O_{3-\delta}$ and $La_{0.7}Sr_{0.3}FeO_{3-\delta}$ membranes) however did not present good activation for hydrogen production via membrane-based steam reforming. This indicated that fast oxygen bulk transport is not necessarily the main consideration for hydrogen production and the limiting step can be a surface process. The surface's catalytic capability to split water and activate methane plays an important role in the overall process. $La_{0.7}Sr_{0.3}FeO_{3-\delta}$ membranes did not show oxygen permeation at 900°C nor hydrogen production from water splitting; post operation analysis revealed that a strontium/sulfur layer (previous observed with membrane fragments) affected the membrane's performance. $La_{0.6}Sr_{0.4}Co_{0.2}Fe_{0.8}O_{3-\delta}$ membranes presented moderate oxygen permeation rates and good capability to hydrogen production from membrane based steam reforming. Altering water vapour and methane concentrations it was observed that hydrogen production gradually increased with the increase of methane and water vapour concentration, however surface exchange limitation was observed at the oxidation membrane surface when water vapour concentration was raised above 6%. Also the most suitable conditions (to the experimental setup used in this project) for long term membrane-based steam reforming experiments were determined in these studies; temperature at 900°C, water vapour concentration *ca* 7% and methane concentration at 5%.

Preliminary studies, rarely reported in membrane experiments, were carried out in this project; temperature profiles of both the furnaces (short and long) used in this project were prepared in order to estimate the active effective area of permeation. This is necessary as the total length of the membrane is uncovered due to the cold sealing strategy applied. Residence time distribution analysis was also carried out; it was

observed that the shell side of the membranes performs as a well mixed reactor and the lumen side performs in a plug flow regime when compared to the shell side. A blank membrane-based steam reforming test with alumina tubes (instead membranes) showed that the sealant material could support the experiments conditions. Low water-splitting activity was also observed with the alumina tubes.

As a result of the preliminary tests, the best performing perovskite membrane ($La_{0.6}Sr_{0.4}Co_{0.2}Fe_{0.8}O_{3-\delta}$) for hydrogen production from water splitting was selected for further long term studies. The influence of the axial temperature profile of two different furnaces was investigated in oxygen permeation and membrane-based steam reforming experiments. The membrane reactor used in the short furnace unexpectedly performed better than the membrane reactor in the long furnace. Post operation analysis indicated that the temperature profile imposed from the long furnace gave rise to differences in performance and degradation.

The membrane reactors operated over a total operation period of *ca* 400 hours of oxygen permeation followed by *ca* 400 hours of steam reforming (longest reported duration in water splitting studies). The need for an induction period of *ca* 30 hours in order to establish an oxygen vacancy gradient across the $La_{0.6}Sr_{0.4}Co_{0.2}Fe_{0.8}O_{3-\delta}$ membrane was observed. No water splitting activity or methane products were observed during this induction period. This was possible due to a dual gas analysis strategy in order to simultaneously monitor the gas outlet composition from both sides of the membrane. This also allowed a careful material balance which showed that the oxygen removed from the water dissociation side matches the oxygen permeated to the reaction side. The closure of this material balance is supporting evidence that hydrogen production from water splitting is directly related to the oxygen permeation flux across the membrane rather than surface reactions only.

The role of oxygen permeation was also investigated by interrupting the methane supply at the reaction side of the membranes during membrane-based steam reforming. The hydrogen production level rate rapidly decreased, however not to zero, showing that hydrogen production from water splitting is associated not only to oxygen permeation but also to surface reactions. Reintroduction of methane established the oxygen vacancy gradient and hydrogen was observed at approximately the same level as before interruption. Post-operation analysis indicated that the main perovskite structure of the membranes was maintained; however performance may hindered due to a strontium rich

dense layer observed at the water exposed side for membranes used in the longer furnace. SrO and La_2O_3 segregation combined with SiO_2 contamination, probably from the quartz tube, was also observed.

7.2 Suggested future work

This research project investigated three different membrane perovskites for hydrogen production from water splitting at high temperature. Some future tasks are suggested from the outcome of this research:

- Development of microtubular asymmetric membranes can improve performance; porous substrate combined with thin layers to reduce bulk oxygen diffusion limitations can be used to ensure high oxygen permeation and therefore higher hydrogen production rates.

- Application of catalyst material to improve kinetics *e.g.* nickel based catalyst can be applied to improve methane activation on the reaction side of the membranes.

- Optimisation of hot sealant materials for tubular membranes in order to avoid temperature gradient along the membrane length. This would reduce thermal stress (caused by restricting thermal expansion) as the length can be exposed to an isothermal zone.

- Employment of pulsed isotopic exchange techniques with labelled water ($H_2{}^{18}O$) on membrane samples during high temperature operation to investigate the surface oxygen exchange and bulk oxygen transport.

- Membrane-based steam reforming is an endothermic process; a novel autothermal membrane-based process for hydrogen production from water splitting can be developed if some of the reducing gas is combusted to provide the required heat. This would involve two sets of OTM tubular membranes with fuel (*e.g.* methane) on the shell side and different inlet feeds on the lumen side for each set of membrane; one set with water and the other with air (Figure 7.1). Autothermal operation can be achieved balancing their flow rates and

conversions (*e.g.* with the application of catalyst material to improve kinetics) of each set of membranes.

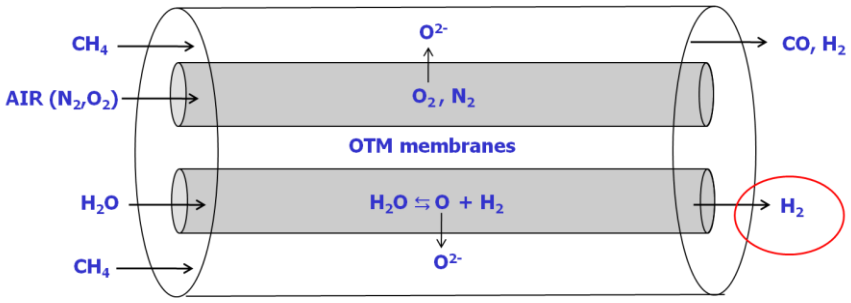

Figure 7.1 Schematic representation of autothermal membrane-based process for hydrogen production. Water splitting is performed in one set of membranes and the other set provides oxygen for methane combustion.

Bibliography

8 References

1. (EIA), U.S.E.I.A., *Annual Energy Outlook 2012 with projections to 2035.* 2012.
2. Carvallo, A. and J. Cooper, *The advanced smart grid : edge power driving sustainability*, Boston: Artech House.
3. (EIA), U.S.E.I.A., *International Energy Outlook 2011*. 2011.
4. Menegaki, A.N., *A social marketing mix for renewable energy in Europe based on consumer stated preference surveys.* Renewable Energy. **39**(1): p. 30-39.
5. Naito, H. and H. Arashi, *Hydrogen production from direct water splitting at high temperatures using a ZrO2-TiO2-Y2O3 membrane.* Solid State Ionics, 1995. **79**: p. 366-370.
6. Tan, X., Y. Liu, and K. Li, *Preparation of LSCF Ceramic Hollow-Fiber Membranes for Oxygen Production by a Phase-Inversion/Sintering Technique.* Industrial & Engineering Chemistry Research, 2004. **44**(1): p. 61-66.
7. Buysse, C., et al., *Fabrication and oxygen permeability of gastight, macrovoid-free Ba0.5Sr0.5Co0.8Fe0.2O3-δ capillaries for high temperature gas separation.* Journal of Membrane Science. **359**(1-2): p. 86-92.
8. Buysse, C., et al., *Development, performance and stability of sulfur-free, macrovoid-free BSCF capillaries for high temperature oxygen separation from air.* Journal of Membrane Science. **372**(1-2): p. 239-248.
9. Tan, X., et al., *La0.7Sr0.3FeO3-δ perovskite hollow fiber membranes for oxygen permeation and methane conversion.* Separation and Purification Technology. **96**(0): p. 89-97.
10. Demirbas, A., *Political, economic and environmental impacts of biofuels: A review.* Applied Energy, 2009. **86, Supplement 1**(0): p. S108-S117.
11. Agency, I.E., *World Energy Outlook 2011*: OECD Publishing.
12. Angency, E.E., *SC Opinion on Greenhouse Gas Accounting in Relation to Bioenergy - 15 September 2011*. 2011.
13. Edwards, P.P., et al., *Hydrogen and fuel cells: Towards a sustainable energy future.* Energy Policy, 2008. **36**(12): p. 4356-4362.
14. Bauen, A., *Future energy sources and systems - Acting on climate change and energy security.* Journal of Power Sources, 2006. **157**(2): p. 893-901.
15. H.A. Meinema, R.W.J.D., H.W. Brinkman, R.A. Terpstra, J. Jekerle, P.H. Kösters, *Ceramic Membranes for Gas Separation – Recent Developments and State of the Art.* Interceram, 2005. **54**.
16. Halloran, J.W., *Extraction of hydrogen from fossil fuels with production of solid carbon materials.* International Journal of Hydrogen Energy, 2008. **33**(9): p. 2218-2224.
17. Adhikari, S. and S. Fernando, *Hydrogen Membrane Separation Techniques.* Industrial & Engineering Chemistry Research, 2006. **45**(3): p. 875-881.
18. Lu, G.Q., et al., *Inorganic membranes for hydrogen production and purification: A critical review and perspective.* Journal of Colloid and Interface Science, 2007. **314**(2): p. 589-603.

19. Bernardo, P., E. Drioli, and G. Golemme, *Membrane Gas Separation: A Review/State of the Art.* Industrial & Engineering Chemistry Research, 2009. **48**(10): p. 4638-4663.
20. Gallucci, F., et al., *A Review on Patents for Hydrogen Production Using Membrane Reactors.* Recent patents on chemical engineering, 2009. **2**(3): p. 207-222.
21. Yaremchenko, A.A., et al., *Stability, oxygen permeability and chemical expansion of Sr(Fe,Al)O3-δ and Sr(Co,Fe)O3-δ based membranes.* Solid State Ionics. **192**(1): p. 259-268.
22. Agency, I.E., *Hydrogen Production and Storage* 2006.
23. Balat, M., *Potential importance of hydrogen as a future solution to environmental and transportation problems.* International Journal of Hydrogen Energy, 2008. **33**(15): p. 4013-4029.
24. Baykara, S.Z., *Hydrogen as fuel: a critical technology?* International Journal of Hydrogen Energy, 2005. **30**(5): p. 545-553.
25. Gaudernack, B.r. and S. Lynum, *Hydrogen from natural gas without release of CO2 to the atmosphere.* International Journal of Hydrogen Energy, 1998. **23**(12): p. 1087-1093.
26. Boyano, A., et al., *Exergoenvironmental analysis of a steam methane reforming process for hydrogen production.* Energy. **36**(4): p. 2202-2214.
27. Stocker, J.W., M.; Miller, G.Q>, *30 years of PSA technology for hydrogen purification.* 2005.
28. Sharma, S.D., *FUELS - HYDROGEN PRODUCTION | Gas Cleaning: Pressure Swing Adsorption*, in *Encyclopedia of Electrochemical Power Sources*. 2009, Elsevier: Amsterdam. p. 335-349.
29. Tugnoli, A., G. Landucci, and V. Cozzani, *Sustainability assessment of hydrogen production by steam reforming.* International Journal of Hydrogen Energy, 2008. **33**(16): p. 4345-4357.
30. Babita, K., S. Sridhar, and K.V. Raghavan, *Membrane reactors for fuel cell quality hydrogen through WGSR - Review of their status, challenges and opportunities.* International Journal of Hydrogen Energy. **36**(11): p. 6671-6688.
31. Ursua, A., L.M. Gandia, and P. Sanchis, *Hydrogen Production From Water Electrolysis: Current Status and Future Trends.* Proceedings of the IEEE, 2012. **100**(2): p. 410-42.
32. Zeng, K. and D. Zhang, *Recent progress in alkaline water electrolysis for hydrogen production and applications.* Progress in Energy and Combustion Science. **36**(3): p. 307-326.
33. Barbir, F., *PEM electrolysis for production of hydrogen from renewable energy sources.* Solar Energy, 2005. **78**(5): p. 661-669.
34. Shafiee, S. and E. Topal, *A long-term view of worldwide fossil fuel prices.* Applied Energy. **87**(3): p. 988-1000.
35. E. Funk, J., *Thermochemical hydrogen production: past and present.* International Journal of Hydrogen Energy, 2001. **26**(3): p. 185-190.
36. Baykara, S.Z., *Hydrogen production by direct solar thermal decomposition of water, possibilities for improvement of process efficiency.* International Journal of Hydrogen Energy, 2004. **29**(14): p. 1451-1458.
37. Aroutiounian, V.M., V.M. Arakelyan, and G.E. Shahnazaryan, *Metal oxide photoelectrodes for hydrogen generation using solar radiation-driven water splitting.* Solar Energy, 2005. **78**(5): p. 581-592.
38. Kasem, K.K.D., Melissa; Zia, Nida; Finney, Aubrey, *Photoelectrochemical Production of Hydrogen in Aqueous Suspensions Nanoparticles Composites of CdS/ZnS.* Materials Sciences & Applications;, 2011. **2**(11): p. 1631.

39. Ni, M., et al., *A review and recent developments in photocatalytic water-splitting using for hydrogen production.* Renewable and Sustainable Energy Reviews, 2007. **11**(3): p. 401-425.
40. Das, D. and T.N. Veziroglu, *Hydrogen production by biological processes: a survey of literature.* International Journal of Hydrogen Energy, 2001. **26**(1): p. 13-28.
41. Levin, D.B., L. Pitt, and M. Love, *Biohydrogen production: prospects and limitations to practical application.* International Journal of Hydrogen Energy, 2004. **29**(2): p. 173-185.
42. Holladay, J.D., et al., *An overview of hydrogen production technologies.* Catalysis Today, 2009. **139**(4): p. 244-260.
43. Qinglan, H., et al., *Production of hydrogen-rich gas from plant biomass by catalytic pyrolysis at low temperature.* International Journal of Hydrogen Energy. **35**(17): p. 8884-8890.
44. Milne, T.A., C.C. Elam, and R.J. Evans, *Hydrogen from biomass: state of the art and research challenges*, in *Other Information: PBD: 1 Feb 2002*. 2002. p. Medium: ED; Size: 82 pages.
45. Tanksale, A., J.N. Beltramini, and G.M. Lu, *A review of catalytic hydrogen production processes from biomass.* Renewable and Sustainable Energy Reviews. **14**(1): p. 166-182.
46. Kruse, A., *Supercritical water gasification.* Biofuels, Bioproducts and Biorefining, 2008. **2**(5): p. 415-437.
47. Ni, M., et al., *An overview of hydrogen production from biomass.* Fuel Processing Technology, 2006. **87**(5): p. 461-472.
48. Kalinci, Y., A. Hepbasli, and I. Dincer, *Biomass-based hydrogen production: A review and analysis.* International Journal of Hydrogen Energy, 2009. **34**(21): p. 8799-8817.
49. Makaruk, A., M. Miltner, and M. Harasek, *Membrane gas permeation in the upgrading of renewable hydrogen from biomass steam gasification gases.* Applied Thermal Engineering. **43**(0): p. 134-140.
50. Favre, E., *Pioneers in membrane transport: Graham, von Wroblewski â€¦ and Lhermite.* Journal of Membrane Science, 2004. **229**(1-2): p. 241-242.
51. R. D. NOBLE, S.A.S., *Membrane Separations Technology - Principles and Applications. Elsevier, Amsterdam 1995. –.* 1996.
52. Habert, A.C.B.C.P.N.R., *Processos de separação com membranas- epapers*, ed. E.p.d.e. Química. 2006, Rio de Janeiro: COPPE/UFRJ.
53. Mulder, M., *Basic Principles of Membranes technology*. 2 ed. 1996: Springer-Verlag New York, LLC.
54. **S.C.A.Kluiters**, *Status review on membrane systems for hydrogen separation.* ECN publication 2004.
55. Abedini, R. and A. Nezhadmoghadam, *APPLICATION OF MEMBRANE IN GAS SEPARATION PROCESSES: ITS SUITABILITY AND MECHANISMS.* Petroleum and Coal 2010. **52**(2).
56. Baker, R.W., *Future Directions of Membrane Gas Separation Technology.* Industrial & Engineering Chemistry Research, 2002. **41**(6): p. 1393-1411.
57. Freeman Benny, D. and I. Pinnau, *Gas and Liquid Separations Using Membranes: An Overview*, in *Advanced Materials for Membrane Separations*. 2004, American Chemical Society. p. 1-23.
58. Baker, R.W., *Membrane Technology and Applications*. 2 edition ed. 2004, Chichester: John Wiley & Sons.

59. Paglieri, S.N. and J.D. Way, *INNOVATIONS IN PALLADIUM MEMBRANE RESEARCH.* Separation & Purification Reviews, 2002. **31**(1): p. 1-169.
60. Xomeritakis, G. and Y.S. Lin, *Fabrication of a thin palladium membrane supported in a porous ceramic substrate by chemical vapor deposition.* Journal of Membrane Science, 1996. **120**(2): p. 261-272.
61. Cheng, Y.S. and K.L. Yeung, *Palladium-silver composite membranes by electroless plating technique.* Journal of Membrane Science, 1999. **158**(1-2): p. 127-141.
62. Yun, S. and S. Ted Oyama, *Correlations in palladium membranes for hydrogen separation: A review.* Journal of Membrane Science. **375**(1-2): p. 28-45.
63. Ismail, A.F. and L.I.B. David, *A review on the latest development of carbon membranes for gas separation.* Journal of Membrane Science, 2001. **193**(1): p. 1-18.
64. Baker, R.W. and e. al, *Membrane Separation Systems - Recent Developments and Future Directions*. 1991, William Andrew Publishing/Noyes.
65. Lin, Y.S., *Microporous and dense inorganic membranes: current status and prospective.* Separation and Purification Technology, 2001. **25**(1-3): p. 39-55.
66. Dong, X., et al., *Dense ceramic catalytic membranes and membrane reactors for energy and environmental applications.* Chemical Communications. **47**(39): p. 10886-10902.
67. Dyer, P.N., et al., *Ion transport membrane technology for oxygen separation and syngas production.* Solid State Ionics, 2000. **134**(1-2): p. 21-33.
68. Knauth, P. and H.L. Tuller, *Solid-State Ionics: Roots, Status, and Future Prospects.* Journal of the American Ceramic Society, 2002. **85**(7): p. 1654-1680.
69. Akin, F.T. and J.Y.S. Lin, *Oxygen permeation through oxygen ionic or mixed-conducting ceramic membranes with chemical reactions.* Journal of Membrane Science, 2004. **231**(1-2): p. 133-146.
70. Teraoka, Y., et al., *Mixed ionic-electronic conductivity of La1-xSrxCo1-yFeyO3-δ perovskite-type oxides.* Materials Research Bulletin, 1988. **23**(1): p. 51-58.
71. Teraoka, Y., et al., *Oxygen permeation through Perovskite-type oxides.* Chemistry Letters, 1985(11): p. 1743-1746.
72. Kharton, V.V., et al., *Perovskite-type oxides for high-temperature oxygen separation membranes.* Journal of Membrane Science, 1999. **163**(2): p. 307-317.
73. Sunarso, J., et al., *Mixed ionic-electronic conducting (MIEC) ceramic-based membranes for oxygen separation.* Journal of Membrane Science, 2008. **320**(1-2): p. 13-41.
74. Carter, S., et al., *Oxygen transport in selected nonstoichiometric perovskite-structure oxides.* Solid State Ionics, 1992. **53-56, Part 1**(0): p. 597-605.
75. Li, K. *Ceramic membranes for separation and reaction*. 2007; Available from: http://books.google.com/books?id=vsVTAAAAMAAJ.
76. Virkar, A.V., *Theoretical analysis of the role of interfaces in transport through oxygen ion and electron conducting membranes.* Journal of Power Sources, 2005. **147**(1-2): p. 8-31.
77. Zhu, X., et al., *Permeation model and experimental investigation of mixed conducting membranes.* AIChE Journal. **58**(6): p. 1744-1754.
78. Gellings, P.J. and H.J.M. Bouwmeester, *The CRC Handbook of Solid State Electrochemistry*. 1997: CRC Press.
79. Wagner, C., *Equations for transport in solid oxides and sulfides of transition metals.* Progress in Solid State Chemistry, 1975. **10, Part 1**(0): p. 3-16.
80. Bouwmeester, H.J.M., H. Kruidhof, and A.J. Burggraaf, *Importance of the surface exchange kinetics as rate limiting step in oxygen permeation through mixed-conducting oxides.* Solid State Ionics, 1994. **72, Part 2**(0): p. 185-194.

81. Julbe, A., D. Farrusseng, and C. Guizard, *Porous ceramic membranes for catalytic reactors â€" overview and new ideas.* Journal of Membrane Science, 2001. **181**(1): p. 3-20.
82. Liu, S., et al., *Preparation and characterisation of SrCe0.95Yb0.05O2.975 hollow fibre membranes.* Journal of Membrane Science, 2001. **193**(2): p. 249-260.
83. Thursfield, A. and I. Metcalfe, *Methane oxidation in a mixed ionic–electronic conducting ceramic hollow fibre reactor module.* Journal of Solid State Electrochemistry, 2006. **10**(8): p. 604-616.
84. Venkatesh, R. and S.R. Ramanan, *Influence of processing variables on the microstructure of sol-gel spun alumina fibres.* Materials Letters, 2002. **55**(3): p. 189-195.
85. Zydorczak, B., Z. Wu, and K. Li, *Fabrication of ultrathin La0.6Sr0.4Co0.2Fe0.8O3-δ hollow fibre membranes for oxygen permeation.* Chemical Engineering Science, 2009. **64**(21): p. 4383-4388.
86. Zivkovic, T., N.E. Benes, and H.J.M. Bouwmeester, *Gas transport efficiency of ceramic membranes: comparison of different geometries.* Journal of Membrane Science, 2004. **236**(1-2): p. 101-108.
87. Burggraaf, A.J., et al., *Fundamentals of inorganic membrane science and technology*, in *Membrane Science and Technology*. 1996, Elsevier. p. iii.
88. Liang, F., et al., *High-purity oxygen production by a dead-end Ba0.5Sr0.5Co0.8Fe0.2O3-δ tube membrane.* Catalysis Today. **193**(1): p. 95-100.
89. Wang, H., et al., *Production of high-purity oxygen by perovskite hollow fiber membranes swept with steam.* Journal of Membrane Science, 2006. **284**(1-2): p. 5-8.
90. Elshof ten, J.E., H.J.M. Bouwmeester, and H. Verweij, *Oxidative coupling of methane in a mixed-conducting perovskite membrane reactor.* Applied Catalysis A: General, 1995. **130**(2): p. 195-212.
91. Zeng, Y. and Y.S. Lin, *Oxygen Permeation and Oxidative Coupling of Methane in Yttria Doped Bismuth Oxide Membrane Reactor.* Journal of Catalysis, 2000. **193**(1): p. 58-64.
92. Lu, Y., et al., *Oxygen-permeable dense membrane reactor for the oxidative coupling of methane.* Journal of Membrane Science, 2000. **170**(1): p. 27-34.
93. Koros, W.J. and R. Mahajan, *Pushing the limits on possibilities for large scale gas separation: which strategies?* Journal of Membrane Science, 2001. **181**(1): p. 141.
94. Bouwmeester, H.J.M., *Dense ceramic membranes for methane conversion.* Catalysis Today, 2003. **82**(1-4): p. 141-150.
95. Liu, H., et al., *Enhanced oxygen permeation through perovskite hollow fibre membranes by methane activation.* Ceramics International, 2009. **35**(4): p. 1435-1439.
96. Hendriksen, P.V., et al., *Prospects and problems of dense oxygen permeable membranes.* Catalysis Today, 2000. **56**(1-3): p. 283-295.
97. Pei, S., et al., *Failure mechanisms of ceramic membrane reactors in partial oxidation of methane to synthesis gas.* Catalysis Letters, 1994. **30**(1): p. 201-212.
98. Tan, X., Z. Pang, and K. Li, *Oxygen production using La0.6Sr0.4Co0.2Fe0.8O3-α (LSCF) perovskite hollow fibre membrane modules.* Journal of Membrane Science, 2008. **310**(1-2): p. 550-556.
99. Li, S., et al., *Tubular lanthanum cobaltite perovskite type membrane for oxygen permeation.* Journal of Membrane Science, 2000. **166**(1): p. 51-61.

100. Tan, X., et al., *Oxygen permeation behavior of La0.6Sr0.4Co0.8Fe0.2O3 hollow fibre membranes with highly concentrated CO2 exposure.* Journal of Membrane Science. **389**(0): p. 216-222.
101. Elshof ten, J.E., H.J.M. Bouwmeester, and H. Verweij, *Oxygen transport through La1 − xSrxFeO3 − δ membranes II. Permeation in air/CO, CO2 gradients.* Solid State Ionics, 1996. **89**(1-2): p. 81-92.
102. Hatcher, J., et al., *Development and testing of an intermediate temperature glass sealant for use in mixed ionic and electronic conducting membrane reactors.* Solid State Ionics. **181**(15-16): p. 767-774.
103. Dong, X., et al., *Dense ceramic catalytic membranes and membrane reactors for energy and environmental applications.* Chemical Communications, 2011. **47**(39): p. 10886-10902.
104. Liu, Y., X. Tan, and K. Li, *Mixed Conducting Ceramics for Catalytic Membrane Processing.* Catalysis Reviews, 2006. **48**(2): p. 145-198.
105. Yang, W., et al., *Development and Application of Oxygen Permeable Membrane in Selective Oxidation of Light Alkanes.* Topics in Catalysis, 2005. **35**(1): p. 155-167.
106. Caro, J., *Membranreaktoren für die katalytische Oxidation.* Chemie Ingenieur Technik, 2006. **78**(7): p. 899-912.
107. Usachev, N.Y., et al., *Conversion of hydrocarbons to synthesis gas: Problems and prospects.* Petroleum Chemistry, 2011. **51**(2): p. 96-106.
108. Jiang, Q., et al., *A Review of Mixed Ionic and Electronic Conducting Ceramic Membranes as Oxygen Sources for High Temperature Reactors*, in *Membrane Science and Technology*. 2011. p. 235-273.
109. Thursfield, A., et al., *Chemical looping and oxygen permeable ceramic membranes for hydrogen production - a review.* Energy & Environmental Science. **5**(6): p. 7421-7459.
110. Lu, H., et al., *Partial oxidation of methane in Ba0.5Sr0.5Co0.8Fe0.2O3-[delta] membrane reactor at high pressures.* Catalysis Today, 2005. **104**(2-4): p. 154-159.
111. Shen, Z., et al., *Performance of Ba0.5Sr0.5Co0.8Fe0.2O3 + [delta] membrane after laser ablation for methane conversion.* Catalysis Communications, 2010. **11**(10): p. 892-895.
112. Wang, H., et al., *Partial oxidation of methane to syngas in a perovskite hollow fiber membrane reactor.* Catalysis Communications, 2006. **7**(11): p. 907-912.
113. Kondratenko, E.V., et al., *Selective oxidation of CH4 and C2H6 over a mixed oxygen ion and electron conducting perovskite--A TAP and membrane reactors study.* Journal of Molecular Catalysis A: Chemical, 2009. **297**(2): p. 142-149.
114. Luo, H.X., et al., *Novel Ba0.5Sr0.5Fe0.8Zn0.2O3-[delta] membranes for POM.* Chinese Chemical Letters, 2009. **20**(2): p. 250-252.
115. Luo, H.X., et al., *Performance of a ceramic membrane reactor with high oxygen flux Ta-containing perovskite for the partial oxidation of methane to syngas.* Journal of Membrane Science, 2010. **350**(1-2): p. 154-160.
116. Caro, J., et al., *Perovskite hollow fibre membranes in the partial oxidation of methane to synthesis gas in a membrane reactor.* Desalination, 2006. **199**(1-3): p. 415-417.
117. Kleinert, A., et al., *Novel hollow fibre membrane reactor for the partial oxidation of methane.* Catalysis Today, 2006. **118**(1-2): p. 44-51.
118. Gong, Z. and L. Hong, *Integration of air separation and partial oxidation of methane in the La0.4Ba0.6Fe0.8Zn0.2O3-[delta] membrane reactor.* Journal of Membrane Science, 2011. **380**(1-2): p. 81-86.

119. Kawahara, A., et al., *High Oxygen Permeation Rate in La0.6Sr0.4Ti0.3Fe0.7O3 Thin Membrane on a Porous Support with Multichannel Structure for CH4 Partial Oxidation.* Industrial & Engineering Chemistry Research, 2010. **49**(12): p. 5511-5516.
120. Kawahara, A., et al., *Importance of pore structure control in porous substrate for high oxygen penetration in La0.6Sr0.4Ti0.3Fe0.7O3 thin film for CH4 partial oxidation.* Solid State Ionics, 2011. **190**(1): p. 53-59.
121. Chang, X., et al., *A Comparative Study of the Performance of Symmetric and Asymmetric Mixed-conducting Membranes.* Chinese Journal of Chemical Engineering, 2009. **17**(4): p. 562-570.
122. Tan, X., Y. Liu, and K. Li, *Mixed conducting ceramic hollow-fiber membranes for air separation.* AIChE Journal, 2005. **51**(7): p. 1991-2000.
123. Shao, Z., et al., *Investigation of the permeation behavior and stability of a Ba0.5Sr0.5Co0.8Fe0.2O3âˆ'Î´ oxygen membrane.* Journal of Membrane Science, 2000. **172**(1â€“2): p. 177-188.
124. Wang, H., Y. Cong, and W. Yang, *Oxygen permeation study in a tubular Ba0.5Sr0.5Co0.8Fe0.2O3-Î´ oxygen permeable membrane.* Journal of Membrane Science, 2002. **210**(2): p. 259-271.
125. Wang, H., Y. Cong, and W. Yang, *Oxidative coupling of methane in Ba0.5Sr0.5Co0.8Fe0.2O3âˆ'Î´ tubular membrane reactors.* Catalysis Today, 2005. **104**(2â€“4): p. 160-167.
126. Xu, S.J. and W.J. Thomson, *Stability of La0.6Sr0.4Co0.2Fe0.8O3-delta perovskite membranes in reducing and nonreducing environments.* Industrial & Engineering Chemistry Research, 1998. **37**(4): p. 1290-1299.
127. Jin, W., et al., *Tubular lanthanum cobaltite perovskite-type membrane reactors for partial oxidation of methane to syngas.* Journal of Membrane Science, 2000. **166**(1): p. 13-22.
128. Zhu, W., et al., *Mixed reforming of heptane to syngas in the Ba0.5Sr0.5Co0.8Fe0.2O3 membrane reactor.* Catalysis Today, 2005. **104**(2-4): p. 149-153.
129. Löfberg, A., et al., *Selective oxidation of hydrocarbons in a catalytic dense membrane reactor: Catalytic properties of BIMEVOX (Me = Ta).* Catalysis Today, 2006. **118**(1-2): p. 223-227.
130. Löfberg, A., et al., *Transient behaviour of dense catalytic membranes based on Cu- and Co-doped Bi4V2O11 (BIMEVOX) in the oxidation of propene and propane.* Catalysis Today, 2006. **112**(1-4): p. 8-11.
131. Cheng, H., et al., *Hydrogen Production from Simulated Hot Coke Oven Gas by Using Oxygen-Permeable Ceramics.* Energy & Fuels, 2009. **23**(1): p. 414-421.
132. Yang, Z., et al., *Catalytic partial oxidation of coke oven gas to syngas in an oxygen permeation membrane reactor combined with NiO/MgO catalyst.* International Journal of Hydrogen Energy, 2010. **35**(12): p. 6239-6247.
133. Zhang, Y., et al., *Performance of an oxygen-permeable membrane reactor for partial oxidation of methane in coke oven gas to syngas.* Fuel, 2011. **90**(1): p. 324-330.
134. Cales, B. and J.F. Baumard, *Oxygen semipermeability and electronic conductivity in calcia-stabilized zirconia.* Journal of Materials Science, 1982. **17**(11): p. 3243-3248.
135. Lede, J., et al., *Production of hydrogen by direct thermal decomposition of water: Preliminary investigations.* International Journal of Hydrogen Energy, 1982. **7**(12): p. 939-950.

136. Balachandran, U., et al., *Use of mixed conducting membranes to produce hydrogen by water dissociation.* International Journal of Hydrogen Energy, 2004. **29**(3): p. 291-296.
137. Balachandran, U., T.H. Lee, and S.E. Dorris, *Hydrogen production by water dissociation using mixed conducting dense ceramic membranes.* International Journal of Hydrogen Energy, 2007. **32**(4): p. 451-456.
138. Jiang, H., et al., *Simultaneous production of hydrogen and synthesis gas by combining water splitting with partial oxidation of methane in a hollow-fiber membrane reactor.* Angewandte Chemie - International Edition, 2008. **47**(48): p. 9341-9344.
139. Jiang, H., et al., *Hydrogen production by water dissociation in surface-modified BaCoxFeyZr1-x-yO3-δ hollow-fiber membrane reactor with improved oxygen permeation.* Chemistry - A European Journal, 2010. **16**(26): p. 7898-7903.
140. Jiang, H., et al., *A Coupling Strategy to Produce Hydrogen and Ethylene in a Membrane Reactor.* Angewandte Chemie International Edition, 2010. **49**(33): p. 5656-5660.
141. Jiang, H., et al., *Improved water dissociation and nitrous oxide decomposition by in situ oxygen removal in perovskite catalytic membrane reactor.* Catalysis Today, 2010. **156**(3-4): p. 187-190.
142. Evdou, A., L. Nalbandian, and V.T. Zaspalis, *Perovskite membrane reactor for continuous and isothermal redox hydrogen production from the dissociation of water.* Journal of Membrane Science, 2008. **325**(2): p. 704-711.
143. Nalbandian, L., A. Evdou, and V. Zaspalis, *La1-xSrxMO3 (M = Mn, Fe) perovskites as materials for thermochemical hydrogen production in conventional and membrane reactors.* International Journal of Hydrogen Energy, 2009. **34**(17): p. 7162-7172.
144. Park, C.Y., et al., *La0.7Sr0.3Cu0.2Fe0.8O3-x as Oxygen Transport Membrane for Producing Hydrogen via Water Splitting.* ECS Transactions, 2008. **13**(26): p. 393-403.
145. Park, C.Y., et al., *Hydrogen production from fossil and renewable sources using an oxygen transport membrane.* International Journal of Hydrogen Energy, 2010. **35**(9): p. 4103-4110.
146. Park, C.Y., et al., *Oxygen permeation and coal-gas-assisted hydrogen production using oxygen transport membranes.* International Journal of Hydrogen Energy, 2011. **36**(15): p. 9345-9354.
147. Lee, T.H., et al., *Hydrogen Production by Steam Dissociation using Oxygen Transport Membranes.* ECS Transactions, 2008. **13**(26): p. 379-384.
148. Kang, K.-S., et al., *Reduction characteristics of CuFe2O4 and Fe3O4 by methane; CuFe2O4 as an oxidant for two-step thermochemical methane reforming.* International Journal of Hydrogen Energy, 2008. **33**(17): p. 4560-4568.
149. Kang, K.-S., et al., *Oxygen-carrier selection and thermal analysis of the chemical-looping process for hydrogen production.* International Journal of Hydrogen Energy, 2010. **35**(22): p. 12246-12254.
150. Shen, P., et al., *Reaction mechanism on reduction surface of mixed conductor membrane for H2 production by coal-gas.* Applied Surface Science, 2010. **256**(16): p. 5094-5101.
151. Deshmukh, S.P. and K. Li, *Effect of ethanol composition in water coagulation bath on morphology of PVDF hollow fibre membranes.* Journal of Membrane Science, 1998. **150**(1): p. 75-85.
152. Arul, M., T. Alan, and I.S. Metcalfe, *A chemical looping process for hydrogen production using iron-containing perovskites.* **4**(11): p. 4639-4639.

153. Thursfield, A. and I.S. Metcalfe, *Air separation using a catalytically modified mixed conducting ceramic hollow fibre membrane module.* Journal of Membrane Science, 2007. **288**(1-2): p. 175-187.
154. Fowlis, I.A., *Gas chromatography : analytical chemistry by open learning*. 2nd ed. ed. 1995, Chichester ;: Published on behalf of ACOL (University of Greenwich) by Wiley.
155. Minter, C.C., *Thermal conductivity of binary mixtures of gases. I. Hydrogen-helium mixtures.* The Journal of Physical Chemistry, 1968. **72**(6): p. 1924-1926.
156. Ullmann, H., et al., *Correlation between thermal expansion and oxide ion transport in mixed conducting perovskite-type oxides for SOFC cathodes.* Solid State Ionics, 2000. **138**(1-2): p. 79-90.
157. Zeng, P., et al., *Re-evaluation of Ba0.5Sr0.5Co0.8Fe0.2O3-δ perovskite as oxygen semi-permeable membrane.* Journal of Membrane Science, 2007. **291**(1-2): p. 148-156.
158. Levenspiel, O., *Chemical Reaction Engineering (3rd Edition)*, John Wiley & Sons.
159. Yang, J.Y., C. Nishimura, and M. Komaki, *Preparation and characterization of Pd-Cu/V-15Ni composite membrane for hydrogen permeation.* Journal of Alloys and Compounds, 2007. **431**(1-2): p. 180-184.
160. Yacou, C., et al., *Palladium surface modified La0.6Sr0.4Co0.2Fe0.8O3â˜'Î΄ hollow fibres for oxygen separation.* Journal of Membrane Science. **380**(1â€“2): p. 223-231.
161. Liu, S., et al., *Ba0.5Sr0.5Co0.8Fe0.2O3-δ ceramic hollow-fiber membranes for oxygen permeation.* AIChE Journal, 2006. **52**(10): p. 3452-3461.
162. Liu, S. and G.R. Gavalas, *Preparation of Oxygen Ion Conducting Ceramic Hollow-Fiber Membranes.* Industrial & Engineering Chemistry Research, 2005. **44**(20): p. 7633-7637.
163. Wang, H., et al., *Mixed oxygen ion and electron conducting hollow fiber membranes for oxygen separation.* Solid State Ionics, 2006. **177**(26-32): p. 2255-2259.
164. Leo, A., S. Liu, and J.o.C. Diniz da Costa, *Production of pure oxygen from BSCF hollow fiber membranes using steam sweep.* Separation and Purification Technology. **78**(2): p. 220-227.
165. Wang, H., Y. Cong, and W. Yang, *Investigation on the partial oxidation of methane to syngas in a tubular Ba0.5Sr0.5Co0.8Fe0.2O3-δ membrane reactor.* Catalysis Today, 2003. **82**(1-4): p. 157-166.
166. Cao, Z., et al., *Simultaneous overcome of the equilibrium limitations in BSCF oxygen-permeable membrane reactors: Water splitting and methane coupling.* Catalysis Today. **193**(1): p. 2-7.
167. Franca, R.V., A. Thursfield, and I.S. Metcalfe, *La0.6Sr0.4Co0.2Fe0.8O3-δ microtubular membranes for hydrogen production from water splitting.* Journal of Membrane Science. **389**(0): p. 173-181.
168. Jiang, H., et al., *Hydrogen production by water dissociation in surface-modified $BaCo_xFe_yZr_{1-x-y}O_{3-\delta}$ hollow-fiber membrane reactor with improved oxygen permeation.* Chemistry - A European Journal, 2010. **16**(26): p. 7898-7903.
169. Jiang, H., et al., *Improved water dissociation and nitrous oxide decomposition by in situ oxygen removal in perovskite catalytic membrane reactor.* Catalysis Today, 2010. **156**: p. 187-190.
170. Möbius, A., D. Henriques, and T. Markus, *Sintering behaviour of La1-xSrxCo0.2Fe0.8O3-δ (0.3≤x≤0.8) mixed conducting materials* Journal of the European Ceramic Society, 2009. **29**(13): p. 2831-2839.

171. York, A.P.E., T. Xiao, and M.L.H. Green, *Brief Overview of the Partial Oxidation of Methane to Synthesis Gas.* Topics in Catalysis, 2003. **22**(3): p. 345-358.

Appendix

9 Appendix 3-A

Experimental apparatus showing feed system, flow meters, furnace and membrane module.

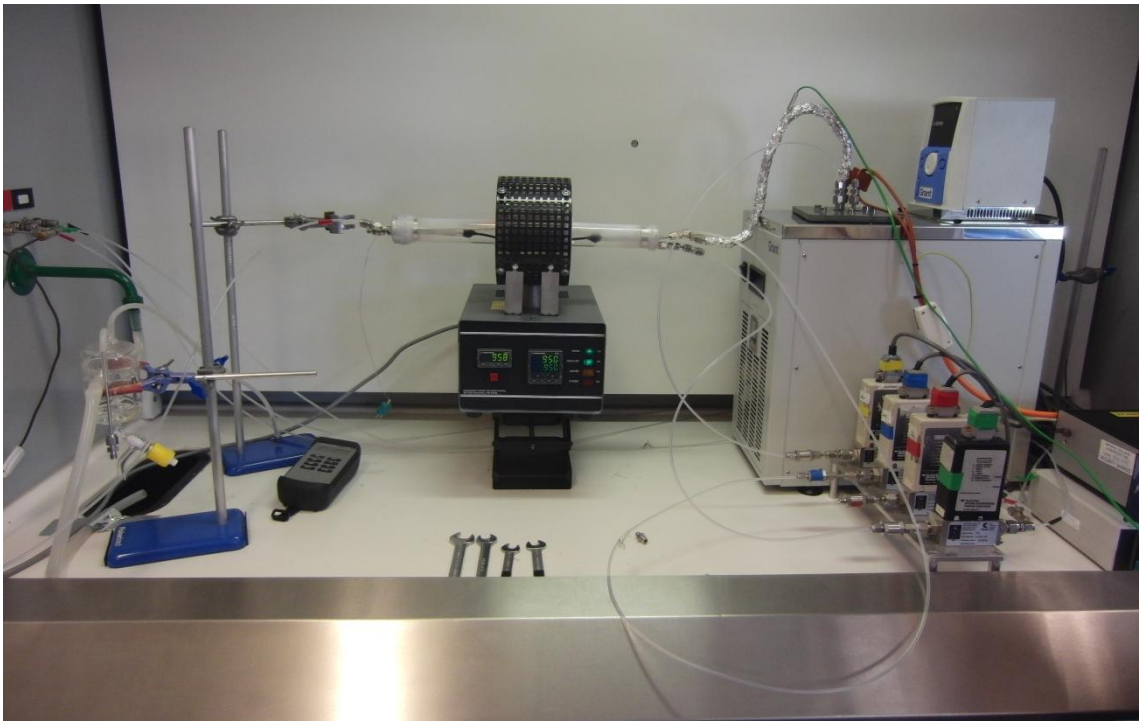

Figure 9.1 Experimental setup used in this project.

10 Appendix 3-B

Results from water saturator calibration using hygrometer.

Table 10.1 Results for water saturator calibration.

Water bath T (°C)	**Thermocouple T inside water bath (°C)**	**Dew point hygrometer (°C)**	**Vapour pressure hygrometer (hpa)**	**Concentration (%)**
11	11	8.5	11.1	1.11
20	20	18.9	21.8	2.18
30	30	28.3	38.6	3.86
35	34	32.3	48.3	4.83
40	40	36.7	61.8	6.18
50	49	48.0	110.0	11.0
60	60	56.6	170.5	17.05

11 Appendix 3-C

Membrane module before sealed showing MACOR tubes, silicone rubber, shell glass and end-caps.

Figure 11.1 Membrane module before sealed.

12 Appendix 5-A

Powder materials

Analysis from the 1st to 15th TPR and TPO cycles of (a) and (b) BSCF5582; (c) and (d) LSCF6428 and (e) and (f) LSF731 (b) powder materials at 900°C.

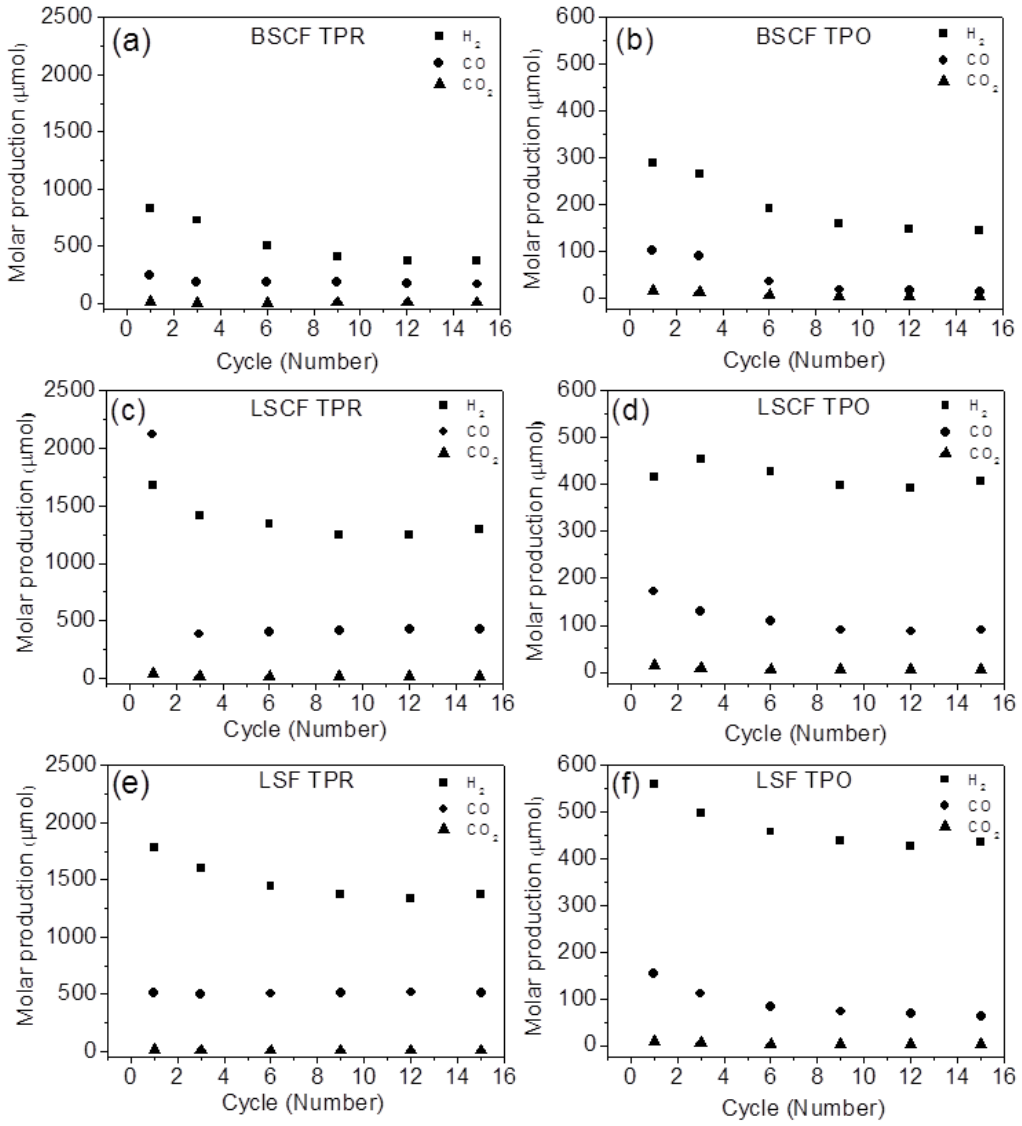

Figure 12.1 Products of TPR/TPO at 900°C during 15 cycles for powder materials. (a) and (b) BSCF5582; (c) and (d) LSCF6428 and (e) and (f) LSF731.

Membranes fragments

Analysis from the 1st to 15th TPR and TPO cycles of (a) and (b) BSCF5582; (c) and (d) LSCF6428 and (e) and (f) LSF731 membranes fragments at 900°C.

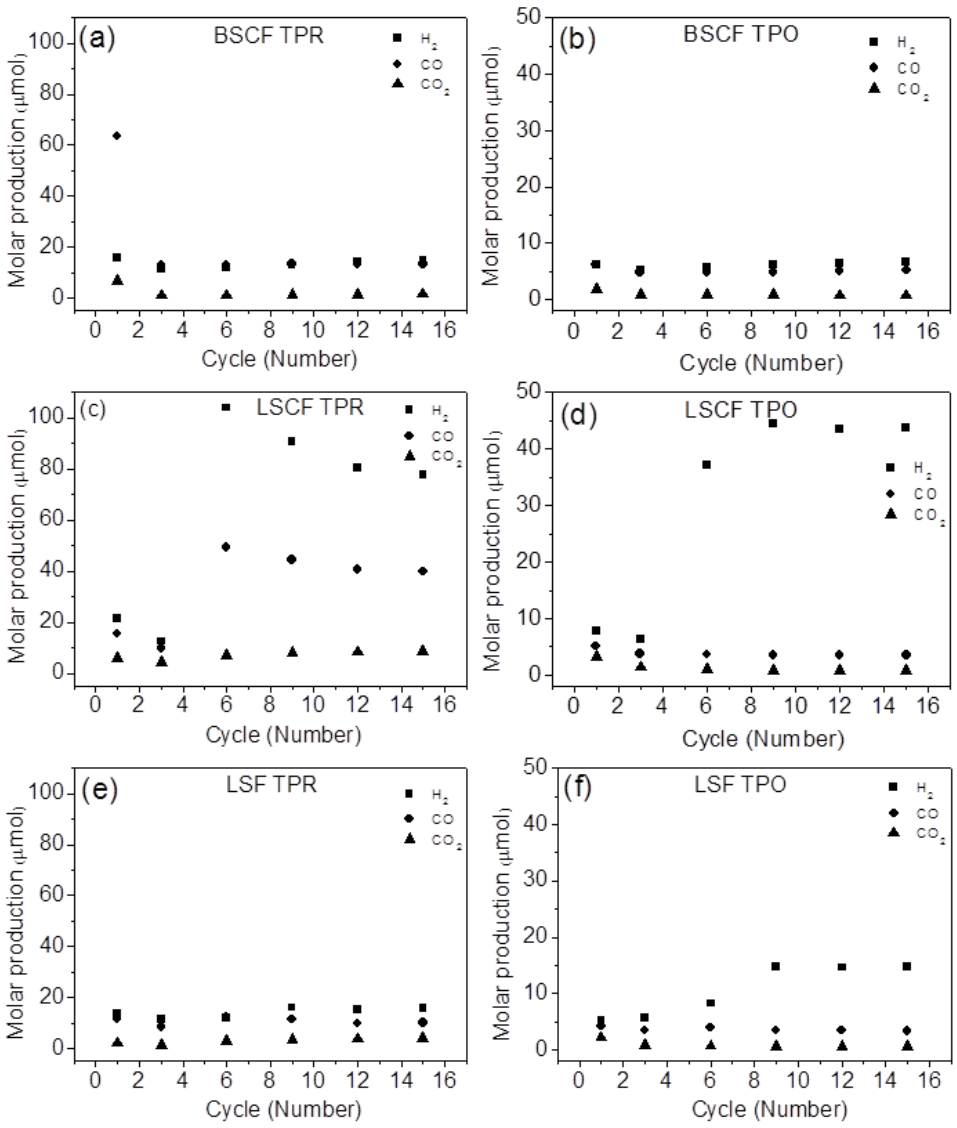

Figure 12.2 Products of TPR/TPO at 900°C during 15 cycles for membranes fragments. (a) and (b) BSCF5582; (c) and (d) LSCF6428 and (e) and (f) LSF731.

13 Appendix 6-A

The XRD patterns of the lumen-side and shell-side surfaces of unused LSCF6428 fresh membranes.

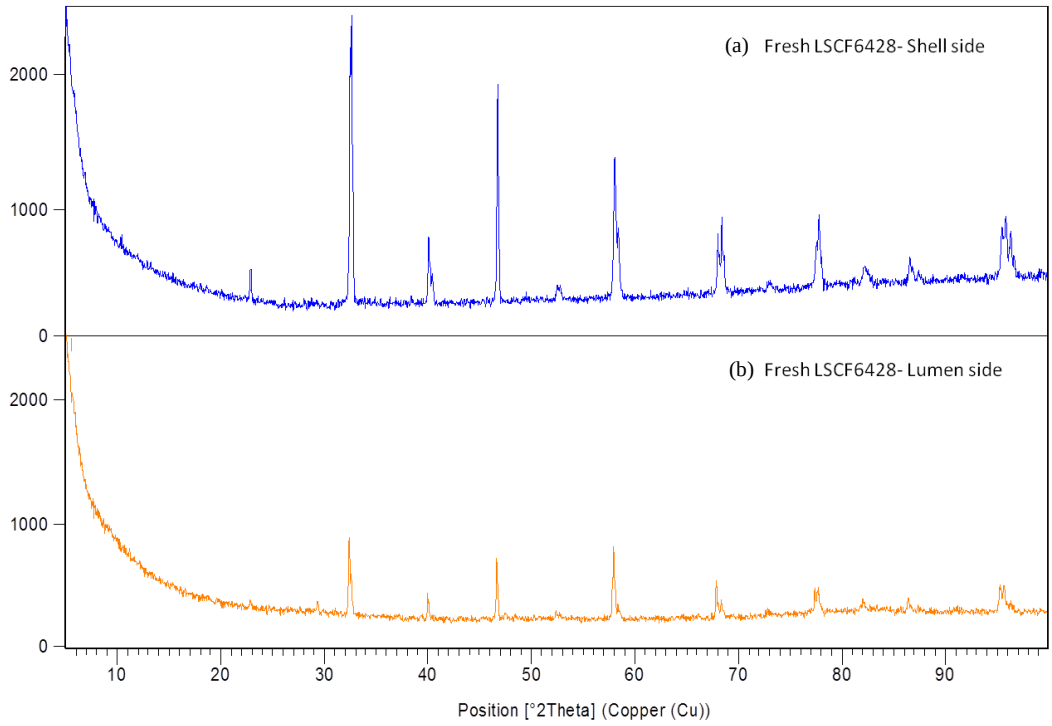

Figure 13.1 XRD patterns of unused LSCF6428 fresh membranes (a) shell side and (b) lumen side.

14 Appendix 6-B

Error analysis

In general, a source of error is any factor that may affect the outcome of the experiment. In this present work, uncertain measurements generated by the equipment used in the experiments can result in these sources of errors. The experimental errors calculated in this section have not been included into the data of this thesis (apart from the material balance calculations), however they are discussed and used to explain possible discrepancies. Each source of error is discussed in the following sections.

Water saturator

The routine set point for the water saturator was 7.2% H_2O (water bath maintained at 40°C) balanced in argon, the water content was monitored by a hygrometer and the reading generally fluctuated between 7.1 and 7.3%. The temperature of the water bath during experiments was monitored carefully, however is conceivable that the temperature was warmer or cooler than intended and this would have affected the water vapour pressure. These fluctuations could also be result of the hygrometer itself performing feedback control or due to variation of the laboratory temperature.

This experimental error of ± 0.1% H_2O (± 10% of the set point) is relatively small and would have little effect on the results obtained during hydrogen production (membrane-based steam reforming experiments), as the hydrogen mole fraction signal of the GC is calibrated using the calibration gas containing hydrogen. Also, over a long experiment (*ca* 400 hours) a variance of ± 0.1 H_2O would make little difference as the shell-side of the membranes would be fully oxidised over this period and would not affect the oxidation step of the experiment.

Mass flow controllers

The usual flow rate delivered to the membrane reactor was 20 ml (STP) min^{-1} (routine set point). To ensure flow rates were accurate, an independent flow meter (Varian UK.) was used to monitor the set flow rate. The readings generally fluctuated and an experimental absolute error of ± 0.5 ml min^{-1} was recorded. This error would not make much difference for mole fraction measurements by the GC, however during the

calculation of the permeation rates (Equation (3.2)) this would lead to an error of ± 2.5%.

Leaks

Preliminary experiments (*Section 4.4*) were performed to detect if a refractory membrane could be adequately sealed under the membrane-based steam reforming reaction conditions at 900°C. It was noticed that at a flow rate of 20 ml (STP) min^{-1} a maximum background leak of oxygen (0.104 mol %) and nitrogen (0.344 mol %) was observed. Therefore, an approximate total error of ± 0.1 mol. % for oxygen permeation could be assumed for measurement by the GC, however the oxygen permeation rate is adjusted to take this into account by subtracting the rate of oxygen leakage based on the rate of nitrogen leakage (assuming a 1:4 oxygen:nitrogen ratio).

Gas chromatograph

Prior to the beginning of the experiments, the GC was calibrated as described in *Section 3.4.4*. However, the GC could not maintain the correct calibration over *ca* 800 hours of experiment as a result of drift in stability of the GC detector. Recalibration of both CGs at the end of this period indicated a drift of no more than 10 %, calculated by Equation (14.1)

$$\%Error = \frac{|ReC_v - C_v|}{C_v} \times 100 \qquad (14.1)$$

Where ReC_v is the recalibration value (measured) after the experiments and C_v is the calibration value at the beginning of the experiment. This uncertainty (percentage error) of measuring the gas phase mole fractions of the products was applied for the material balance calculation (*Section 6.5*) and presented in Table 6.3.